**From the holdings of the Department of Special Collections , Princeton University Library, Princeton, NJ**

These documents are either in the public domain, or can only be used for educational and research purposes (Fair use) as per U.S. Copyright law (text below). By accessing this file, all users agree that their use falls in the public domain or within fair use as defined by the copyrightlaw. We do not charge any permission or usage fees for the publication of images of material inour collections, including those provided by Princeton University Library, via our website, catalog, or directly from staff.For more information regarding copyright, credit, and citation please review the information onthe Copyright, Credit and Citation Guidelines page of our website.
https://library.princeton.edu/special-collections/policies/copyright-credit-and-citation-guidelines. If you have any questions, including how to order higher-quality images from the collection, contact Special Collections Public Services via our Ask Us! Form. https://library.princeton.edu/special-collections/ask-us

Doctoral Dissertations, 2011-2026 | Atmospheric and Oceanic Sciences

2021

# Investigating the physical controls of monsoon seasonality in a hierarchy of climate models

Smyth, Jane Elizabeth

Princeton, NJ : Princeton University

http://arks.princeton.edu/ark:/88435/dsp01jh343w42w

*U.S. Copyright law: The copyright law of the United States (Title 17, §108, United States Code) governs the making of photocopies or other reproductions of copyrighted material. Under certain conditions specified in the law, libraries and archives are authorized to furnish a photocopy or other reproduction. One of these specified conditions is that the photocopy or reproduction is not to be used for any purpose other than private study, scholarship, or research. If a user makes a request for, or later uses, a photocopy or reproduction for purposes in excess of fair use that user may be liable for copyright infringement. This institution reserves the right to refuse to accept a copying order if, in its judgment, fulfillment of the order would involve a violation of copyright law. https://www.copyright.gov/title17/title17.pdf*

# Investigating the physical controls of monsoon seasonality in a hierarchy of climate models

Jane Elizabeth Smyth

A Dissertation
Presented to the Faculty
of Princeton University
in Candidacy for the Degree
of Doctor of Philosophy

Recommended for Acceptance
by the Program in Atmospheric and Oceanic Sciences
Adviser: Dr. Yi Ming

September 2021

© Copyright by Jane Elizabeth Smyth, 2021.

All rights reserved.

# Abstract

Monsoons supply the majority of annual rainfall to land regions across the tropics and play a prominent role in global climate. Despite this, we lack a complete mechanistic understanding of monsoon characteristics and how they might change with warming. This dissertation draws on theory and a range of climate models to elucidate the physics governing monsoon circulations.

First, we investigate the seasonally dependent responses of the South American monsoon to warming. In the latest Geophysical Fluid Dynamics Laboratory Atmospheric Model (AM4), uniform 2-K sea surface temperature warming reduces precipitation by 11%, and precipitation minus evaporation by 40%, in the monsoon onset season, producing a more severe dry season. A column-integrated moist static energy budget analysis helps elucidate the drying mechanism. By comparing the response across seasons we identify two necessary conditions for a region to exhibit a substantial drying response to warming.

To better understand the seasonal and global variations in monsoon circulations, Chapter 3 utilizes an idealized modeling framework. We systematically vary the moisture and albedo parameters over an isolated South American continent with reduced heat capacity, but no topography. Irrespective of the local moisture availability, the seasonal cycles of precipitation and circulation over the monsoon sector are distinctly monsoonal with the default surface albedo, but with differing characteristics and dynamical mechanisms. The analysis supports that when the land-ocean thermal contrast is strong enough, inertial instability is sufficient for producing a shallow but vigorous circulation and converging a large amount of moisture from the ocean. Once the land is sufficiently moist, convective instability takes hold and the shallow circulation deepens. Chapter 4 investigates the monsoonal precipitation over a dry continent on synoptic timescales, and provides additional evidence for the importance of inertial instability.

In Chapter 5, we utilize an Earth System Model (ESM4.1) to investigate changes in precipitation and aridity over the South American monsoon sector in future emissions scenarios. The projected runoff reductions have implications for energy system planning in Brazil, where 60-80% of monthly power generation comes from hydropower. The possibility of seasonal power generation deficits underscores the importance of climate risk management in the energy sector.

# Acknowledgements

First and foremost I thank my advisor Yi Ming, who first welcomed me to the NOAA Geophysical Fluid Dynamics Laboratory as an undergraduate Hollings Scholar. Yi has taught me so much about the climate system and about how to identify important problems and pursue them with rigor. Our meetings consistently inspire and motivate me. Yi's kind mentorship helped me enjoy these years and stay the course when I faced challenges. It has been an honor to collaborate with him. I have also benefited from the thoughtful input of my committee members Isaac Held and Stephan Fueglistaler, and I thank Isaac for providing insightful feedback on my papers. Thanks to the entire AOS faculty for their teaching and for fostering a collegial environment.

I am thankful to Michael Oppenheimer for supervising my HMEI Science, Technology, and Environmental Policy (STEP) Fellowship project (Chapter 5). Michael quickly gets to the heart of an issue, and I learned a lot about the social and economic dimensions of climate change from him and his research group. Thanks are also due to Renato Carlos Zambon at the University of Sao Paulo, who generously shared his expertise on the Brazilian power sector.

In my fourth year I was a teaching assistant for Rob Socolow's course "Time Capsules for Climate Change." Thanks to Rob for showing me that it is possible to create a meaningful, personal course that interweaves science and humanity.

My undergraduate years at Yale set me on the path to pursue graduate school and prepared me well. Trude Storelvmo was a life-changing mentor for three years; thank you so much for the opportunities and encouragement. Mary-Louise Timmermans sparked my interest in Geophysical Fluid Dynamics with her awe-inspiring rotating tank experiments. Bill Boos and Ron Smith also taught influential courses.

I feel lucky to have experienced graduate school with my cohort, Shiv Priyam Raghuraman and Yi Zhang. Working on problem sets and discussing concepts with you and Matthew Gliatto made the early years much less daunting. I could never

have learned as much as I did without you. Priyam also became one of my closest friends and helped me laugh (a lot) over the past five years.

I do not take for granted the warm and collaborative AOS student community. Student tea times fostered much-needed connection, especially during the pandemic and the final dissertation writing stage. Our reading groups over the years (Great Papers, Randall textbook, Isaac's blog) were particularly special learning experiences.

I want to thank two very important Spencers in the Princeton AOS community. Spencer Hill was a fantastic and fastidious mentor during my Hollings internship at GFDL and inspired me so much. Spencer Clark spent hours helping me set up the aospy climate model analysis tool that he developed with Spencer Hill, as well as the idealized moist model I use in Chapters 3 and 4. His kind and patient advice greatly facilitated my research.

It was a privilege to study at Princeton and interact with scientists from GFDL, the High Meadows Environmental Institute, the Department of Geosciences, and the Princeton School of Public and International Affairs. I also appreciate the technical staff at GFDL, who helped me take full advantage of GFDL's computational resources. Thanks also to Anna Valerio, who keeps the AOS program running smoothly.

I was fortunate to join several communities beyond the AOS program during my time at Princeton. The Princeton Energy and Climate Scholars program introduced me to people across a range of disciplines, and I learned a lot about the climate problem from our group discussions. Editing Highwire Earth with Emily Sun, Julio Herrera-Estrada, and Noemi Vergopolan kept me thinking broadly about sustainable development. I am grateful to the Lewis Center for the Arts for hosting the co-curricular dance program, and in particular to my ballet teacher Kathleen Moore-Tovar, who radiates positivity. I also want to acknowledge Katrina Hui, my super smart and hilarious conference buddy.

I am deeply grateful for my friends in the wider Princeton graduate community, who made these years more fun than I thought possible. I will always treasure the memories we made at the Graduate College, Lakeside, Mercer Street, the Jersey Shore, our audio club, and "The Ballroom." I have to thank Molly Chaney in particular for always having my back. Thanks also to Michael Palmer, Zoe Volenec, Joel Abraham, Rachel Anderson, Ben Weiner, Dan Fess, Archit Verma, Sidu Jena, Karina Tachihara, Alyssa Cady, Claudia Roberts, Gabe Moore, and the whole first year squad that stayed together these last five years.

Thanks to my friends from Long Beach and Yale, who always offered compassionate and refreshing perspectives. My Long Beach friends are truly sisters: Emma Christie, Eileen Kelly, Cara McAuliffe, Samantha Scandole, and Aditi Gupta. From Yale, Tess Maggio, Paul Singer, Josh Faber, Catherine Stark, and Rebecca Bakal have been standout sources of support, fun, and inspiration.

Finally, thanks to my mom, my dad, my brothers John and Aidan, and my extended family for their love, prayers, and unending support through the academic and personal challenges of graduate school. Your faith in me is a constant source of strength.

Dedicated to my mom, Jane Anne Walsh

# Collaborators and prior publications

This thesis research came to fruition thanks to the scientific and technical support of my collaborators. Chapters 2, 3, and 4 are work with Yi Ming. Ming Zhao provided the GFDL AM4 model simulations used in Chapter 2, and Spencer Clark provided help running the idealized moist model studied in Chapters 3 and 4. Chapter 5 was developed in collaboration with Michael Oppenheimer, with crucial input from Renato Carlos Zambon. Kirsten Findell, Chris Milly, and Elena Shevliakova also provided valuable scientific advice on this work. Thanks to to Jasmin John and Elena Shevliakova for making the ESM4.1 simulations available for study.

Chapters 2 and 3 were published as Smyth and Ming (2020) and Smyth and Ming (2021) in the Journal of Climate. The Chapter 2 results were presented at the American Geophysical Union Fall Meeting 2017, the World Climate Research Programme 2nd Meeting on Monsoons and Tropical Rain Belts in 2018, and the 22nd Conference on Atmospheric and Oceanic Fluid Dynamics in 2019. Portions of the work in Chapter 3 were presented at the American Geophysical Union Fall Meeting 2019 and 2020. Chapter 5 was presented at the 2021 World Environmental & Water Resources Congress.

# Contents

Abstract . . . . . iii

Acknowledgements . . . . . v

Collaborators and prior publications . . . . . ix

**1 Introduction** **1**

1.1 Theories for monsoon development . . . . . 2

1.1.1 Three primary frameworks . . . . . 3

1.2 The role of the land surface . . . . . 6

1.3 The case of South America . . . . . 9

**2 Characterizing drying in the South American monsoon onset season with the moist static energy budget** **13**

2.1 Abstract . . . . . 13

2.2 Introduction . . . . . 14

2.3 Experimental Design . . . . . 15

2.3.1 Model Experiments . . . . . 15

2.3.2 Moist Static Energy Budget Theory . . . . . 17

2.4 Results . . . . . 19

2.4.1 Control climate . . . . . 19

2.4.2 Climate response to warming . . . . . 21

2.4.3 Mechanisms of drying . . . . . 26

2.5 Discussion . . . . . 33
2.6 Conclusions . . . . . 35

**3 Investigating the impact of land surface characteristics on monsoon dynamics with idealized model simulations and theories 38**

3.1 Abstract . . . . . 38
3.2 Introduction . . . . . 39
3.3 Experimental Design . . . . . 40
3.4 Results . . . . . 43
3.4.1 Varying land moisture conditions . . . . . 43
3.4.2 MSE Budget Analysis . . . . . 53
3.4.3 Land albedo perturbation experiments . . . . . 56
3.5 Discussion . . . . . 64
3.6 Supplemental Material . . . . . 69

**4 Synoptic analysis of monsoonal precipitation mechanisms over an idealized dry continent 73**

4.1 Introduction . . . . . 73
4.2 Results . . . . . 77
4.2.1 Event Analysis: Days 21-23 . . . . . 85
4.2.2 Monsoon low pressure systems . . . . . 91
4.3 Discussion . . . . . 93

**5 The impact of climate change on hydrological seasonality in Brazil: implications for energy system planning 95**

5.1 Introduction . . . . . 95
5.2 Methods . . . . . 99
5.3 Results . . . . . 102
5.3.1 The monsoon-sector climate response . . . . . 102

5.3.2 Runoff changes in key hydropower basins . . . . . 114
5.4 Policy implications . . . . . 118

**6 Conclusion** **124**

6.1 Summary . . . . . 124
6.2 A model hierarchy approach . . . . . 127
6.3 Future research directions . . . . . 130

**Bibliography** **133**

# Chapter 1

# Introduction

The physical factors controlling the tropical precipitation distribution remain poorly characterized, especially on regional scales. This incomplete theoretical understanding impedes efforts to predict the precipitation response to climate change (e.g. Xie et al., 2015; Kent et al., 2015; Chou and Neelin, 2004). The challenge is particularly salient over land, where economies and ecosystems are sensitive to changes in rainfall characteristics (amount, intensity, seasonal cycle, etc.) (e.g. Byrne and O'Gorman, 2015; Hill, 2019).

Monsoon circulations play a key role in Earth's climate, including the atmospheric energy, moisture, and momentum budgets. They are the defining feature of the seasonal cycle over tropical land, producing rain in local summer and dry conditions in winter. Consequently, monsoon variability carries great social and economic significance, with agriculture, energy systems, and ecosystem health all depending on monsoon regularity. Over 70% of the world's population is directly impacted by monsoon variability, which can cause droughts, floods, food insecurity, worsened wildfires, energy shortages, and broad financial impacts (An et al., 2015). Interannual monsoon variability, such as in the timing and magnitude of rains, has a major effect on agricultural yields (Webster et al., 1998), as does the rhythm of intraseasonal

variability as the monsoon swings between active and break periods (Gadgil, 2018). Improved physical understanding of monsoon dynamics can enable improved forecasts and adaptation measures, such as altered farming practices for the billions of people inhabiting monsoon regions globally (Gadgil et al., 2002). The theoretical and societal importance of monsoons has motivated sustained research efforts to identify the key mechanisms underlying their development and regulation.

## 1.1 Theories for monsoon development

The traditional conception of monsoons as land-sea breezes (Halley, 1687) has given way to the modern perspective of monsoons as an integral component of the global atmospheric circulation and climate. Studies applying the axisymmetric theory for the Hadley cells to idealized monsoons have driven this shift in thinking (Privé and Plumb, 2007a,b; Bordoni and Schneider, 2008). When a zonally symmetric atmosphere is subject to subtropical forcing, the transition from a thermodynamic equilibrium to an angular momentum conserving overturning circulation occurs when the forcing is strong enough to induce an upper-tropospheric anticyclonic relative vorticity that offsets the planetary vorticity (i.e. when absolute vorticity $\eta = \zeta + f$ approaches zero) (Plumb and Hou, 1992). Based on this theory for angular momentum conserving circulations and related work (e.g. Emanuel, 1995), Privé and Plumb (2007a,b) link the meridional extent of the monsoonal overturning cell to the near-surface maximum of subcloud moist static energy (MSE), and find that this is a good indicator of the monsoon extent even when zonal symmetry is broken. They base this conclusion on a series of experiments using the MITgcm with Newtonian cooling and prescribed SSTs. Bordoni and Schneider (2008) describe a rapid summertime transition to off-equatorial tropical convergence in an idealized moist aquaplanet model with a two-stream gray radiation scheme. This indicates that land-sea thermal contrast is not fundamental to

monsoon emergence. They characterize monsoons as regime transitions of the Hadley circulation: during the monsoon season, the cross-equatorial winter Hadley cell is in an angular momentum-conserving regime, subject to little influence by extratropical eddies. The alignment of streamlines with angular momentum contours over the Indian monsoon sector suggests the potential utility of this theory for off-equatorial monsoons (Bordoni and Schneider, 2008).

Work since the 1990s has shown that the seasonal transitions of monsoon circulations depend not on land-sea thermal contrast, but on local meridional moist static energy (MSE) gradients, where higher near-surface MSE favors convection and rainfall (Emanuel, 1995; Privé and Plumb, 2007a; Seth et al., 2018). In six global monsoon systems, interannual precipitation variability is strongly correlated with low-level MSE anomalies poleward of the climatological maximum (Hurley and Boos, 2013). Advances in relating the location of the Intertropical Convergence Zone (ITCZ) to interhemispheric energy imbalances have also shed light on monsoonal behavior (Kang et al., 2008; Schneider et al., 2014; Heaviside and Czaja, 2013). However, the distinct behavior of land monsoons and adjacent oceanic ITCZ over the seasonal cycle, inter-annually, and in response to orbital forcing underscores the importance of zonal asymmetry in the tropics (Adam et al., 2016; Boos and Korty, 2016; Smyth et al., 2018). Numerous authors therefore advocate for an adaptation of the zonal mean energetic framework to account for zonal inhomogeneities (Muller and O'Gorman, 2011; Boos and Korty, 2016; Biasutti et al., 2018). A more complete review of our theoretical understanding of monsoon circulations is provided in the following section.

### 1.1.1 Three primary frameworks

There are three primary theoretical conceptions of monsoons in the literature: one based on convective quasi-equilibrium (CQE), another founded on the MSE budget,

and one that frames the monsoon as an extension of the zonal-mean ITCZ (Hill, 2019).

In the CQE view, the monsoonal overturning cell extends to the latitude of highest near-surface MSE, with the maximum rainfall located just equatorward thereof (e.g. Privé and Plumb, 2007a,b; Nie et al., 2010; Hurley and Boos, 2013). CQE posits that convection couples near-surface and upper tropospheric MSE, linking high boundary layer MSE to high upper-tropospheric potential temperatures (Emanuel and Bretherton, 1994). Within this framework, the impact of a perturbation on the monsoon location can be understood via its effect on the near-surface thermodynamics. While this theory does not explain what controls monsoon strength, Harrop et al. (2019) show that the curvature of sub-cloud moist entropy could be a strong predictor of the precipitation minus evaporation magnitude. The CQE paradigm does not seem to hold as cleanly in South America as in other monsoon regions; there is a broad summer maximum of near-surface moist entropy over the continent, with the maximum upper-tropospheric saturation moist entropy located near its poleward boundary (Nie et al., 2010). While useful, the CQE paradigm provides little prognostic power in the absence of a complete theory for what controls the near-surface MSE distribution itself.

Alternatively, some studies use the column-integrated MSE budget as a basis for characterizing tropical rainfall, including monsoon circulations (e.g. Neelin and Held, 1987; Chou and Neelin, 2004; Back and Bretherton, 2006; Neelin, 2007; Hill et al., 2017). The MSE budget, presented in detail in Section 2.3.2, states that the net column forcing from radiative and turbulent heat fluxes must balance the atmospheric MSE flux divergence and the time tendency of column-integrated internal energy. While MSE budget analysis is a diagnostic approach, it has been applied in various fruitful ways, such as: to evaluate the limits on the poleward extent of monsoons (e.g. Chou and Neelin, 2001); to identify key mechanisms of tropical precipitation change,

such as the "upped-ante" and "rich-get-richer" responses (Chou and Neelin, 2004); and to assess a circulation's susceptibility to these responses under climate change (Hill et al., 2017; Smyth and Ming, 2020).

Unlike the local control of precipitation in the CQE and MSE budget theories, the ITCZ framework takes a unified view of land and ocean precipitation as guided by zonal mean energetics (Chao and Chen, 2001; Gadgil, 2018). The ITCZ is the tropical rainfall maximum whose location is determined by the cross-equatorial extent of the Hadley circulation, which in turn is guided by the energy flux equator, the zero-crossing of the meridional atmospheric heat transport (Kang et al., 2008). The ITCZ shifts towards the hemisphere with higher net energy input to the atmosphere, allowing anomalous energy transport to the opposite hemisphere by the upper branch of the cross-equatorial Hadley cell (e.g. Bischoff and Schneider, 2014). On paleoclimate timescales, the Indian monsoon complies with ITCZ constraints, migrating towards asymmetric hemispheric warming (Schneider et al., 2014), and on an interannual basis, a strong Indian monsoon is associated with northward migrations of the meridional overturning circulation (Walker et al., 2015). The ITCZ perspective is consistent with a global monsoon mode that encompasses the solstitial migrations of the convergence zone across the regional subsystems (Geen et al., 2020). As in CQE theory, the view of monsoons as a regional extension of the thermally-direct Hadley circulation highlights the role of near-surface MSE gradients, rather than temperature gradients, in modulating the monsoon position (Walker et al., 2015).

As mentioned earlier, the ITCZ over land and ocean may shift in opposite directions in certain situations, hinting at potential limitations of the ITCZ framework (Smyth et al., 2018; Hill, 2019). In general, the relevance of zonally symmetric theory for realistic, zonally confined monsoon circulations is unclear. In a zonally asymmetric context, a meridional overturning circulation can develop before the upper-tropospheric absolute vorticity approaches zero because of the contribution of the

zonal eddy momentum flux divergence to the zonal momentum balance (Walker and Schneider, 2005, 2006). In addition, zonally asymmetric forcing induces zonal overturning circulations, as in the linear response to tropical heating (Zhai and Boos, 2015; Gill, 1980). In a dry model with forcing as in Held and Suarez (1994) but with zonal structure to the equilibrium temperature profile, the total monsoon-sector upward mass flux associated with both zonal and meridional divergent circulations increases linearly with forcing strength (Zhai and Boos, 2015). This demonstrates clear deviation from the zonally symmetric theory that predicts threshold behavior (Zhai and Boos, 2015).

While these three theoretical pictures of monsoon circulations dominate the literature, another influential theory for tropical rainfall is that put forth by Lindzen and Nigam (1987), which emphasizes the boundary layer convergence driven by pressure gradients associated with SST gradients. This mechanism is doubtless important for understanding the climatological precipitation distribution, and for inducing the bottom-heavy convection profiles found in regions with strong SST gradients, like the East Pacific ITCZ (Back and Bretherton, 2006, 2009). The relative importance of theories based on energy balance versus the boundary layer momentum budget is a subject of active research (Held, 2019).

## 1.2 The role of the land surface

Globally, precipitation balances evaporation and we expect increases in both with global warming; this follows from the energetic constraint that globally, latent heating balances radiative cooling, which increases with greenhouse gas warming (Allen and Ingram, 2002). This global constraint sheds little light on regional hydroclimate changes, particularly over land where moisture limitations complicate the surface partitioning of latent and sensible heat fluxes. Further, land is subject to complex

feedbacks between surface properties and rainfall. Here, we review our present understanding of how land surface properties shape the tropical precipitation distribution.

It is not straightforward to assess the role of land surface properties within any of the monsoon theories summarized in the previous section. Vegetation impacts both albedo and moisture fluxes, driving feedbacks between rainfall changes and ecological transitions (Charney, 1975). For example, decreases in rainfall can reduce vegetation cover, increasing albedo and reducing the net column radiation flux, thus further reducing rainfall and contributing to desertification (Charney, 1975). Indeed, the albedo bias associated with vegetated land regions was found to be an important contributor to inter-model rainfall discrepancies, especially over the Asian monsoon sector (Levine and Boos, 2017). It is important to disentangle the feedbacks impacting precipitation variability over land, where such variability matters most for the drinking water supply, agriculture, ecosystems, infrastructure, industry, and more.

Soil moisture has implications for the partitioning of surface turbulent fluxes, and therefore the surface temperature, precipitation, and regional circulation (e.g. Seneviratne et al., 2010). In regions with strong land-atmosphere coupling, including India, West Africa, and parts of tropical South America (Koster et al., 2004), soil moisture strongly impacts the evaporative fraction and daily maximum surface temperature (Schwingshackl et al., 2018). Numerous studies have shown that including interactive soil moisture introduces memory or "hydrological persistence" to the monsoon system and increases low-frequency precipitation variability (Delworth and Manabe, 1988; Koster and Suarez, 1995; Ferranti et al., 1999; Dirmeyer et al., 2009). Webster (1983) shows the importance of ground hydrology for capturing the monsoon active-break sequence. More recent work on the Indian monsoon illustrates how powerful these internal dynamics can be: an experiment in which spring (May) forcing is imposed develops mid-summer-like monsoonal conditions in equilibrium due to the coupling of soil moisture with the circulation (Bollasina and Ming, 2013).

Several studies have endeavored to elucidate how continental moisture conditions exert such pronounced impacts on tropical precipitation. When a dry equatorial continent is subjected to perpetual solstice forcing with fixed SSTs, the ITCZ breaks and drought conditions develop despite substantial lower tropospheric convergence (Cook and Gnanadesikan, 1991). Shukla and Mintz (1982) similarly report enhanced thermally driven convergence but reduced precipitation over continents with disabled evapotranspiration. Cook and Gnanadesikan (1991) attribute the simulated precipitation pattern to the low boundary layer relative humidity combined with large-scale subsidence over the western continent, and note that these equilibrium results are more relevant to interannual rather than seasonal variability. Along similar lines, Chou et al. (2001) show that interactive soil moisture reduces the precipitation relative to a saturated land surface. They argue that this is due to the reduction in convective available potential energy (CAPE) when moisture is limited, and to the impact of enhanced subtropical heating on the circulation pattern. Interestingly, severing the two-way coupling of soil moisture and precipitation by externally prescribing soil moisture has different impacts on monsoonal precipitation throughout the seasonal cycle; this underscores that surface moisture plays a complex and time-varying role in monsoon dynamics (Berg et al., 2017). Zhou and Xie (2018) utilize an idealized model with gray radiation to evaluate the role of geometry, albedo, soil moisture, and ocean heat fluxes on monsoon properties. They find that with the exception of soil moisture, all these factors can be understood via their effects on the surface equivalent potential temperature ($\theta_e$, essentially MSE) distribution, underscoring the importance of CQE dynamics. In their experiments, soil moisture changes elicit more complex circulation responses that are not always consistent with the migration of the maximum near-surface MSE, and warrant further study. We do not yet have a complete understanding of how seasonally varying soil moisture shapes monsoon dynamics or the sensitivity of the circulation to forcing.

## 1.3 The case of South America

Chapters 2 and 5 of this dissertation focus explicitly on the South American monsoon, and Chapters 3 and 4 utilize South American continental geometry, albeit in a highly simplified model and with an emphasis on fundamental monsoon dynamics. The focus on South America is motivated by several factors. The South American monsoon has received comparably little research attention, with more focus on the South Asian monsoon and, particularly following episodes of severe Sahelian drought in the 20th and 21st centuries, the West African monsoon (Held et al., 2005). From a theoretical perspective, the choice of South America allows us to consider the dynamics governing a near-equatorial monsoon, in contrast to the off-equatorial Indian monsoon where Earth's rotation has a stronger influence on the circulation. From a societal perspective, climate change-induced rainfall reductions in South America could destabilize the Amazon rainforest ecosystem, agriculture, and the hydropower-based Brazilian electricity system, among other impacts (Boisier et al., 2015; Ruffato-Ferreira et al., 2017).

The South American monsoon system sustains a large section of the world's largest rainforest: the Amazon. The dry season length plays a limiting role in rainforest survival, such that rainfall reductions in this season are more ecologically consequential than comparable changes during the wet season (Fu and Li, 2004). Given its relatively long dry season, the South American monsoon sector is vulnerable to reductions in soil moisture and susceptible to a rainforest-savanna ecosystem transition (Boisier et al., 2015; Fu et al., 2013). The Amazon rainforest plays an outsized role in the global carbon cycle, accounting for a quarter of the global forest carbon uptake of 2.4 billion metric tons per year (Kintisch, 2015). Therefore, beyond the loss of biodiversity, such an ecosystem transition would increase atmospheric $CO_2$ globally (Fu et al., 2013).

As with land regions in general, the South American climatological precipitation distribution is impacted by land surface properties. In the NCEP GCM, the inclusion of explicit vegetation biophysical processes improves the South American monsoon representation (Xue et al., 2006). This is primarily due to the impact of resulting thermodynamic gradient changes on the circulation, while the impact of vegetation on the surface water budget contributes to a lesser extent (Xue et al., 2006). Using a regional model during the monsoon onset season (October), Collini et al. (2008) find that South American precipitation in this season has a strong sensitivity to soil moisture reductions. In terms of topography, the presence of the Andes mountains is important for blocking low-MSE westerly inflow, allowing for a southward expansion of the South American monsoon (Chou and Neelin, 2001).

There is not a clear understanding of how precipitation over South America will change with global warming. Coupled Model Intercomparison Project Phase 3 (CMIP3) A1B scenario simulations, which reflect a path to rapid economic growth with a balanced use of energy sources, show disagreement among models with no statistically significant ensemble mean change over South America, while studies of the CMIP5 suite indicate the possibility of severe drying in the annual mean and rainy season (Vera et al., 2006; Li et al., 2006; Torres and Marengo, 2013; Lee and Wang, 2014). On the other hand, nine of ten CMIP5 model historical runs indicate a trend of increased rainy season duration over the monsoon sector (Jones and Carvalho, 2013). These disparate conclusions can be attributed to differing parameterizations of key convective, cloud, and land processes in models, and uncertainty regarding model-simulated sea surface temperature (SST) changes (Li et al., 2006).

Despite the aforementioned issues, some aspects of how the seasonal cycle of precipitation will respond to increased atmospheric $CO_2$ are well characterized. Based on CMIP3, CMIP5, and CMIP6 simulations, higher $CO_2$ leads to an increased amplitude in the seasonal cycle of precipitation (Chou and Lan, 2012; Dwyer et al., 2014;

Wang et al., 2020), a phase shift such that rainfall is inhibited in spring and enhanced later in the rainy season (Biasutti and Sobel, 2009; Seth et al., 2011, 2013), and a longer dry season over land (Lau et al., 2013; Boisier et al., 2015), at least in the Southern Hemisphere monsoon sectors (Wang et al., 2020). Further supporting the latter conclusion, and counter to the results of Jones and Carvalho (2013), Fu et al. (2013) report an observed trend of lengthening dry seasons over southern Amazonia between 1979 and 2011. They link the extended dry season with increased convective inhibition: surface relative humidity has declined over the Amazon due to increasing surface temperatures and insufficient surface moisture sources. Such observations portend further drying as the climate warms. Pietschnig et al. (2019) argue that the two key ingredients for future drying over South America are limited soil moisture and the presence of Africa, which induces a Matsuno-Gill-type circulation response with warming that results in anomalous subsidence over South America. This work does not address the fact that the projected South American precipitation changes differ over the seasonal cycle.

Since rainforests are much less prevalent in regions where the dry season length exceeds three months (with dry month precipitation less than 2 mm day$^{-1}$), the rainforest area is expected to diminish with surface warming (Boisier et al., 2015). Further, land use changes impacting the rainforest itself can drive large changes in the overlying atmospheric circulation. During the rainy season, condensational heating from precipitation enhances moist Atlantic inflow, which further enhances precipitation. By reducing local moisture availability and surface wind strength through surface evapotranspiration and roughness effects, deforestation can impede this positive feedback and severely limit the magnitude of the South American monsoon (Boers et al., 2017).

The mechanisms of future drying over South America will be explored, and an explanation for its seasonally varying response put forth, in Chapter 2 of this disserta-

tion. Chapter 3 employs a moist idealized modeling framework to discern the impact of land surface albedo and moisture conditions on monsoon properties. Chapter 4 examines the synoptic dynamics underlying monsoonal precipitation in an idealized model experiment in which the land surface is completely dry. Chapter 5 considers future changes in precipitation and aridity indices over the South American monsoon sector in the latest GFDL Earth System Model, and analyzes how the projected runoff reductions might impact hydropower production and energy system planning in Brazil. Chapter 6 summarizes the main messages of the dissertation and identifies future research directions.

# Chapter 2

# Characterizing drying in the South American monsoon onset season with the moist static energy budget

## 2.1 Abstract

The tropical atmospheric circulation and attendant rainfall exhibit seasonally dependent responses to increasing temperatures. Understanding changes in the South American monsoon system is of particular interest given the sensitivity of the southern Amazon rainforest to changes in dry season length. We utilize the latest Geophysical Fluid Dynamics Laboratory Atmospheric Model (GFDL AM4) to analyze the response of the South American monsoon to uniform sea surface temperature (SST) warming. SST warming is a poorly understood yet impactful component of greenhouse gas induced climate change. Region-mean rainfall declines by 11%, and net precipitation (precipitation minus evaporation) by 40%, during the monsoon onset

season (September-November), producing a more severe dry season. The column-integrated moist static energy (MSE) budget helps elucidate the physical mechanisms of the simulated drying. Based on the seasonal analysis, precipitation reductions tend to occur when (1) a convecting region's climatological MSE export is dominated by horizontal rather than vertical advection, and (2) the horizontal MSE advection increases in the perturbed climate, impeding ascent. On a synoptic scale, the South American low-level jet strengthens and exports more moisture from the monsoon sector, exacerbating spring drying.

## 2.2 Introduction

The literature outlined in the Introduction (Section 1.3) demonstrates a growing consensus that southern Amazonia may be subject to substantial changes in hydroclimate as temperatures increase. However, given the focus on observational data and output from fully-coupled models forced with complicated emissions scenarios, it has been difficult to establish definitive physical explanations for these results. Simplified model experiments enable one to better identify and understand the mechanisms of precipitation change. Insights from these studies can elucidate results from more realistic modelling experiments and the observational record, and build (or erode) confidence in the coupled model projections. This study was conceived to work towards that end.

To approach this aim, the study draws on the MSE budget theoretical framework, background on which will be provided in the following section. The analysis focuses on how the the climatological MSE budget regulation relates to the hydrological response to SST warming, with a chief interest in how this relationship varies seasonally over the monsoon sector. While the MSE theory is diagnostic in nature, establishing how the budget regulation relates to forced hydrological changes might inform a prog-

nostic theory. In addition, the study examines how synoptic circulation changes may contribute to the South American hydrological response to warming. The overarching goal of the study is to gain mechanistic insights that will aid interpretation of CMIP model experiments and observations, ultimately informing climate projections.

## 2.3 Experimental Design

### 2.3.1 Model Experiments

We utilize two simulations performed with the latest Geophysical Fluid Dynamics Laboratory (GFDL) atmospheric general circulation model AM4. AM4's cubed-sphere dynamical core avoids polar singularities and reduces the size variation of grid boxes, among other benefits. Compared to previous generations of GFDL models, it features improved resolution ($\sim$ 100 km, 33 vertical levels), a double plume model representing shallow and deep convection, and updated radiative transfer code. For more details on the model formulation, the reader is referred to Zhao et al. (2018a,b).

The control simulation is forced with a monthly varying climatology of observed gridded SSTs and sea-ice concentrations (1979-2014) from Taylor et al. (2000), global monthly mean concentrations of greenhouse gases (GHGs), ozone depleting substances, and emissions from the year 2010, and a fixed seasonal cycle of vegetation (Zhao et al., 2018b).

In the experimental simulation, the prescribed SST field is uniformly warmed by 2 K at all times (Cess et al., 1990). SSTs exert a strong if not dominant influence on precipitation variability in monsoon regions (Hurley and Boos, 2013). For example, previous studies succeeded in simulating the late 20th century Sahel drought given the time series of observed SSTs (Giannini et al., 2003; Lu and Delworth, 2005). Determining how the SST changes associated with global warming modulate precipitation is therefore a practical first step towards understanding the full response. This

problem can be made more tractable by decomposing the anomalous SST field into uniform and spatially varying components (Chadwick, 2016; Hill et al., 2015, 2017). Uniform SST warming experiments therefore allow one to better understand the full climate response in coupled models (e.g. Held et al., 2005). A uniform 2-K perturbation experiment is an appealing idealization for multiple reasons. First, mean SST warming is a robust response to rising greenhouse gas levels. Second, over tropical land areas, the precipitation response to SST changes and its inter-model uncertainty are both dominated by the response to the uniform warming component (Chadwick, 2016; He et al., 2014; Held et al., 2005; Hill et al., 2017). Previous studies utilizing uniform SST warming simulations to assess changes in the seasonality of tropical precipitation consider the zonal-mean exclusively (Huang et al., 2013; Dwyer et al., 2014). The present work builds on these studies by focusing on regional precipitation changes and utilizing the MSE budget framework to interpret results.

Uniform SST warming experiments exclude, by design, the influence of changing SST patterns, vegetation, and $CO_2$ radiative effects. This simplification facilitates mechanistic analysis because hydrological changes can be attributed to a spatially and temporally uniform change in the lower boundary condition. If a precipitation response is common to the uniform SST warming experiment and more realistic high-$CO_2$ experiments (e.g. Biasutti et al. (2009); Seth et al. (2011, 2013); Wang et al. (2020)), it is likely a robust response to warming. Where the realistic high-$CO_2$ experiment differs, some other aspect of the climate response to greenhouse gas emissions opposes that elicited by uniform warming. Further experiments would be needed to diagnose the underlying driver (e.g. anomalous SST gradients, direct $CO_2$ effects, ocean dynamics), and the credibility of the projection depends on our confidence in that aspect of the simulation.

Each simulation was run for 21 years generating daily output, with the first year considered as spin-up initialization and removed for the analyses. Given the sensi-

tivities of the Amazon rainforest to changes in the dry season amplitude and length described in Section 1.3, we focus on the austral spring season (September-November or SON), when the dry season terminates and the monsoon system develops.

### 2.3.2 Moist Static Energy Budget Theory

The MSE budget serves as the principal theoretical framework in our analysis of monsoon rainfall. The MSE or $h$ is defined as $h = c_p T + gz + L_v q - L_f q_{ice}$, where $c_p$ is the heat capacity of air at constant pressure, $T$ is temperature, $g$ is the gravitational constant, $z$ is geopotential height, $L_v$ is the latent heat of vaporization of water, $q$ is specific humidity, $L_f$ is the latent heat of fusion of water, and $q_{ice}$ is specific mass of ice. The column-integrated MSE budget is given by:

$$\frac{\partial}{\partial t}\{\overline{\mathcal{E}}\} + \{\overline{\mathbf{v}} \cdot \nabla_p \overline{h}\} + \left\{\overline{\omega}\frac{\partial \overline{h}}{\partial p}\right\} + \nabla \cdot \{\overline{h'\mathbf{v}'}\} \approx \overline{F}_{net}. \tag{2.1}$$

Brackets represent column integrals, $\mathcal{E}$ is the internal energy, $\mathbf{v}$ is the horizontal wind vector, $\nabla_p$ is the horizontal gradient operator on constant pressure surfaces, $\omega$ is vertical velocity in pressure coordinates, and $\overline{F}_{net}$ is the total of surface and top-of-atmosphere (TOA) radiative fluxes and surface turbulent fluxes, signed positive into the atmosphere. Overbars denote time means, and primes are temporal deviations. The advantage of an MSE perspective over a moisture budget approach is that through cancellation of large terms in the vertically integrated thermodynamic and moisture equations, column MSE variations are directly linked to surface and TOA energy fluxes (Neelin, 2007). Further, over land on climatic timescales, the net surface fluxes are zero, so only TOA fluxes need to be considered.

Neelin and Held (1987) first popularized an MSE budget perspective for the purposes of understanding tropical precipitation. They developed a simple two-layer model assuming no transients and small horizontal MSE gradients, and therefore a

dominant balance of $\overline{F}_{net} \approx \left\{\overline{\omega}\frac{\partial \overline{h}}{\partial p}\right\}$. They defined the gross moist stability (GMS) as the MSE difference between the upper and lower layers, essentially the energetic stratification of the atmosphere. Based on this model, one expects precipitation where the GMS is small and positive, signaling MSE export by deep moist convection.

In reality, there exist precipitating tropical regions with negative GMS (essentially $\left\{\overline{\omega}\frac{\partial \overline{h}}{\partial p}\right\} < 0$), such as the Eastern Pacific ITCZ sector (Back and Bretherton, 2006). Given the mid-tropospheric minimum of the typical vertical MSE profile, shallow precipitating convection imports MSE to the column. In such regions, horizontal MSE advection is the primary process balancing energy input $F_{net}$. With its simplifying assumptions, the Neelin-Held theory cannot predict precipitating circulations in a negative GMS regime such as this. Furthermore, the Coriolis parameter is small in the tropics, and pressure gradients are rapidly smoothed by gravity waves. This ensures weak temperature gradients in the free troposphere (Charney, 1963). Thus, horizontal MSE gradients are often thought to largely track moisture gradients associated with boundary layer temperature gradients in the deep tropics, and directly link to precipitation. This, however, cannot rule out the relevance of dry advection in the boundary layer, where the momentum budget has to be taken into account (Lindzen and Nigam, 1987). Particularly when surface temperature gradients are strong, boundary layer convergence governed by momentum dynamics can produce shallow precipitating convection like that observed in the Eastern Pacific ITCZ (Back and Bretherton, 2006).

Hill et al. (2017) further advanced the MSE budget framework with an in-depth study of the MSE budget regulation over land, specifically over the Sahel during the West African monsoon's rainy season. They assess the impact of the convective parameterization and emergent convective depth on the climatological MSE budget regulation to explain the disparate projections of Sahel rainfall among climate models (e.g., Held et al., 2005). The present study takes a similar approach, but with

an emphasis on the seasonal variations of the MSE budget regulation and thus the hydrological response to warming.

## 2.4 Results

### 2.4.1 Control climate

To determine whether the AM4 model is an appropriate tool for the questions of interest, we compare its control simulation of South American precipitation with the 1996-2015 observational record from the Global Precipitation Climatology Project (GPCP v2.3) (Adler et al., 2016). Fig. 2.1a displays the precipitation seasonal cycle, averaged over the South American monsoon region ($5-18°$S, $40-72°$W) and repeated to show all seasonal transitions. Across this domain, DJF precipitation represents at least 30% of the annual mean, and in the core of the monsoon it exceeds 50%, as depicted in Figure 5 of Silva and Kousky (2012) and Figure 2 of Vuille et al. (2012). AM4 simulates the phase of precipitation with good fidelity to GPCP observations. The model-simulated dry winter season from June to August (JJA) exhibits rainfall rates below 1 mm day$^{-1}$. More vigorous precipitation develops in spring (September to November or SON), producing a seasonal mean rainfall rate of 4.1 mm day$^{-1}$. Precipitation continues to intensify throughout austral summer (December-February or DJF), when the simulated monthly mean rainfall exceeds 11 mm day$^{-1}$. In fall (March through May or MAM), the precipitation rate declines steadily toward 1 mm day$^{-1}$. The main shortcomings of the AM4 simulation are the wet bias in summer (maximum $\sim$2 mm day$^{-1}$) and a more modest dry bias in winter, meaning a more rapid transition in spring than observed. By contrast, the CMIP3 model ensemble underestimates precipitation in all seasons (Torres and Marengo, 2013). With such a severe and persistent dry bias, these models are prone to underestimate possible drying in warming experiments.

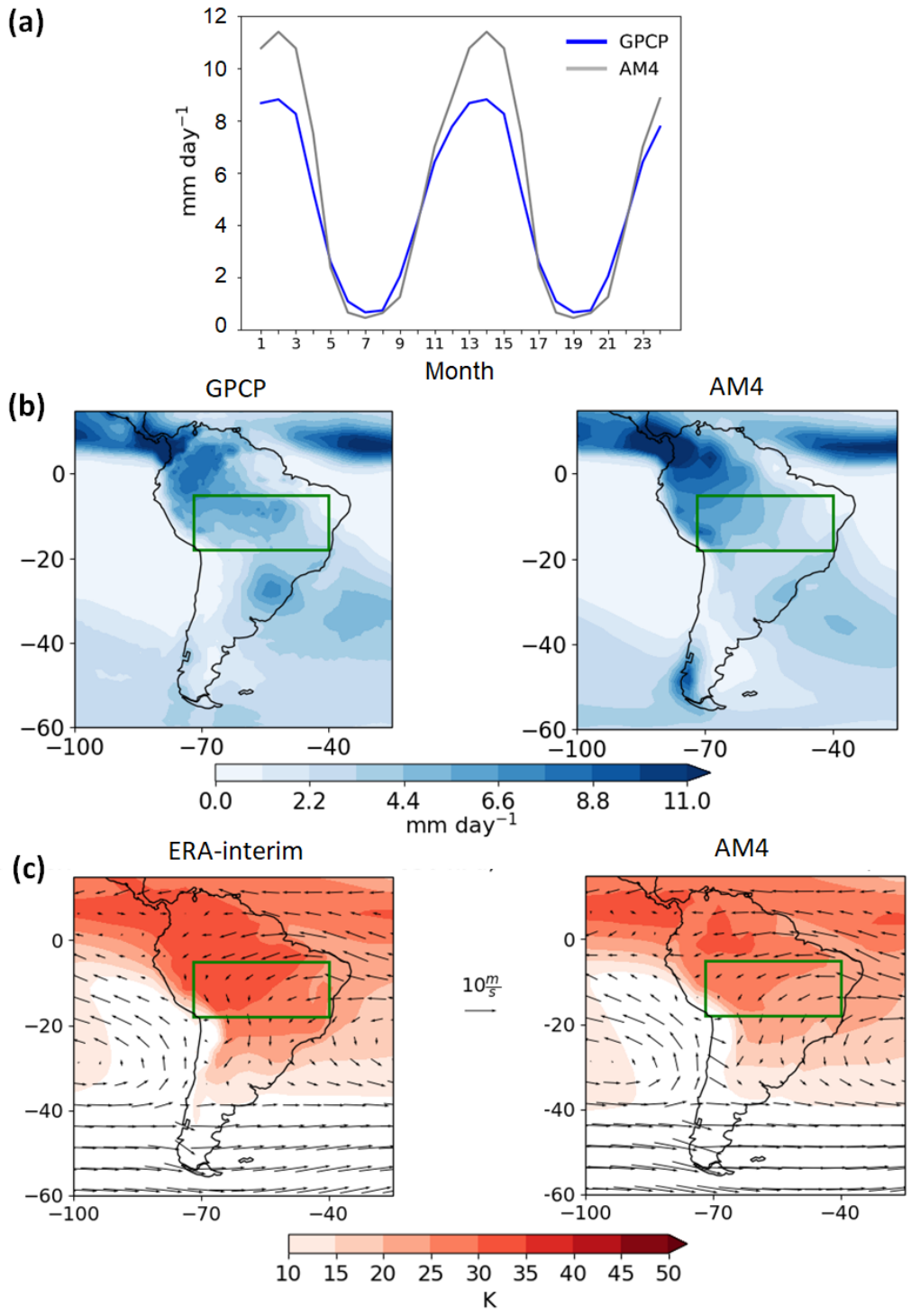



Figure 2.1: (a) Seasonal cycle of region-mean precipitation over the South American monsoon sector (the area outlined in green in (b) and (c)) in GPCP v2.3 observations and AM4. Month 1 and Month 13 represent the monthly mean value for January. The GPCP data is re-gridded to the AM4 horizontal resolution before spatial averaging. (b) Spring (SON) precipitation distribution in GPCP and AM4. (c) SON 850 hPa wind and moisture distributions in ERA-interim and AM4. Moisture is expressed in terms of its contribution to MSE in K.

Besides its realistic seasonality, AM4 captures the spatial distribution of spring rainfall (the main focus of this work) reasonably well, with peak rainfall in the northwest and a distinct South Atlantic convergence zone (Fig. 2.1b). AM4 also realistically simulates the atmospheric flow over the region of interest (Fig. 2.1c). Trade winds flow into the continent from the tropical Atlantic, supplying moisture. They further moisten over the rainforest due to strong evapotranspiration before being deflected by the Andes mountains into a meridional flow (Soares and Marengo, 2009). It is also interesting to note that the boundary layer specific humidity is higher over the Amazon basin than over the Atlantic Ocean to the east (Fig. 2.1c), hinting at the important role of land surface processes in determining the land-ocean distribution of boundary layer moisture. At tropical latitudes, the simulated 850 hPa zonal moisture gradient is weaker than the ERA-interim re-analysis, with insufficient moisture over the Amazon basin (Fig. 2.1c). AM4 may therefore underestimate horizontal moisture advection across the monsoon sector, though the slightly stronger winds in AM4 compared to ERA-interim somewhat compensate.

### 2.4.2 Climate response to warming

The seasonal cycles of precipitation and surface temperature in the 2-K warming experiment are contrasted with those in the control in Fig. 2.2a, with the percentage change in precipitation shown in Fig. 2.2b. The precipitation response is highly seasonally dependent. In the dry winter season, precipitation decreases by 0.10 mm day$^{-1}$ from the climatological value of 0.57 mm day$^{-1}$, which amounts to a 17% decline. The drying is particularly severe in July and August ($\sim$30%). In spring, SST warming gives rise to a drying of 0.44 mm day$^{-1}$ or 11%, and lowers the occurrence of precipitation at all intensities (not shown). Precipitation remains within 1% of control values in summer and fall. In contrast, the surface temperature response is

largely consistent across all seasons. The average warming (∼2.7 K) is greater than the prescribed SST warming (2 K).

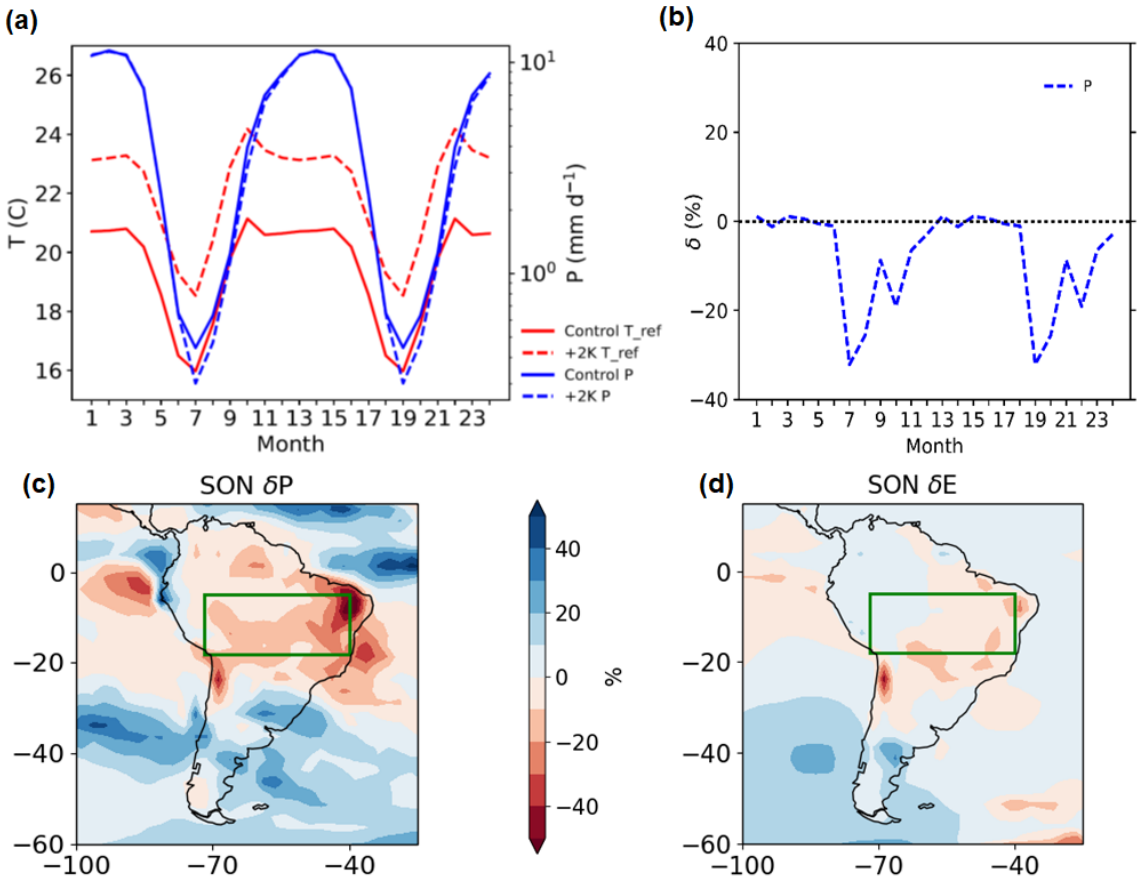



Figure 2.2: (a) Seasonal cycles of precipitation and surface temperature over the South American monsoon sector based on the final 20 years of AM4 control and 2-K simulations. (b) Precipitation anomalies (2-K minus control) expressed as percentage of control values. (c) Spatial distribution of the spring precipitation anomalies (percentage). (d) Same as (c) but for evaporation.

The spring (SON) drying is coherent across the entire South American monsoon domain, and almost the entire continent north of ∼30°S (Fig. 2.2c). The precipitation decreases by over 10% across the center of the monsoon domain and by over 20% along its eastern margin where rainfall is climatologically lower. Also of note is that the semi-arid region of Northeast Brazil exhibits pronounced drying, in some places exceeding 40%. CMIP5 models and observations also predict that this region will grow

more arid and drought-prone with global warming (e.g. Marengo and Bernasconi, 2015). The strong drying signal extends east over the ocean between 10 and 20°S. By contrast, precipitation increases over most of the continent south of 30°S. We further examine this moistening signal in Section 2.4.3.

The vertical structures of some key properties in SON are plotted in Fig. 2.3. The free troposphere warms by more than 2 K in the 2-K experiment, and the warming generally increases with height (e.g. $\sim$ 4 K in the upper troposphere) as a direct consequence of the moist adiabatic control of the tropical lapse rate. Specific humidity also rises, most notably in the lower troposphere, where the relative increase is around 14%. This explains why relative humidity decreases slightly (from $\sim$ 64% to $\sim$ 61%); the rate at which specific humidity increases with temperature is less than 7% $K^{-1}$, the Clausius-Clapeyron scaling. Despite the small drop in relative humidity, the increase in MSE is rather uniform throughout the free troposphere, albeit accompanied by a modest steepening of the vertical gradient, suggesting that the region is still in convective quasi-equilibrium (Emanuel and Bretherton, 1994). Consistent with the substantial reduction in precipitation, the large-scale ascent ($\omega$) declines by up to $\sim$30% (6 hPa $day^{-1}$) in the mid-troposphere. It is interesting to note that all three seasons characterized by mean climatological convection – spring, summer, and fall – exhibit anomalous descent in the 2-K SST warming experiment. In both summer and fall, the maximum descent anomaly is more modest at $\sim$15% (not shown). Furthermore, while the weakening of ascent occurs in all three seasons, there is only a substantial precipitation reduction in spring.

The net precipitation (precipitation minus evaporation, or $P - E$) decreases by $\sim$ 40% in spring, as opposed to only a few percents in summer and fall. Assuming steady state and a small role for horizontal advection in the moisture budget, one can approximate $P - E$ as $\left\{\overline{\omega}\frac{\partial\overline{q}}{\partial p}\right\}$. The $\sim$ 40% $P - E$ reduction in spring is caused by the relatively large fractional change in $\overline{\omega}$ noted above. In summer and fall, the increase

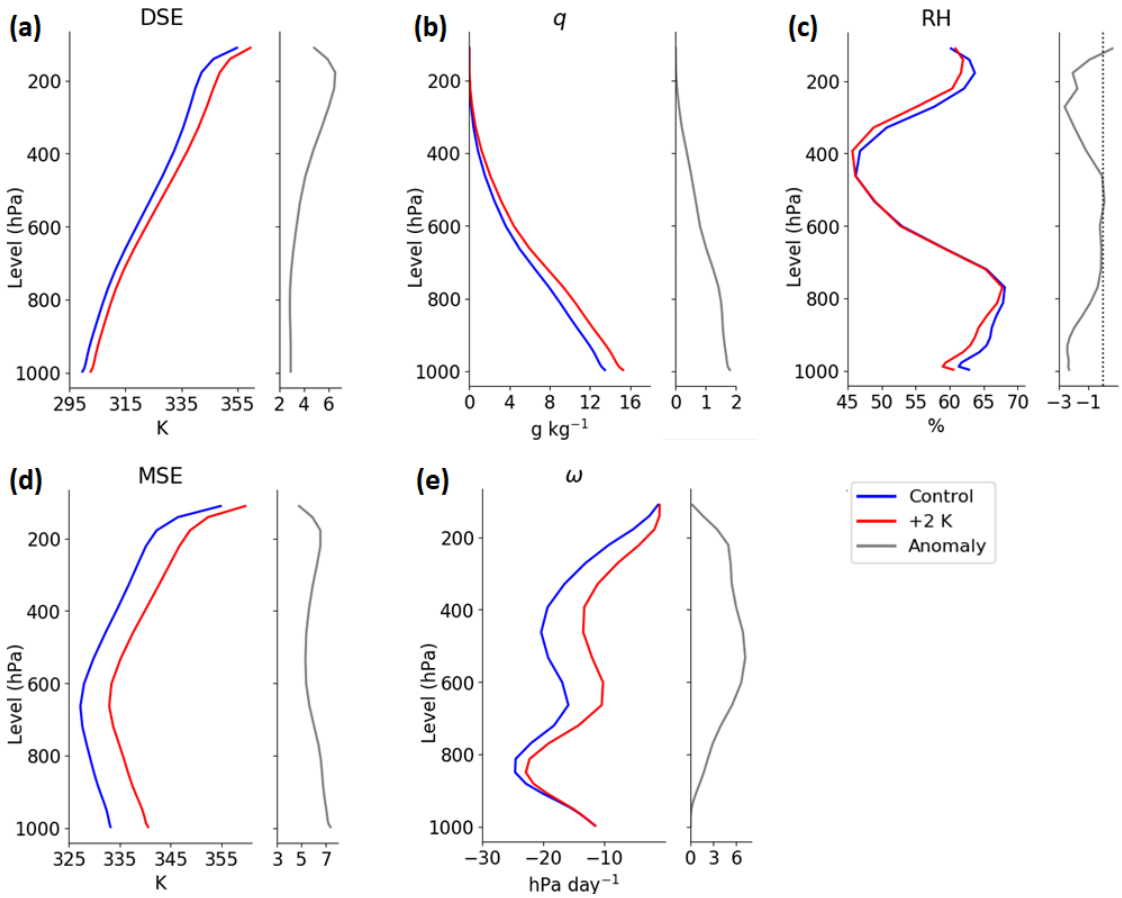



Figure 2.3: Vertical profiles of SON region-mean (a) dry static energy (DSE), (b) specific humidity, (c) relative humidity, (d) MSE, and (e) vertical pressure velocity. For each variable, control values are blue, +2 K results are red, and anomalies (2-K minus control) are plotted on a separate axis in gray.

in boundary layer moisture and thus $\frac{\partial \overline{q}}{\partial p}$ is sufficient to maintain the control $P - E$ given the more modest weakening of convection.

In spring, the 2-K uniform SST perturbation causes warming by more than 2 K over land, exceeding 3 K along the southern boundary of the monsoon sector (Fig. 2.4a). This land-amplified warming results from the differing dry and moist adiabatic lapse rates operating over land and ocean respectively, combined with the constraint of weak temperature gradients in the free troposphere (Byrne and O'Gorman, 2013). Specific humidity increases accompany the increased temperatures everywhere (Fig. 2.4b), but moisture limitations result in reduced low-level relative humidity across the

land domain, particularly in the southeastern part of the monsoon sector (Fig. 2.4c). The anomalous boundary layer moist static energy distribution also reflects the combined effects of the temperature and moisture increases (Fig. 2.4d). The prevailing MSE gradient is enhanced, with MSE increasing by over 7 K to the northwest and along the Andes and by 4-5 K to the southeast. In the eastern monsoon sector, the enhanced zonal MSE gradient is associated with the anomalous temperature gradient, while the moisture response underlies the MSE pattern change in the west.

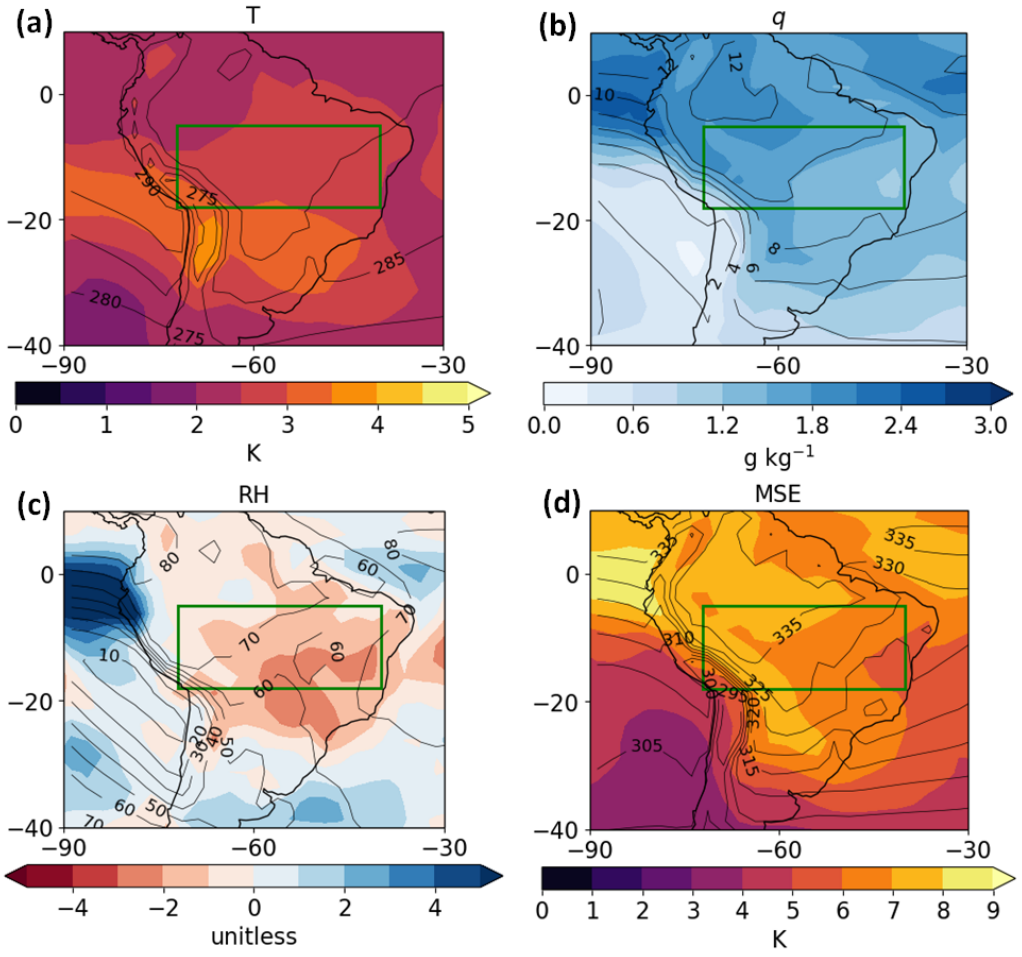



Figure 2.4: Spatial distributions of SON 850 hPa controls (contours) and anomalies (2-K minus control, shadings) of (a) temperature, (b) specific humidity, (c) relative humidity, and (d) MSE. The monsoon sector is outlined in green.

Overall, the 2-K SST warming simulation has a drier monsoon onset season in South America, supporting the conclusions of previous studies (e.g. Lau et al., 2013; Boisier et al., 2015; Biasutti and Sobel, 2009; Seth et al., 2011). The present experiment demonstrates that uniform SST warming alone can drive this change in seasonality. As described in Section 1.3, spring drying would strain the Amazon rainforest ecosystem. In the following section we investigate the cause of spring drying with the MSE budget.

### 2.4.3 Mechanisms of drying

To better understand the simulated spring drying, we examine the MSE budget regulation in the control experiment as well as its response to SST warming. The terms of the column-integrated MSE budget (Eq. 2.1) are computed using the adjustment procedure of Hill et al. (2017, c.f. their Appendix A, B). The eddy term is based on deviations from monthly means. Table 2.1 provides season- and region-mean values over the South American monsoon sector. In spring, $\overline{F}_{net}$ (69.5 W m$^{-2}$) is balanced primarily by horizontal MSE advection (37.9 W m$^{-2}$) , with vertical advection (6.01 W m$^{-2}$) in a supporting role (Fig. 2.5, Table 2.1). Transient eddy MSE export completes the balance (22.0 W m$^{-2}$). This is a deviation from the Neelin and Held (1987) picture of precipitating tropical regions in which horizontal MSE advection is negligible. The vertical MSE advection term makes a larger relative contribution to column-integrated MSE export in the western half of the domain (Fig. 2.5b), where rainfall is stronger (Fig. 2.1b).

The leading-order balance of the perturbed SON MSE budget (2-K minus control) is between the horizontal and vertical advection terms, namely $\delta\left\{\overline{\omega}\frac{\partial\overline{h}}{\partial p}\right\} \approx -\delta\{\overline{\mathbf{v}}\cdot\nabla_p\overline{h}\}$, with the vertical contribution to MSE export reduced and the horizontal component enhanced (Fig. 2.6, Table 2.1). While the region remains moderately rainy (3.6 mm day$^{-1}$) in the 2-K warming experiment, the region-mean column-integrated

Table 2.1: SON column-integrated MSE budget terms (W $m^{-2}$) in the control simulation, and anomalies (2-K minus control) averaged over the South American monsoon sector.

| | Control | Anomaly |
|---|---|---|
| $\overline{F}_{net}$ | 69.5 | -1.5 |
| $\frac{\partial}{\partial t}\{\overline{\mathcal{E}}\}$ | 3.0 | 1.7 |
| $\{\overline{\mathbf{v}} \cdot \nabla_p \overline{h}\}$ | 37.9 | 6.2 |
| $\left\{\overline{\omega}\frac{\partial \overline{h}}{\partial p}\right\}$ | 6.0 | -9.4 |
| $\nabla \cdot \{\overline{h'\mathbf{v}'}\}$ | 22.0 | -0.3 |

vertical MSE advection turns into a net import (-3.4 W $m^{-2}$), amounting to a negative GMS. Based on a linear decomposition, the increase in horizontal MSE advection (by 6.2 W $m^{-2}$) is almost entirely thermodynamic, associated with the climatological horizontal winds operating on the anomalous horizontal gradient of MSE: $\{\overline{\mathbf{v}_{ctl}} \cdot \delta\nabla_p \overline{h}\}$, where $\mathbf{v}_{ctl}$ is the control experiment horizontal wind vector (Fig. 2.1c). Due to the enhanced horizontal MSE gradient, the incursion of low MSE air by easterly inflow from the neighboring Atlantic ocean more effectively ventilates the region in the 2-K warming experiment than in the control simulation. The enhanced horizontal MSE advection is primarily in the eastern part of the monsoon sector (Fig. 2.6a) where the anomalous MSE gradient (Fig. 2.4d) is most aligned with the zonal climatological flow (Fig. 2.1c).

We examine the separate contributions of dry static energy (DSE), $s = c_p T + gz$, and moisture terms (LE), $L_v q - L_f q_{ice}$, to the column-integrated MSE budget (Table 2.2). The 6.2 W $m^{-2}$ increase in region-mean horizontal MSE advection is due to the DSE component (7.2 W $m^{-2}$), and offset only slightly by the moisture term. This is a distinction from the "upped-ante" mechanism described by Chou and Neelin (2004) which is driven by anomalous moisture advection along convective margins. In the case of uniform warming on a well-watered surface, enhanced MSE gradients arise

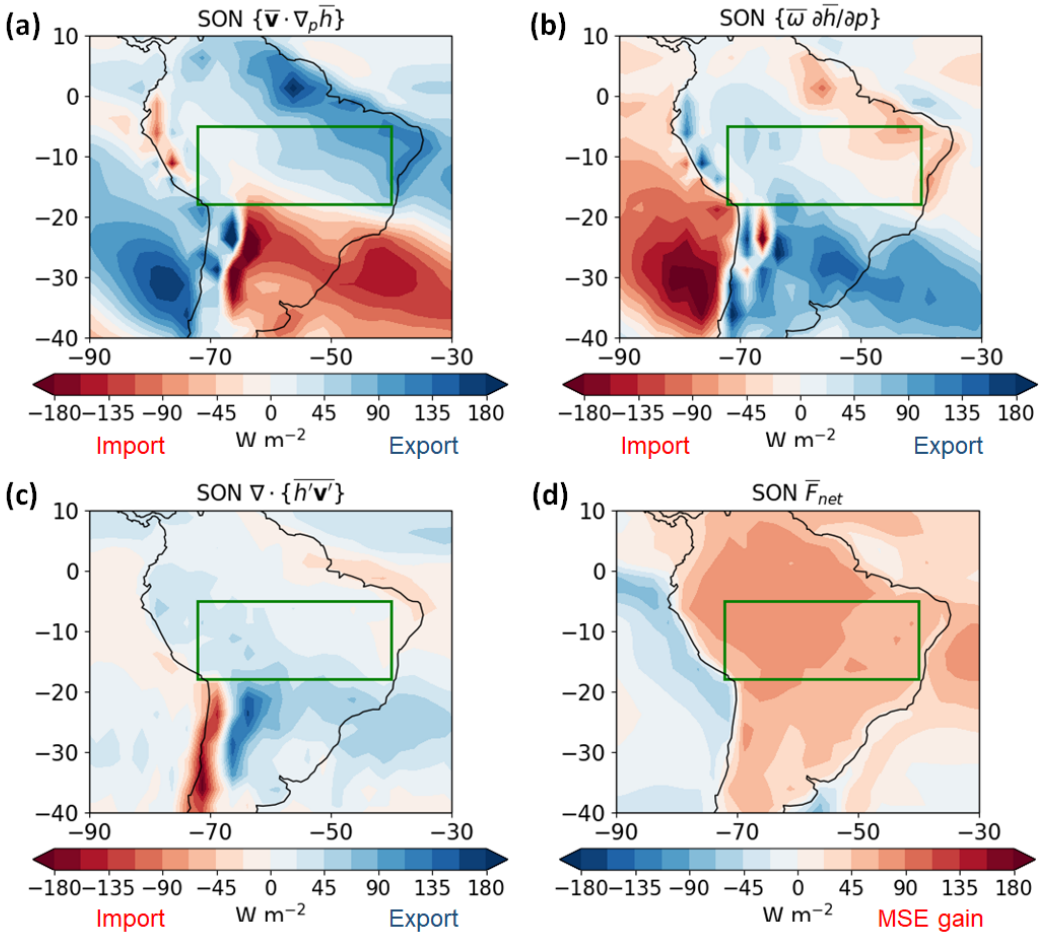



Figure 2.5: Terms of the SON column-integrated MSE budget in the AM4 control simulation: (a) horizontal MSE advection, (b) vertical MSE advection, (c) transient eddy MSE flux divergence, and (d) net energetic forcing. Region mean values over the monsoon sector, outlined in green, are presented in Table 2.1.

from the nonlinearity of the Clausius-Clapeyron relation: the specific humidity ($q$) increase per unit warming is higher at higher temperatures (Chou and Neelin, 2004; Neelin et al., 2003; Boos and Hurley, 2013). In the present 2-K warming experiment, by contrast, the enhanced warming over land compared to the adjacent Atlantic underlies the orientation of the anomalous MSE gradient in the eastern half of the monsoon domain, while the specific humidity anomaly is more uniform between land and ocean (Fig. 2.4). Relative humidity reductions are accordingly more pronounced in the east (Fig. 2.4c). Due to the warming pattern dictated by land geometry and

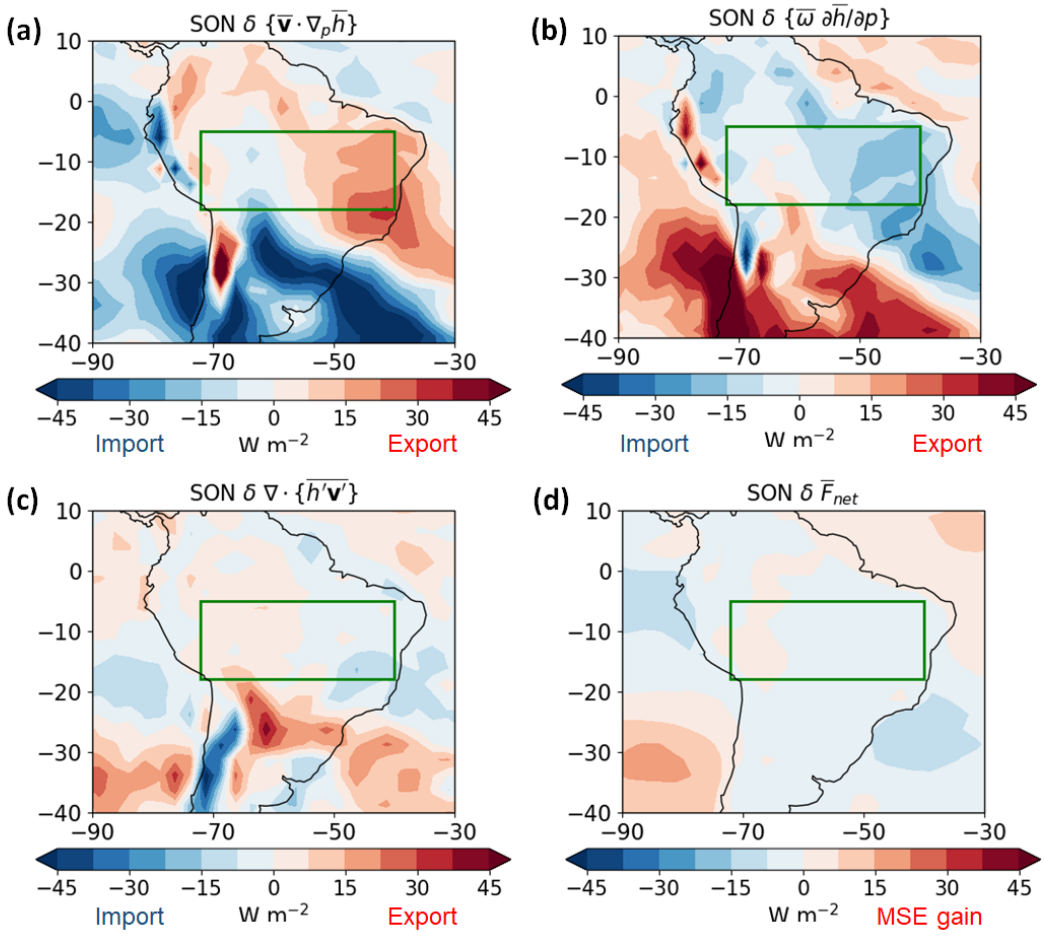



Figure 2.6: Anomalies (2-K minus control) of the SON MSE budget terms: (a) horizontal MSE advection, (b) vertical MSE advection, (c) transient eddy MSE flux divergence, and (d) net energetic forcing. Region mean values over the monsoon sector, outlined in green, are presented in Table 2.1.

surface properties, DSE advection increases thermodynamic ventilation of the South American monsoon sector in spring. While the MSE budget analysis alone indicates a common drying mechanism with that described by Chou and Neelin (2004), the subsequent decomposition demonstrates that local features can impact the relative importance of dry and moist processes. The prevalence of DSE advection as a tropical drying process has not previously been highlighted.

The anomalous MSE export via column integrated horizontal advection elicits compensating import by the vertical advection. The control simulation $\omega$ profile

Table 2.2: Decomposition of the SON column-integrated MSE budget terms (W $m^{-2}$) into dry static energy (DSE or $s$) and latent energy ($LE$) components in the control simulation, and anomalies (2-K minus control) averaged over the South American monsoon sector. Positive anomalies represent a greater contribution to MSE export.

| | Control | Anomaly |
|---|---|---|
| $\{\overline{\mathbf{v}} \cdot \nabla_p \overline{s}\}$ | 16.7 | 7.2 |
| $\{\overline{\mathbf{v}} \cdot \nabla_p \overline{LE}\}$ | 21.4 | -0.8 |
| $\left\{\overline{\omega}\frac{\partial \overline{s}}{\partial p}\right\}$ | 85.1 | -20.3 |
| $\left\{\overline{\omega}\frac{\partial \overline{LE}}{\partial p}\right\}$ | -79.1 | 10.9 |
| $\nabla \cdot \{\overline{s'\mathbf{v}'}\}$ | 2.5 | -0.1 |
| $\nabla \cdot \{\overline{LE'\mathbf{v}'}\}$ | 19.2 | -0.2 |

exhibits two ascent peaks, at ∼825 hPa and ∼450 hPa (Fig. 2.3e). In the 2-K experiment, anomalous subsidence throughout the column peaks near 500 hPa, reflecting weaker and shallower mean convection (Fig. 2.3e). As horizontal MSE gradients increase, column-integrated MSE is increasingly damped over the South American monsoon sector in spring, which is characteristic of substantial inflow up those gradients. In this way, barring compensating changes in eddies or $F_{net}$, regions can become less favorable for convection and exhibit weaker ascent and precipitation.

The MSE budget analysis informs a physical understanding of the regional precipitation response, but it does not foreclose the possibility that other processes, such as synoptic dynamics, also play a role. Analysis along these lines demonstrates that changes in the low level horizontal flow field, in particular the low level jet (LLJ), make a secondary contribution to the drying over the South American monsoon sector. A low level jet is a meridional wind maximum in the lower 1-2 km of the atmosphere that forms to the east of a mountain barrier, in this case the Andes. This seasonally persistent synoptic feature transports moisture poleward from the Amazon to the La Plata river basin, feeding mesoscale convective systems there. A northerly LLJ

regime causes low level moisture divergence over the Amazon and convergence and anomalous precipitation in the La Plata Basin (Wang and Fu, 2004). As in two previous global warming simulation studies, in the 2-K experiment the LLJ strengthens in spring, as measured by the South American LLJ index: the mean 850 hPa meridional winds averaged over the region ($15 - 25^\circ$ S, $65 - 55^\circ$ W) (Wang and Fu, 2004). In the 2-K experiment, the LLJ index northerlies strengthen by 0.8 m $s^{-1}$ or 26 % ($p < 0.001$) (Fig. 2.7a). This is consistent with the simulated precipitation increases south of $\sim 30^\circ$ S (Fig. 2.2c). The South American LLJ moisture transport is quantified as the region-mean meridional component of the column-integrated moisture flux $Q_\phi = \{\overline{q} \cdot \overline{v}\}$. In the 2-K experiment, the southward LLJ $Q_\phi$ increases by a magnitude of 35 kg $s^{-1}$ $m^{-1}$ or $\sim 40\%$ (Fig 2.7b). As in previous studies, anomalous moisture transport by the LLJ exacerbates the spring season drying over the monsoon sector (Soares and Marengo, 2009; Seth et al., 2010).

While in austral summer the LLJ is driven by local boundary layer processes, in other seasons, including spring, it is associated with upstream westerly winds which interact with the Andes and induce downstream cyclones via lee cyclogenesis (e.g. Wang and Fu, 2004). In the AM4 2-K warming simulation, the SON Pacific subtropical high weakens, consistent with increased westerly flow over the Andes (Fig. 2.7a). Based on this dynamic mechanism, it is plausible that the strengthening of the LLJ, a synoptic feature, is driven by the broader changes in the large-scale subtropical circulation. Other features of the South American circulation, such as the South Atlantic Convergence Zone and the Bolivian High (not shown), show muted responses to uniform warming in spring.

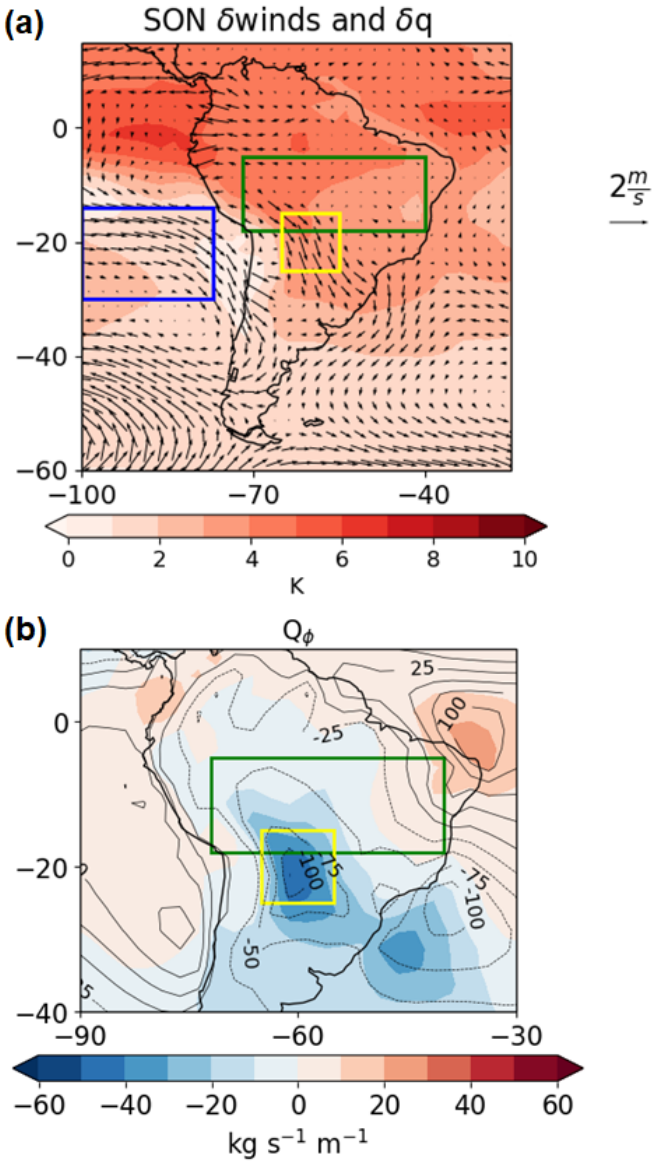



Figure 2.7: (a) Anomalous (2-K minus control) SON winds and moisture at 850 hPa. The green box delimits the monsoon sector. The yellow box outlines the low level jet sector, where winds are influenced by the strength of the westerlies in the region outlined in blue. (b) The SON column-integrated meridional moisture transport in the control (contours) and anomaly (shading)

## 2.5 Discussion

This study underscores that a uniform perturbation, in this case SST warming, can have uneven hydrological impacts in space and time. The analysis of the spring season response to SST warming enables us to diagnose a mechanism of drying in the South American monsoon sector. Comparing the climatological conditions and the precipitation response across all seasons allows us to identify the conditions that render one location or season more susceptible to drying than another. The results suggest that there are at least two necessary conditions for a significant precipitation reduction. The first condition is that the sector's climatological MSE ventilation is dominated by the horizontal, rather than the vertical, advection term. The second one is that the horizontal MSE advection increases in the perturbed climate. This provides a theoretical framework in which one can contrast spring with the other two raining seasons (summer and fall) to better understand the seasonal variations in the South American monsoon precipitation response.

The relative importance of vertical to horizontal MSE advection varies throughout the year, as reflected by the seasonal cycle of the climatological region-mean ratio $\left\{\overline{\omega}\frac{\partial\overline{h}}{\partial p}\right\}/\{\overline{\mathbf{v}}\cdot\nabla_p\overline{h}\}$ (Fig. 2.8). We abbreviate this ratio as $V_{MSE}/H_{MSE}$ for vertical and horizontal MSE advection. The column-integrated horizontal MSE advection is positive throughout the seasonal cycle, ventilating the region. By contrast, the vertical MSE advection contributes to export in the rainy season and import in the dry season. The $V_{MSE}/H_{MSE}$ ratio exceeds one in the summer rainy season, maximizing in December at 1.1, and minimizes in June at -1.7. In spring (SON), $V_{MSE}/H_{MSE}$ is small and positive (0.16), meaning that both terms contribute to column-integrated MSE export, with horizontal MSE advection dominating by a factor of approximately six. In comparison, the fall season (MAM) has a $V_{MSE}/H_{MSE}$ of 0.51. Thus in both transition seasons, horizontal MSE advection trumps vertical advection in the column-integrated MSE export, though only by a factor of two in fall. However, the

precipitation in fall is insensitive to SST warming, remaining within 1% of its control value of 6.9 mm day$^{-1}$, while it decreases substantially in spring. Why does the drying mechanism identified for spring, instigated by an increase in horizontal MSE advection, not occur in fall?

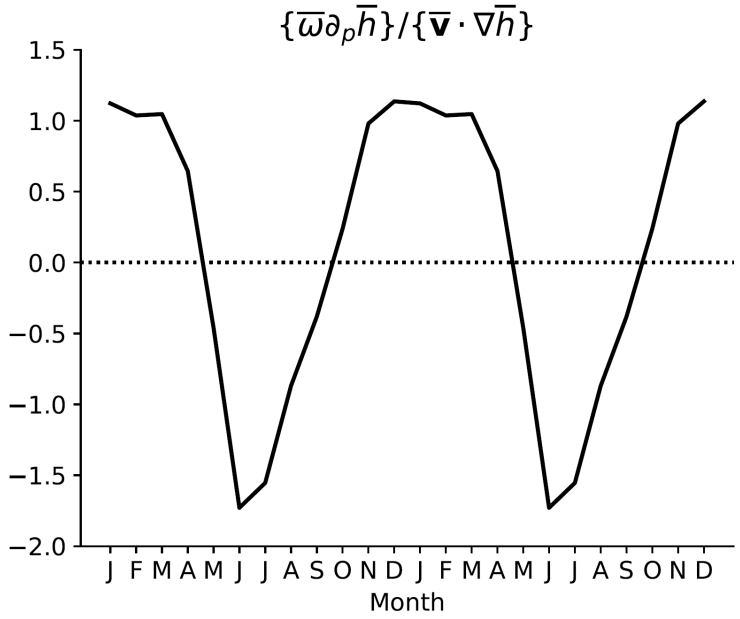



Figure 2.8: Seasonal cycle of $V_{MSE}/H_{MSE}$ averaged over the South American monsoon sector in the control simulation .

Emerging from the dry season, the control near-surface relative humidity in spring is ∼60%, substantially lower than ∼80% in fall, which follows the peak monsoon season. Under these humid conditions, the fall season does not exhibit the land-sea warming differential seen in spring (Fig. 2.4a), nor the associated anomalous zonal MSE gradient between the South American land mass and the Atlantic ocean (Fig. 2.4d). Instead, the fall season anomalous MSE gradient is predominantly meridional. Accordingly, the easterly winds flowing onto the continent do not operate on the anomalous MSE gradient, impeding the thermodynamic drying mechanism which operates effectively in spring. A linear decomposition confirms that there is minimal change in $\{\overline{\mathbf{v}_{ctl}}\cdot\delta\nabla_p\overline{h}\}$ due to SST warming; the change in horizontal MSE

advection in fall is almost entirely due to dynamic changes that advect relatively high MSE air into the region. In other words, the fall season does not satisfy the second condition for drying. Seasonal differences in land surface conditions, namely the moisture availability, play a key role in the distinct spring and fall hydrological responses to warming.

In summer (the peak rainy season), the horizontal MSE advection increases by $\sim$ 4 W m$^{-2}$ in the 2-K experiment, but this does not suppress precipitation. A possible reason is that summer does not satisfy the first condition for drying: the DJF $V_{MSE}/H_{MSE}$ ratio is $> 1$, implying a secondary role for horizontal advection in column-integrated MSE discharge, and thus reduced sensitivity to the enhanced horizontal MSE gradients. The monsoonal precipitation is driven by sufficiently vigorous and top-heavy convection that it withstands modest increases in the horizontal MSE advection.

## 2.6 Conclusions

In the GFDL AM4 model, uniform SST warming causes significant rainfall reductions in the South American monsoon onset season (spring). Several studies based on observations and comprehensive climate model simulations also conclude that climate change will impede spring precipitation in the monsoon sector (e.g. Lau et al., 2013; Boisier et al., 2015; Biasutti and Sobel, 2009; Seth et al., 2011; Wang et al., 2020). The present analysis demonstrates that this change in seasonality is linked to the uniform warming component of greenhouse gas induced climate change. The prospect of diminishing rainforests due to such a change in seasonality is of global concern due to the Amazon's unparalleled biodiversity and its major role in the carbon cycle.

The MSE budget is a useful theoretical framework for systematically diagnosing the mechanisms of precipitation change over land. The seasonal cycle of $V_{MSE}/H_{MSE}$

encapsulates the time-varying MSE budget regulation in the climatology. Based on the climatological MSE regime, one can identify regions and seasons in which rainfall is likely resilient to the impacts of SST warming, and those where precipitation is subject to change. Convective regions where horizontal MSE advection dominates the climatological MSE budget are prone to drying, but only do so if horizontal MSE advection increases in the perturbed climate (Fig. 2.9). The comparison of South American spring and fall illustrates that the horizontal MSE advection response is influenced by the land geometry and surface water availability which together determine the anomalous MSE pattern. Continued research to elucidate the seasonally varying influence of surface conditions on the hydrological response to warming will bolster regional climate projections.

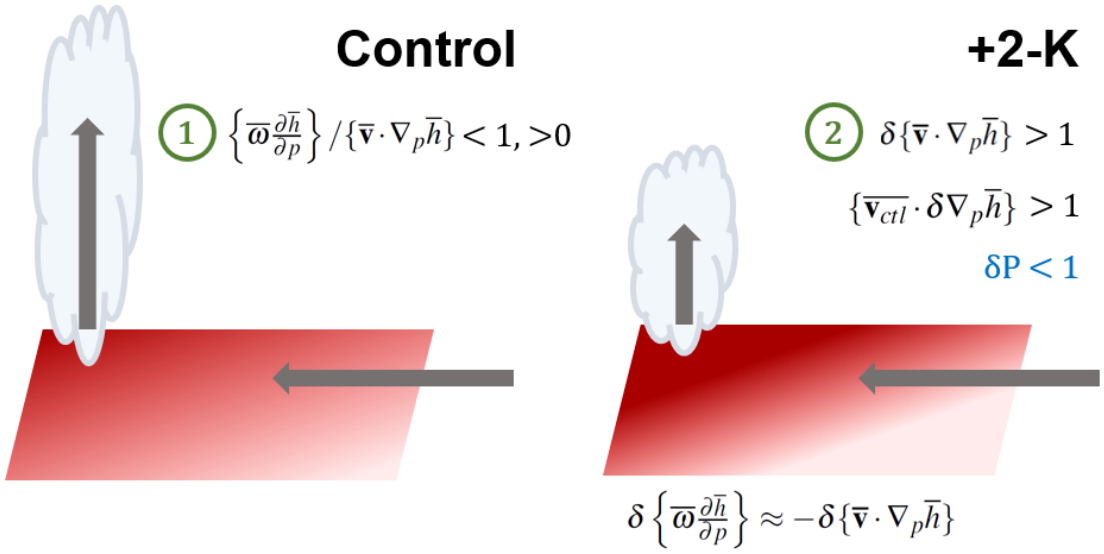



Figure 2.9: A depiction of the thermodynamic drying mechanism, with arrows representing mean winds and the red gradient indicating the MSE distribution. A region is susceptible to drying when the two criteria are satisfied: the climatological region-mean ratio of $V_{MSE}/H_{MSE}$ is positive and less than one, and the horizontal MSE advection increases in the perturbed climate. In the warmer climate, the mean winds act on enhanced horizontal MSE gradients, ventilating the monsoon sector and inhibiting convection and precipitation.

Further study of simulations with different climate perturbations, such as realistic greenhouse gas or aerosol forcing, will be useful to identify additional mechanisms of and conditions for precipitation change. The impact of SST warming on the full probability distribution of precipitation also warrants further study (e.g. Norris et al., 2019). The focus here on the mean precipitation response to uniform SST warming facilitates interpretation of certain robust impacts of climate change. The results provide valuable physical insights to better understand how increasing temperatures could cause severe drying in the South American monsoon onset season.

# Chapter 3

# Investigating the impact of land surface characteristics on monsoon dynamics with idealized model simulations and theories

## 3.1 Abstract

Monsoons emerge over a range of land surface conditions and exhibit varying physical characteristics over the seasonal cycle, from onset to withdrawal. Systematically varying the moisture and albedo parameters over land in an idealized modeling framework allows one to analyze the physics underlying the successive stages of monsoon development. To this end we implement an isolated South American continent with reduced heat capacity but no topography in an idealized moist general circulation model. Irrespective of the local moisture availability, the seasonal cycles of precipitation and circulation over the South American monsoon sector are distinctly monsoonal with the default surface albedo. The dry land case (zero evaporation) is characterized by

a shallow overturning circulation with vigorous lower-tropospheric ascent, transporting water vapor from the ocean. By contrast, with bucket hydrology or unlimited land moisture the monsoon features deep moist convection that penetrates the upper troposphere. A series of land albedo perturbation experiments indicates that the monsoon strengthens with the net column energy flux and the near-surface moist static energy with all land moisture conditions. When the land-ocean thermal contrast is strong enough, inertial instability alone is sufficient for producing a shallow but vigorous circulation and converging a large amount of moisture from the ocean even in the absence of land moisture. Once the land is sufficiently moist, convective instability takes hold and the shallow circulation deepens. These results have implications for monsoon onset and intensification, and may elucidate the seasonal variations in how surface warming impacts tropical precipitation over land.

## 3.2 Introduction

Despite the extensive research highlighted in Section 1, fundamental questions persist about the theoretical basis of monsoon formation. The complications introduced by zonally confined continental geometry, land surface moisture constraints, and albedo contrasts have yet to be fully elucidated (e.g. Zhai and Boos, 2015; Maroon and Frierson, 2016; Zhou and Xie, 2018; Levine and Boos, 2017). The chief purpose of this study is to determine the key mechanisms of monsoon formation across a broad range of climate conditions. The analysis focuses on the processes driving seasonal precipitation that would be relevant beyond the idealized model setting. Motivated by a recent work (Chapter 2, Smyth and Ming, 2020), we take the summer circulation over South American continental geometry as our focal point, but the analysis aims to elucidate the dynamics of a generic, deep tropical monsoon. In an idealized framework, the experiments map the parameter space of land albedo and moisture

conditions, with implications for the stages of seasonal monsoon development as well as the range of global monsoons with their diverse geographic and ecological settings. The holistic approach draws on numerous relevant theories and suggests some general principles regulating monsoon strength. Section 3.3 describes the idealized moist GCM and the suite of experiments. Section 3.4.1 presents the results for varying land moisture conditions, Section 3.4.2 is an MSE budget analysis, and Section 3.4.3 examines the land albedo perturbation experiments. Section 3.5 provides an overview of the monsoon formation mechanisms over the range of land surface conditions.

## 3.3 Experimental Design

We use an idealized moist general circulation model as described in Clark et al. (2018).The model has a three dimensional spectral dynamical core, and the highly simplified atmospheric physics largely follows Frierson et al. (2006), including simplified planetary boundary layer and convection schemes. Like Clark et al. (2018), we replace the gray-atmosphere radiation used in Frierson et al. (2006) with a full radiative transfer scheme (Paynter and Ramaswamy, 2014). This makes it feasible to explicitly simulate water vapor feedbacks. The simplified Betts-Miller (SBM) convection scheme has a default convective relaxation timescale ($\tau_{BM}$) of 2 hours. This timescale dictates how fast simulated profiles of temperature and humidity are relaxed to convectively adjusted reference states once certain criteria are met (Frierson, 2007). The SBM scheme represents shallow, non-precipitating convection by relaxing unstable temperature profiles to reference profiles, and triggers deep, precipitating convection when moisture and temperature profiles exceed stability thresholds, including a 70% relative humidity criterion. Precipitation can also form on the grid scale by removing water vapor in excess of saturation. Neither parameterized convection nor grid-scale precipitation gives rise to clouds. The impact of cloud feedbacks on

the monsoon depends on the net radiative effect of the clouds that form (Voigt et al., 2014); this is a source of uncertainty in climate modeling, and is not considered in the present study. While this compromises the realism of the simulations, it allows for a focus on more essential and robust aspects of the monsoon circulations. In Section 3.5 we compare the results to comprehensive atmospheric model simulations (GFDL AM4.1) that include clouds, topography, and more sophisticated physics, and discuss the relevance of the findings up the model hierarchy.

The lower boundary condition includes a slab mixed layer ocean with a heat capacity equal to 20 meters of water and a prescribed, time-invariant meridional oceanic heat flux, and an isolated South American continent with 10% of the slab ocean heat capacity (i.e. 2 meters of water). The choice of an isolated continent minimizes the broader climatic impact of land moisture and albedo perturbations by confining them to a comparatively small area, facilitating comparison between experiments. On the other hand, the realistic geometry enables more direct comparison of the monsoon sector with both observations and comprehensive model experiments, including the Geophysical Fluid Dynamics Laboratory (GFDL) AM4 simulations that motivate the present study (Smyth and Ming, 2020).

The South American continent has realistic geometry but no topography (i.e. completely flat), and does not include Central America. The exclusion of the Andes mountain range is notable given the attention placed on its climate significance in previous work. For example, the Andes act as a barrier shielding the continent from low MSE oceanic air (e.g. Garreaud and Aceituno, 2001) and support low level jet formation both by diverting easterly winds and via lee cyclogenesis (Wang and Fu, 2004). We expect the increased ventilation in the absence of the Andes Mountains to limit the southward extent of the monsoon compared to observations, as in Chou and Neelin (2001).

A suite of experiments forced with a modern-day seasonal cycle of insolation is designed to elucidate the impact of land moisture and albedo conditions on monsoon characteristics. Though the present study focuses on the case of South America as a bridge to our previous work, the use of an idealized model and the focus on mechanistic analysis should yield insights that inform our general understanding of monsoons. Zhou and Xie (2018) serves as a useful comparison point for our results as their model differs only in the lower boundary condition and their use of a gray radiation scheme. The three land moisture configurations include a "realistic" continent (R) with a bucket hydrology model governing potential evaporation, a "dry" (D) continent with zero evaporation, and a "wet" continent (W) in which the land is an infinite reservoir of moisture (i.e. the only distinction between land and ocean is in heat capacity). The bucket hydrology model (Manabe, 1969) in the R configuration scales the potential evaporation based on a bucket capacity (or field capacity) of 150 mm and a 0.75 saturation fraction, as in Vallis et al. (2018) and Clark et al. (2020). The bucket capacity sets a limit on moisture storage, and the saturation fraction determines that when the bucket level is below 75% the bucket capacity, the evaporative resistance parameter limits the evaporation to some fraction of the potential evaporation (see Vallis et al. (2018)).

For each moisture condition, R, D, and W, we perform six albedo perturbation experiments with land albedo prescribed to 0.1, 0.26, 0.3, 0.4, 0.5, 0.7, and 1.0. Note that 0.26 is the default surface albedo over both land and ocean, and is chosen to attain a realistic climate in the absence of clouds (Frierson et al., 2006). The name of an experiment contains a letter (denoting the moisture condition) followed by a number (denoting the albedo). For instance, R0.26 refers to the experiment in which one uses the bucket hydrology model and the default albedo of 0.26. To discern the effect of the convective relaxation time on the monsoon simulation, we examine three experiments in the R0.26 configuration with $\tau_{BM}$ varied to 4, 8, and 16 hours, as in

Clark et al. (2018). The $CO_2$ concentration is prescribed to 369.4 ppm, and $CH_4$ to 1.821 ppm. The experiments are run at T42 spectral resolution (64 latitude by 128 longitude gridpoints) with 30 vertical levels. Each simulation is run for 20 years with the final 15 years of daily output used for analysis.

## 3.4 Results

### 3.4.1 Varying land moisture conditions

Irrespective of the local moisture availability in the idealized model simulations, the seasonal cycle over the South American monsoon sector (5-18° S, 40-72° W) is distinctly monsoonal in all three experiments with the default surface albedo (0.26) (Fig. 3.1a). Modest precipitation commences in October, two to three months after surface temperatures ($T_{surf}$) shift to a warming trajectory in late winter (Fig. 3.1b). With bucket hydrology (R0.26), a maximum rainfall rate of 6.2 mm $d^{-1}$ occurs in February, and without a local moisture source (D0.26), the peak monthly mean rainfall of 4.4 mm $d^{-1}$ occurs a month earlier, in January. When local moisture is unlimited (W0.26), rainfall maximizes at 9.1 mm $d^{-1}$ in February. [Throughout the chapter, the monsoon season refers to January to March (JFM), the period encompassing the highest mean rainfall rate.] In R0.26, $T_{surf}$ decreases as precipitation intensifies in JFM because in a moisture-limited regime, latent heat fluxes can increase at the expense of sensible heat fluxes (e.g. Berg et al., 2015). In D0.26 and W0.26, this coupling is eliminated since the local moisture is externally controlled. This may partly explain why $T_{surf}$ in the dry and wet cases is relatively flat during the monsoon season. In all experiments, precipitation rapidly retreats from April through June, and the dry season extends from July through September (JAS). During this time, there is virtually zero rainfall when local moisture fluxes are limited or disabled, while the mean precipitation hovers around 1 mm $d^{-1}$ in the W0.26 experiment (Fig. 3.1a). Inso-

lation minimizes in June, and minimum surface temperatures lag this by one month in the R0.26 and D0.26 experiments and by two months in W0.26 (Fig. 3.1b). In D0.26, surface temperatures respond more strongly to the insolation forcing without the moderating effect of latent heat fluxes on the surface energy balance. The D0.26 experiment exhibits the lowest amplitude annual cycle of precipitation, but the most seasonal variation of surface temperature (13 K range, compared to 11 K in R0.26 and 8 K in W0.26).

From a net precipitation perspective ($P - E$) (equivalent to the large-scale moisture convergence), the rainy season disparity between experiments is smaller, given the substantial enhancement of evaporation in the R and W experiments (Fig. 3.1c). Note that there is no land evaporation in the D experiment, so $P - E$ is the same as $P$. The JFM mean $P - E$ is similar in D0.26 (4.2 mm $d^{-1}$) and W0.26 (3.1 mm $d^{-1}$), which underscores the prominent role of the large-scale circulation in importing moisture from the ocean in both extreme cases. The $P - E$ is lower in R0.26 (1.8 mm $d^{-1}$); moisture convergence is higher with dry or saturated land than with bucket hydrology. During the dry season, the disparity in $P - E$ is greater than that in precipitation; the JAS mean $P - E$ is negative in R0.26 (-0.33 mm $d^{-1}$) and W0.26 (-2.6 mm $d^{-1}$). In W0.26, $P - E$ remains negative into the monsoon onset season (October through December, or OND) before increasing sharply. In the W0.26 simulation this continental region serves as a prominent net moisture source for much of the year, an unrealistic consequence of simulating land without a limit on potential evaporation. Nonetheless, the magnitude and phasing of the precipitation in W0.26 is remarkably similar to the observed 1997-2015 annual cycle from the Global Precipitation Climatology Project v2.3, especially from January to August (Fig. 3.1a). In this model, a saturated land surface produces the most realistic seasonal cycle of precipitation over the monsoon sector in terms of magnitude and timing; perhaps the saturated land best represents the strong evapotranspiration from vegetation in this region. In all

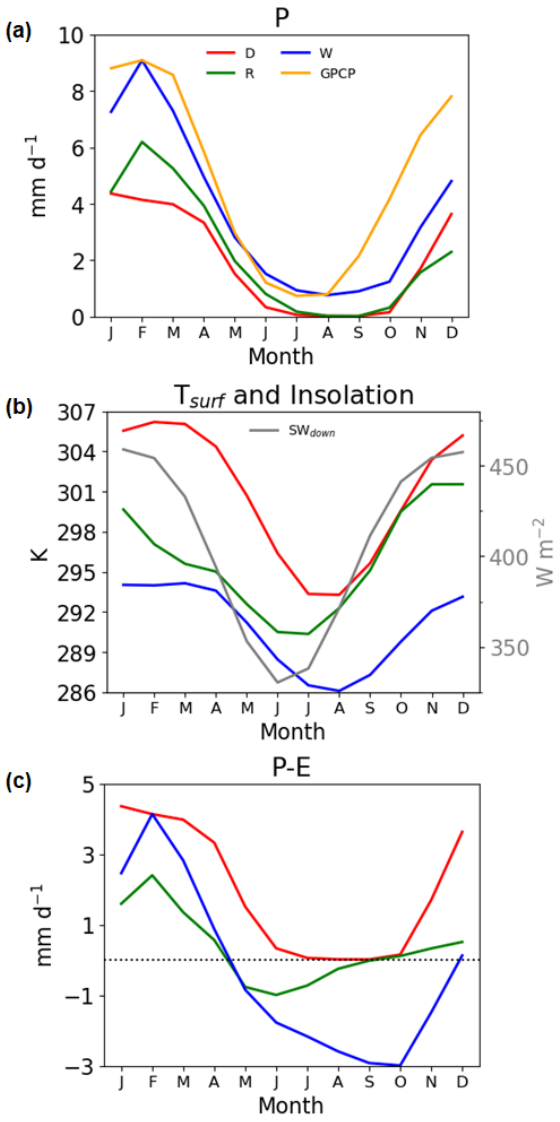



Figure 3.1: Seasonal cycles of region-mean (a) precipitation, (b) surface temperature and insolation, and (c) net precipitation ($P - E$) over the South American monsoon sector in the D0.26, R0.26, and W0.26 experiments.

three idealized model experiments the monsoon onset season precipitation is delayed and substantially weaker than observed, underlying a rather abrupt transition.

Despite the simplicity of the model configuration, especially in the absence of the Andes Mountains, the spatial distribution of monsoonal precipitation is largely consistent with observed patterns (Fig. 3.2), suggesting that the realistic geometry and the differing heat capacity of land and ocean are sufficient to induce a fairly realistic

monsoonal climate in the presence of insolation forcing. The key discrepancy in the atmospheric circulation without the Andes is that low-level westerly flow from the tropical Pacific contributes to the continental moisture convergence (Fig. 3.3). This westerly inflow is particularly strong in D0.26, where a cyclonic circulation on the western continent (Fig. 3.3a) produces a precipitation maximum near 70° W, with a relatively narrow rainfall band extending across the width of the monsoon sector (Fig. 3.2a). Precipitation exceeding 4 mm $d^{-1}$ extends from the east coast to 60° W in R0.26, with the strongest mean precipitation near 40° W (Fig. 3.2b). When surface moisture is unlimited, the monsoon is coherent with the oceanic Intertropical Convergence Zone (ITCZ) both west and east of the continent, though the precipitation has a broader southward extent over South America (Figs. 3.2c, 3.5c).

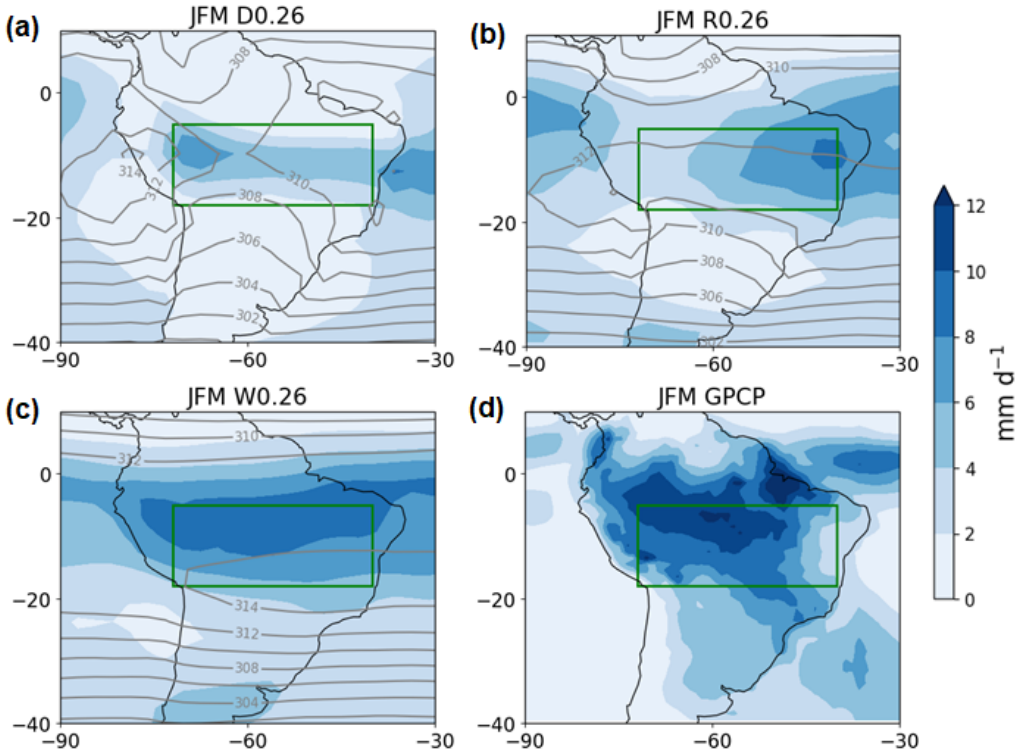



Figure 3.2: JFM mean distributions of precipitation (shading) in mm $d^{-1}$ and 973 hPa MSE (contours) in Kelvin in the (a) D0.26, (b) R0.26, and (c) W0.26 simulations and (d) GPCP v2.3 1997-2015 precipitation observations. The green box outlines the monsoon sector

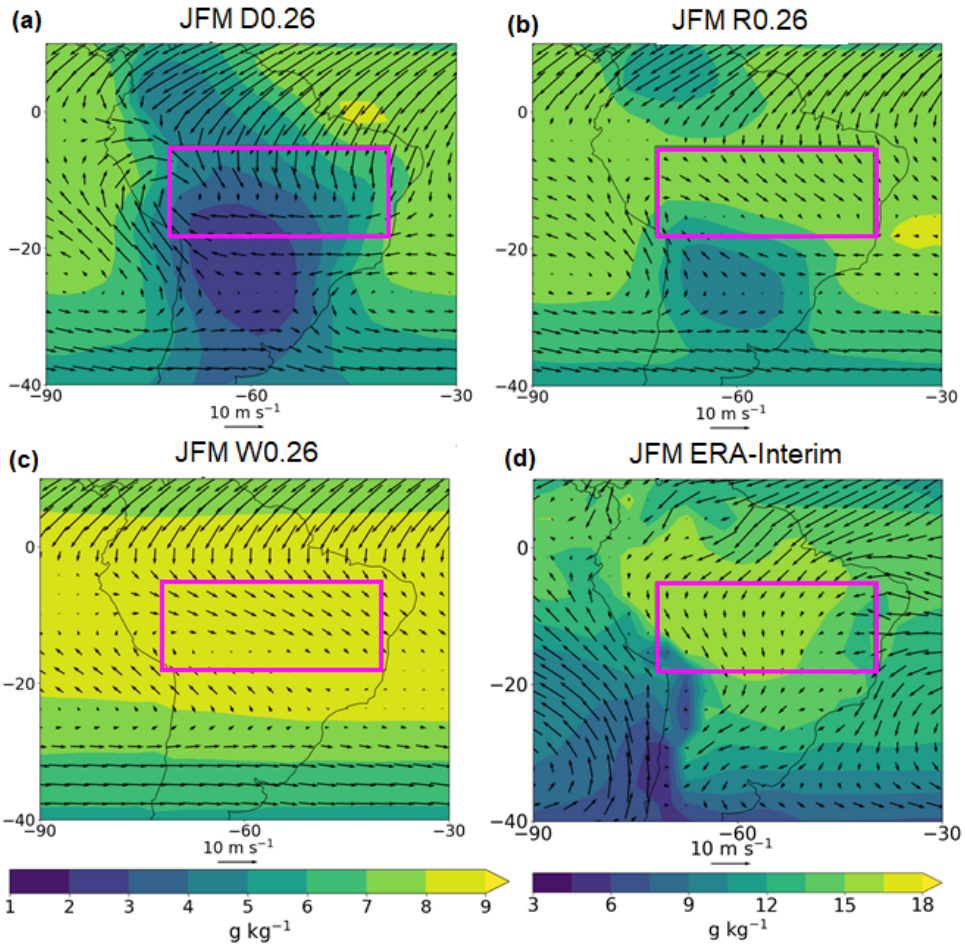



Figure 3.3: JFM mean distributions of 920 hPa specific humidity (shading) and horizontal winds (vectors) in (a) D0.26, (b) R0.26, and (c) W0.26 and at 925 hPa and for (d) ERA-Interim reanalysis, interpolated to the idealized model grid resolution. The model results (a-c) use the colorbar below subplot (c). The magenta box denotes the monsoon sector.

One notable feature in the simulations is the limited southeastward extension of the South Atlantic Convergence Zone (SACZ), a convective band that emanates from the Amazon basin over the South Atlantic Ocean. Previous work suggests that the SACZ forms when midlatitude fronts stall at longitudes with enhanced tropical convection and Rossby waves propagate equatorward (Nieto Ferreira and Chao, 2013; Van Der Wiel et al., 2015). In a series of aquaplanet experiments, Nieto Ferreira and Chao (2013) find that an SACZ-like feature develops when a prescribed patch of

enhanced tropical convection attains sufficient strength and poleward extent. In line with Kodama (1992, 1993), they emphasize that strong poleward low-level flow on the eastern flank of the monsoon region, or along the west of the subtropical high, is crucial for moisture convergence and SACZ formation. The underdevelopment of the SACZ may be attributed to discrepancies in the location and intensity of such a low-level jet in the idealized simulations. In all three experiments, poleward flow on the eastern coast of the continent does not extend poleward of 15°S (Fig. 3.3). In R0.26 and W0.26, the winds have a northwesterly orientation and are relatively weak, possibly due to the weaker land-ocean thermal gradients.

Like the magnitude of the precipitation, the region-mean near-surface (973 hPa) JFM MSE increases with local moisture availability. The MSE or h is defined as $h = c_pT + gz + L_vq - L_fq_{ice}$, where $c_p$ is the heat capacity of air at constant pressure, $T$ is temperature, $g$ is the gravitational constant, $z$ is geopotential height, $L_v$ is the latent heat of vaporization of water, and $q$ is specific humidity. In D0.26, the near-surface MSE is lower over the central monsoon sector than the surrounding coastal land, which is mirrored by the precipitation distribution (Fig. 3.2a). The MSE distribution is more uniform over land and ocean in R0.26 and W0.26 (Fig. 3.2b, c). In R0.26 the highest near-surface MSE contour bisects the maximum precipitation, and in W0.26, the near-surface MSE is highest just poleward of the strongest precipitation, consistent with CQE theory (Emanuel, 1995; Privé and Plumb, 2007a; Nie et al., 2010). In Section 3.4.3 we examine the extent to which the MSE distribution guides the precipitation when land albedo is varied (Hurley and Boos, 2013).

While each of these baseline experiments exhibits a monsoonal climate, the precipitation originates via different pathways in the model. With dry land, all moisture for precipitation derives from oceanic regions, so the monsoon sector is particularly reliant on easterly and westerly inflow of moist air from the tropical ocean. With unlimited moisture, the mean JFM evaporation rate is 60% of the precipitation rate,

which points to the substantial local moisture recycling evident from the $P - E$ results. Additionally, in D0.26, the rainy season precipitation (4.2 mm $d^{-1}$) derives almost exclusively from large-scale processes, with precipitation occurring when an entire grid box reaches saturation (not shown). By contrast, in the R0.26 (5.3 mm $d^{-1}$) and W0.26 (7.8 mm $d^{-1}$) experiments, JFM precipitation is largely produced by the parameterized Betts-Miller convection scheme (88% and 96%, respectively). Given the 70% relative humidity threshold in the SBM convection scheme, the ratio of convective to large-scale strongly depends on the near-surface humidity (Frierson, 2007), a point to which we will return.

The underlying large-scale circulation characteristics differ markedly across the range of land moisture conditions. The monsoon-sector mean ascent profiles in the R0.26 and W0.26 experiments indicate top-heavy moist convection that penetrates the upper troposphere, with vertical velocity maxima ( 50 and 70 hPa $d^{-1}$, respectively) at approximately 400 hPa (Fig. 3.4a). The dry land case is characteristic of a shallow overturning circulation with vigorous ascent; the maximum vertical pressure velocity ($\omega$) is 120 hPa $d^{-1}$ at 750 hPa (Fig. 3.4a). Though the ascent profile is relatively shallow, weaker ascent does penetrate to 250 hPa.

The region-mean MSE profiles also reflect the differing nature of the monsoon across moisture conditions (Fig. 3.4b). Although MSE decreases with height in the lower troposphere in all cases before starting to increase, the location of the MSE minimum becomes progressively lower in height with the increasing availability of moisture. Note that the observed tropical MSE profile typically shows a minimum in the mid-troposphere (around 600 hPa) (Back and Bretherton, 2006). A possible reason is that the free troposphere in the idealized simulations is biased dry, presumably due to the absence of moistening through convective detrainment of cloud condensates. The comparably low near-surface MSE in D0.26 demonstrates the strong effect of local moisture limitations on the overlying atmosphere.

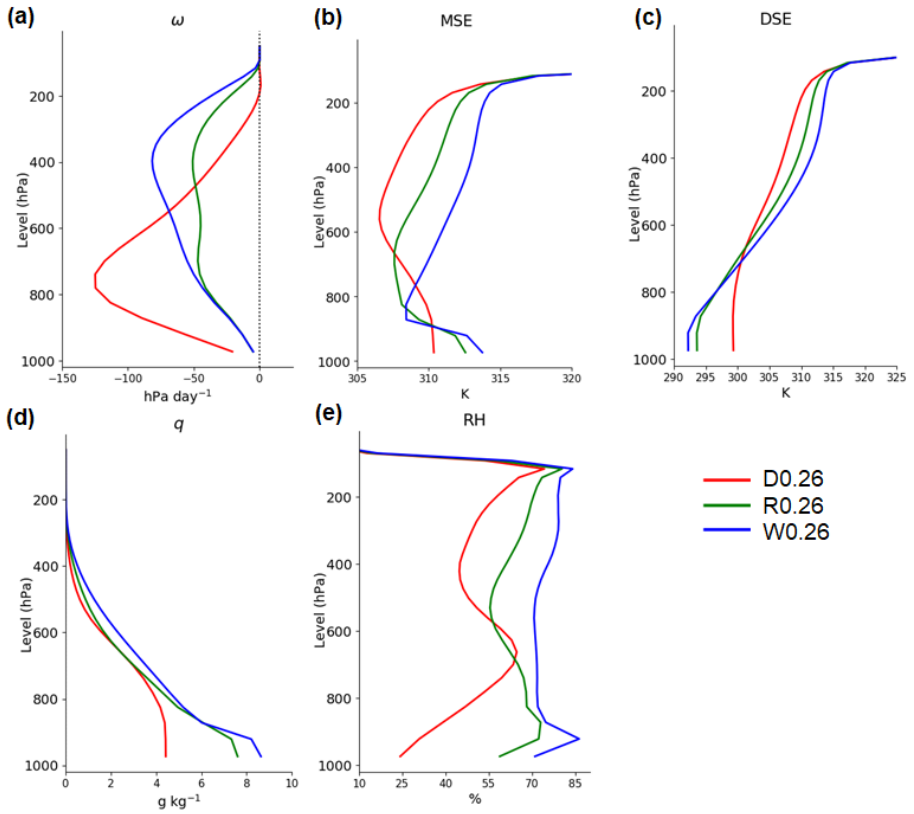



Figure 3.4: JFM monsoon sector-mean vertical profiles of (a) vertical pressure velocity, (b) MSE, (c) DSE, (d) specific humidity, and (e) relative humidity in the three baseline experiments.

The R0.26 and W0.26 profiles are firmly under convective quasi-equilibrium (CQE) control, with precipitation produced primarily via the simplified Betts-Miller (SBM) convection scheme. It seems questionable whether this is the case for D0.26, in which the parameterized convection ceases to operate and precipitation is produced exclusively through large-scale processes. However, the resolved (grid-scale) convection, albeit pathological, may still play a role in establishing a linkage between near-surface and upper-tropospheric MSE.

It is interesting to think about what controls the upper-tropospheric MSE in these experiments. CQE states the expectation that in convecting regions, one should see covariation of boundary layer equivalent potential temperature and the upper-

tropospheric saturation value (e.g. Nie et al., 2010). The free tropospheric saturation value depends on temperature only, so maxima in boundary layer $\theta_e$ should correspond to overlying maxima in free-tropospheric temperature. In the weak temperature gradient (WTG)/CQE framework (e.g. Byrne and O'Gorman, 2013; Hill et al., 2017; Zhang and Fueglistaler, 2020), the upper-tropospheric MSE throughout the inner tropics is dictated by the highest near-surface MSE. Fig. 3.5 shows that the highest near-surface MSE is located over the land monsoon region and the adjacent ocean in R0.26 and W0.26. In both cases, the upper tropospheric temperatures are fairly uniform, varying by less than 3-K in the inner tropics, as expected due to WTG dynamics (Fig. 3.11). The warmest temperatures extend over the monsoonal precipitation and near-surface MSE maxima, in accordance with the CQE framework. In D0.26, the maximum MSE is west of the land precipitation maximum, outside the high-precipitation contours where convection would convey this MSE maximum to the upper-troposphere. The D0.26 experiment stands out in that the upper-tropospheric temperature is lowest over the monsoon sector, directly above the local precipitation maximum. The bottom-heavy convection indeed leads to some deviation from CQE conditions over dry land (Fig. 3.4a). Despite this, continental precipitation in D0.26 appears near the near-surface MSE maximum along the western continental coast (Fig. 3.5).

The impact of varying land moisture availability is also evident in the vertical distributions of several other key variables. The dry static energy (DSE) profiles reflect hotter near-surface conditions in the D0.26 experiment as well as a much deeper boundary layer in which quasi-conserved quantities such as DSE are relatively well-mixed (Fig. 3.4c). This homogenization occurs partly via non-precipitating (dry), shallow convection in the SBM convection scheme (Frierson 2007). Near-surface DSE is highest in the D0.26 experiment and lowest in the W0.26 experiment. By contrast, in the upper troposphere, DSE is highest in the W0.26 experiment and lowest in the

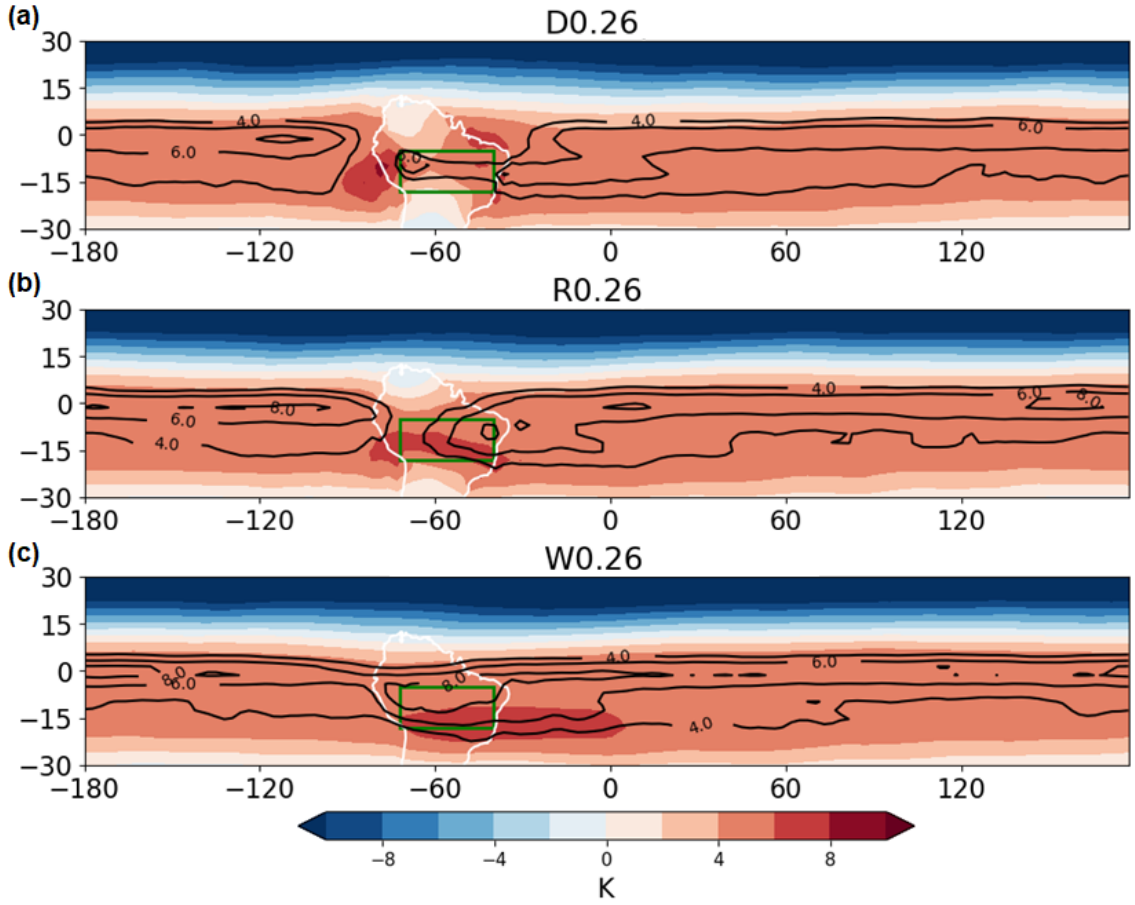



Figure 3.5: JFM distributions of the near-surface (973 hPa) MSE minus the tropical mean (30° S to N) value (shading) and precipitation in mm $d^{-1}$ (contours) in each of the three baseline experiments. The green box outlines the monsoon sector.

D0.26 experiment. As this part of the atmosphere is devoid of moisture (i.e. similar DSE and MSE), it means that the increased availability of land moisture leads to a warming of the upper troposphere. This is a manifestation of the relative standing in near-surface MSE across the experiments which impacts the upper troposphere through convection.

The vertical distribution of specific humidity ($q$) also varies in these experiments. D0.26 has a much drier boundary layer than R0.26 and W0.26. In all cases, relatively high near-surface moisture values fall off sharply with height at least partly owing to the missing convective detrainment, reducing tropospheric relative humidity values

(Fig. 3.4d,e). Consistent with these temperature and moisture distributions, the D0.26 experiment has arid near-surface conditions with 25% mean relative humidity (RH) compared to 60% and 70% RH in the R0.26 and W0.26 experiments, respectively (Fig. 3.4e), which are sufficiently close to the SBM convective threshold (70%). By contrast, it is far too dry for convective precipitation in D0.26. The precipitation intensity distributions also reflect this; in W0.26 the daily rainfall distribution is spread broadly over the 0 to 20 mm $d^{-1}$ range due to frequent moist convection (not shown). In D0.26 by contrast, the distribution has a long tail of infrequent extreme rain events (produced by large-scale scheme), while on the majority of days there is near-zero rainfall.

### 3.4.2 MSE Budget Analysis

The region-mean MSE budget analysis further illustrates the differing character of the monsoonal circulation in the experiments. The column-integrated MSE budget is given by:

$$\frac{\partial}{\partial t}\{\overline{\mathcal{E}}\} + \{\overline{\mathbf{v}} \cdot \nabla_p \overline{h}\} + \left\{\overline{\omega}\frac{\partial \overline{h}}{\partial p}\right\} + \nabla \cdot \{\overline{h'\mathbf{v}'}\} \approx \overline{F}_{net}, \tag{3.1}$$

wherein brackets denote mass-weighted column integrals, overbars are time means, primes are temporal deviations, $\mathcal{E}$ is the internal plus potential energy, $\mathbf{v}$ is the horizontal wind vector, $\nabla_p$ is the horizontal gradient operator on constant pressure surfaces, $\omega$ is vertical velocity in pressure coordinates, and $\overline{F}_{net}$ is the net column energy. $\overline{F}_{net}$ is the sum of top-of-atmosphere (TOA) and surface radiative fluxes into the column plus the surface turbulent fluxes.

Based on a calculation of the region mean column-integrated MSE budget (Table 3.1) following Hill et al. (2017), the vertical MSE advection is negative in the D0.26 experiment, denoting energy import by the circulation, and positive in the R0.26 and W0.26 experiments. In all three cases, the DSE component of the vertical MSE

advection term is positive, since DSE increases with altitude, while the moisture component is negative. Only in the D0.26 experiment does the latter dominate. Between 600 and 800 hPa the vertical moisture gradient, decreasing with altitude, is sampled by very strong vertical velocity values.

Table 3.1: JFM column-integrated MSE budget terms (W $m^{-2}$) averaged over the South American monsoon sector in the D0.26, R0.26, and W0.26 experiments.

| | D0.26 | R0.26 | W0.26 |
|---|---|---|---|
| $\overline{F}_{net}$ | 7.8 | 50.3 | 64.3 |
| $\frac{\partial}{\partial t}\{\overline{\mathcal{E}}\}$ | 3.5 | 3.6 | 3.1 |
| $\{\overline{\mathbf{v}} \cdot \nabla_p \overline{h}\}$ | 5.8 | 9.9 | 6.2 |
| $\left\{\overline{\omega}\frac{\partial \overline{h}}{\partial p}\right\}$ | -23.6 | 21.7 | 43.4 |
| $\nabla \cdot \{\overline{h'\mathbf{v}'}\}$ | 20.6 | 13.7 | 12.1 |

The negative $\left\{\overline{\omega}\frac{\partial \overline{h}}{\partial p}\right\}$ in D0.26 corresponds to a negative gross moist stability (GMS). The GMS relates the column energy transport to the strength of the mean circulation and can be thought of as the efficiency of a circulation's energy export (Bretherton et al., 2006). It is determined by the structure and amplitude of the vertical velocity, along with the stratification of the MSE. In this sense, the D0.26 monsoon circulation is similar in nature to the observed East Pacific ITCZ, a region of relatively shallow precipitating convection with a negative GMS (Back and Bretherton, 2006). By contrast, the monsoon dynamics in R0.26 and W0.26 resemble the deep convection of the West Pacific ITCZ, with positive vertical MSE advection values denoting energy export. These circulations comply with the Neelin and Held (1987) theory of tropical rainfall in which vertical MSE advection plays a chief role in balancing column heating, and precipitating tropical convection is associated with a positive GMS.

The horizontal MSE advection term is similar across the three experiments, between 5 and 10 W $m^{-2}$, and contributes to MSE export in each case. A decomposition of the horizontal MSE advection into dry and moist components, however, reflects differences between the experiments. In D0.26, the advection of relatively cool, moist air from the adjacent ocean produces a positive horizontal DSE advection ($\{\overline{\mathbf{v}} \cdot \nabla_p \overline{DSE}\}$ = 39.2 W $m^{-2}$) and a negative column horizontal moisture advection ($\{\overline{\mathbf{v}} \cdot \nabla_p \overline{L_v q}\}$ = -33.7 W $m^{-2}$). In the R0.26 and W0.26 configurations, the region mean horizontal DSE advection is near zero (2.4 and -0.1 W $m^{-2}$), while the horizontal moisture advection is positive, denoting export (7.8 and 6.4 W $m^{-2}$). These results indicate a relatively small land-sea temperature contrast and higher specific humidity over land than over ocean. $F_{net}$ differs by an order of magnitude between the experiments, ranging from 7.8 W $m^{-2}$ in D0.26 to 64 W $m^{-2}$ in W0.26. This is due primarily to differences in outgoing longwave radiation (OLR), with higher surface temperatures and thus OLR over dry land. The impact of the net column energy flux on the regional climate is examined further in the analysis of the albedo perturbation experiments.

The budget analysis demonstrates that in all three baseline experiments, precipitation is generated by the mean flow rather than transients. Mean ascent in the monsoon sector drives moisture convergence and precipitation, while transient eddies diverge moisture. The eddy MSE flux divergence is dominated by the moisture contribution in all three experiments, and the DSE component is negative in R0.26 and W0.26, indicating DSE convergence over the monsoon sector. The predominance of the mean circulation in generating precipitation is further supported by an assessment of the JFM mean potential vorticity (PV) distribution over continental longitudes (not shown). A necessary condition for baroclinic instability is a reversal of the meridional PV gradient (Charney and Stern, 1962; Hsieh and Cook, 2005), and this is not satisfied in D0.26 or W0.26. In R0.26, a PV gradient reversal at 600 hPa along the southern margin of the monsoon sector suggests a possible role for

baroclinic instability. Rayleigh's criterion for barotropic instability (a change in sign of $\beta - u_{yy}$) is not satisfied in any of the three baseline experiments (not shown).

### 3.4.3 Land albedo perturbation experiments

To better understand the impact of net column energy fluxes on monsoon characteristics, as well as the limits of monsoonal climate regimes, we examine a suite of land albedo perturbation experiments. Land albedo variations drastically impact the monsoonal precipitation magnitude (Fig. 3.6), in agreement with previous studies (Zhou and Xie, 2018; Boos and Storelvmo, 2016). With all three moisture conditions, JFM precipitation declines monotonically with increasing land albedo, with minimal rainfall at albedo values of 0.5 or higher. Regardless of local moisture availability, when the albedo is increased to 0.7 or 1.0, the monsoon region is subject to mean descent throughout the atmospheric column (Fig. 3.7).

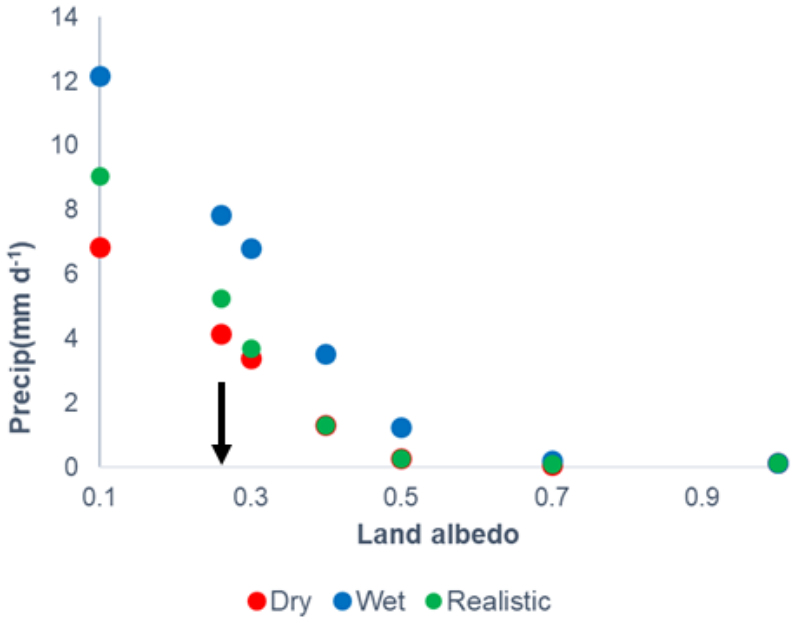



Figure 3.6: JFM mean precipitation in the monsoon sector as a function of land surface albedo with dry, wet, and realistic surface moisture conditions. The black arrow indicates the control albedo value of 0.26.

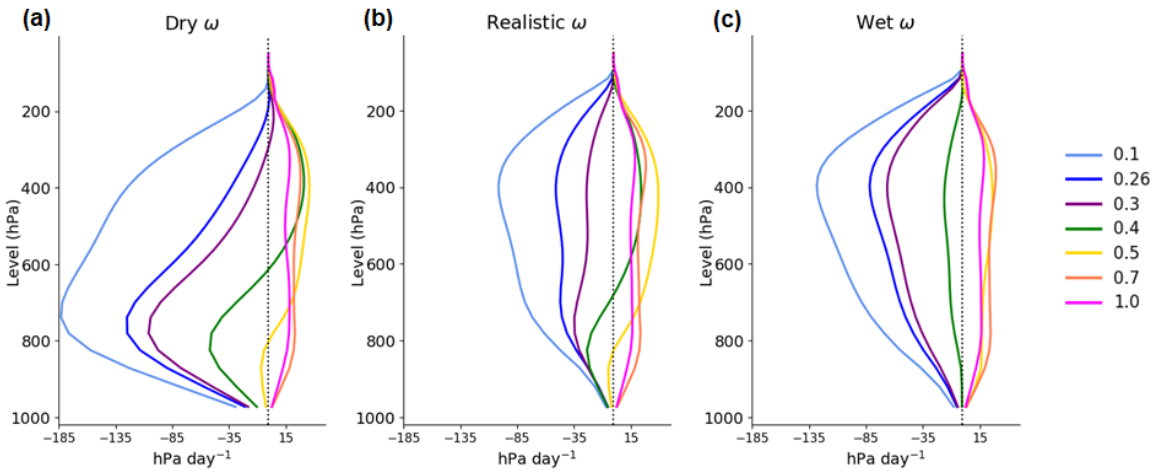



Figure 3.7: JFM mean vertical profiles of the vertical pressure velocity over the monsoon sector as land surface albedo is varied in the (a) dry, (b) realistic, and (c) wet land surface moisture experimental suites.

The surface temperatures over land in the R0.5 and D0.5 experiments (296 K and 301 K, respectively) remain higher than adjacent SSTs, so that a weak, viscously driven circulation persists, though it produces negligible precipitation (Fig.3.7a, b; Fig. 3.6). In the R and D experimental suites, ascent is confined to the boundary layer when albedo values are prescribed to 0.4 or 0.5 (Fig. 3.7a,b). In these simulations, the surface temperature distributions induce low-level pressure gradients which drive convergence over the monsoon sector. In the lower range of land albedo values, the R and D experiments diverge. In the D0.3, D0.26, and D0.1 experiments, the ascent grows increasingly vigorous and vertically extended. While the ascent maximum is relatively low in each of these experiments (below 650 hPa), the ascending motion extends through the mid-troposphere, and is accompanied by a jump in precipitation intensity with mean values of 3.4, 4.2, and 6.9 mm d$^{-1}$, respectively, compared to 1.3 mm d$^{-1}$ in the D0.4 experiment (Fig. 3.6). Even when land albedo is lowered to 0.1 in the dry land configuration, the precipitation derives almost exclusively from the large-scale scheme. By contrast, in the R0.3, R0.26, and R0.1 experiments, deep convection develops and precipitation increases to 3.7, 5.3, and 9.1 mm d$^{-1}$, respectively. The

shape of the ascent profiles and the proportion of convective to total precipitation support that convective instability underlies the monsoon development in these R experiments.

In the wet land configuration, land albedo variations do not alter the precipitation mode; in any experiment in which land remains thermodynamically favorable, precipitation is driven almost exclusively by convective instability. In W0.1 the vertical velocity profile strengthens, and when the land albedo is increased to 0.3 or 0.4, convection weakens but remains vertically extensive (Fig.3.7c). In the W0.5 experiment, without land-ocean gradients in surface moisture availability, the albedo perturbation reduces the temperature of land to 290 K, below that of the nearby sea surface, resulting in mean descent through the column (Fig. 3.7c). Boundary-layer confined ascent only develops in the simulations with land moisture limitations.

We consider the hypothesis that inertial instability underlies the enhancement of the monsoonal circulation in the three dry low-albedo experiments (i.e. D0.3, D0.26, and D0.1) (Plumb and Hou, 1992; Tomas and Webster, 1997). The near-surface (920 hPa) absolute vorticity ($\eta$) distribution supports this, as the zone of locally anticyclonic absolute vorticity expands with the off-equatorial migration of the $\eta = 0$ contour over continental latitudes when albedo is reduced below 0.4 (Fig. 3.8a, b). In inertially unstable zones, the divergent wind accelerates to generate a locally cyclonic tendency term, relaxing the instability. The resulting convergence zone intensifies local convection and precipitation. In the three low-albedo experiments, the near-surface divergence over the central continent is predominantly equatorward of $\eta = 0$, with the convergence zone largely lying poleward thereof, consistent with Tomas and Webster (1997) (Fig. 3.8a, b). This is not the case in the higher albedo experiments, including D0.4 and D0.5, in which the continental convergence zone straddles the $\eta = 0$ contour which hovers closer to the equator (Fig. 3.8c, d). Furthermore, the highest 920 hPa divergent wind speeds are bisected by the $\eta = 0$ contour when

it deviates poleward over the continent in the D0.3, D0.26, and D0.1 experiments (Fig. 3.15). In D0.4 and D0.5, the maximum divergent wind speeds over continental longitudes occur north of the equator (Fig. 3.15).

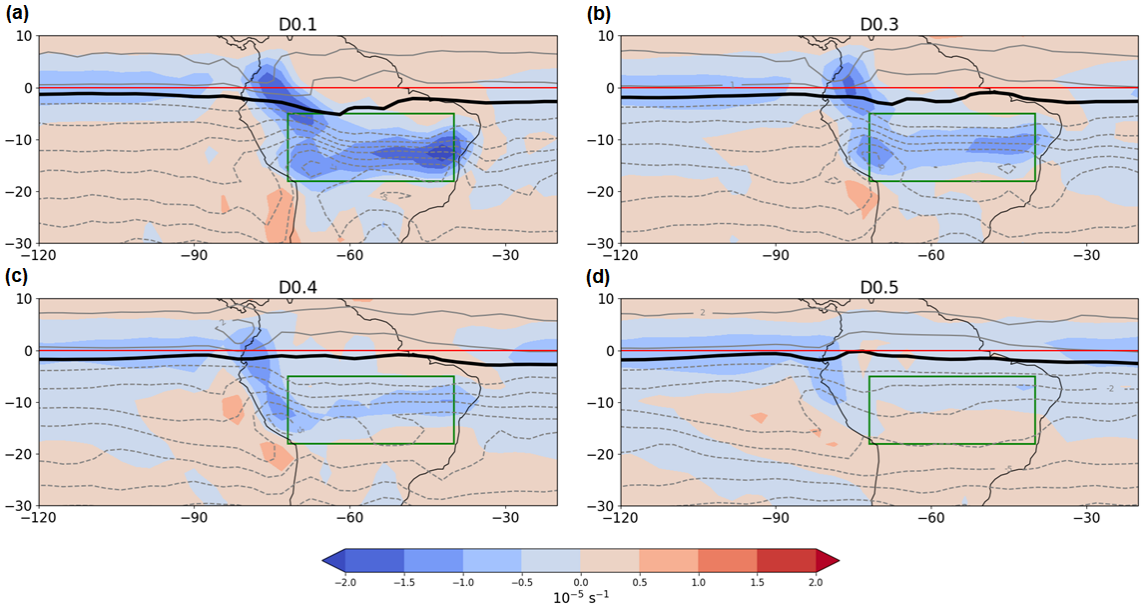



Figure 3.8: February 920 hPa absolute vorticity (contours) and divergence (shading) in the (a) D0.1, (b) D0.3, (c) D0.4, and (d) D0.5 simulations. The bold black line is the zero-line of absolute vorticity. The green box outlines the monsoon sector.

In the R and W experimental suites, inertial instability seems to play a less central role in monsoon development. In February, the $\eta = 0$ contour migrates only slightly further poleward over the continent than over the adjacent ocean, and the displacement is smaller than in the dry land experiments (not shown). For example, in D0.26, the maximum southward displacement of the contour over the continent is 4.2°, compared to 2.4° in the R0.26 experiment and 2.7° in W0.26. This disparity may be explained by the relatively strong cross-equatorial pressure gradient in the dry land experiments caused by the particularly strong heating of the continent.

In terms of the spatial distribution of precipitation, the effect of albedo variations depends on the land moisture configurations (Figs. 3.12-3.14). In the D configuration, the near-surface MSE maximum does not shift substantially in response to

albedo perturbations. Correspondingly, there is little latitudinal change in the monsoon location. At lower albedo values in the W configuration, and to a lesser extent in R, the near-surface MSE maximum increases and shifts poleward, and the monsoon expands poleward, in accordance with CQE predictions (Hurley and Boos, 2013). In both the R and W experiments, JFM precipitation is strongest near the Atlantic coast, and as the continent heats up at lower albedo values, the monsoon penetrates further westward over the continent. Increased continental heating and thermal gradients can enhance baroclinicity of prevailing easterlies and thus convective storm formation, driving a westward expansion of the monsoon; such a process underlies the strengthening of African Easterly Wave activity in global warming simulations (Skinner and Diffenbaugh, 2014). The spatial pattern of precipitation differs in the D suite; a local precipitation maximum near the west coast, coinciding with a local MSE maximum, emerges when the land albedo is 0.3 or lower (Fig. 3.5). The thermal low over the continent induces convergence of westerly winds from the Pacific and easterly winds from the Atlantic. These lower-tropospheric winds are stronger in the D suite than the corresponding R and W experiments due to the relatively strong land-sea thermal contrast (Fig. 3.3). With realistic topography, this moist westerly inflow would be impeded by the Andes.

When land surface albedo is varied across a broad range, various types of monsoonal circulations arise. At the highest albedo values, the land surface is cooler than the zonal mean value and the monsoon vanishes. At moderate albedo values, a viscously driven circulation emerges in local summer, producing a modest seasonal cycle of precipitation over off-equatorial South America. When albedo is reduced to 0.4 or below, inertial instability triggers enhanced convergence and precipitation in the dry land experiments, while convective instability produces more substantial rainfall in the realistic and wet land configurations. Even when the land albedo is suppressed to 0.1, the absence of latent heat fluxes leads to an exceedingly dry boundary layer

and inhibits parameterized moist convection in the dry land experiment. It is notable that even without triggering parameterized convection, the JFM precipitation in D0.1 is substantial (6.9 mm $d^{-1}$) and exceeded only by the W0.26, W0.1, and R0.1 experiments (7.8, 12.2, 9.1 mm $d^{-1}$, respectively). When $F_{net}$ is sufficiently strong due to the sensible heat flux, moisture transport and convergence partially compensate for the disabling of local moisture recycling. Evidently, while a local moisture limitation shapes the monsoonal regime, this parameter alone does not impede the monsoon's emergence nor its intensification. This has implications for monsoon onset, which occurs when local moisture availability is constrained following the dry season in South America. Throughout the spring, increasing local soil moisture and latent heat fluxes enable the vigorous convection of the monsoon season (Fu and Li, 2004). The processes driving the initial precipitation that primes the region for monsoon development may resemble the mechanisms in the D suite (i.e. inertial instability).

Regardless of the physics underlying precipitation development across the suite of experiments, the JFM precipitation increases nearly linearly with $F_{net}$, suggesting that this is a key parameter modulating monsoon intensity (Fig. 3.9a). Moderate precipitation develops only when $F_{net}$ values exceed zero. While local moisture conditions circumscribe the physical triggers of convection, in any case the magnitude of the precipitation is related to the magnitude of the MSE flux divergence. The circulation must comply with the MSE budget, meaning the MSE flux divergence by the total circulation (horizontal advection, vertical advection and eddies) must balance the net forcing and the time tendency (the latter changes negligibly). A higher net column forcing necessitates a stronger mean circulation and/or more pronounced MSE gradients on which the circulation acts. In the dry land experimental suite, the circulation strength (using vertical pressure velocity as a proxy) increases drastically as albedo is reduced, supporting more moisture import and stronger convergence (Fig. 3.7a). In the experiments with higher land moisture availability, the

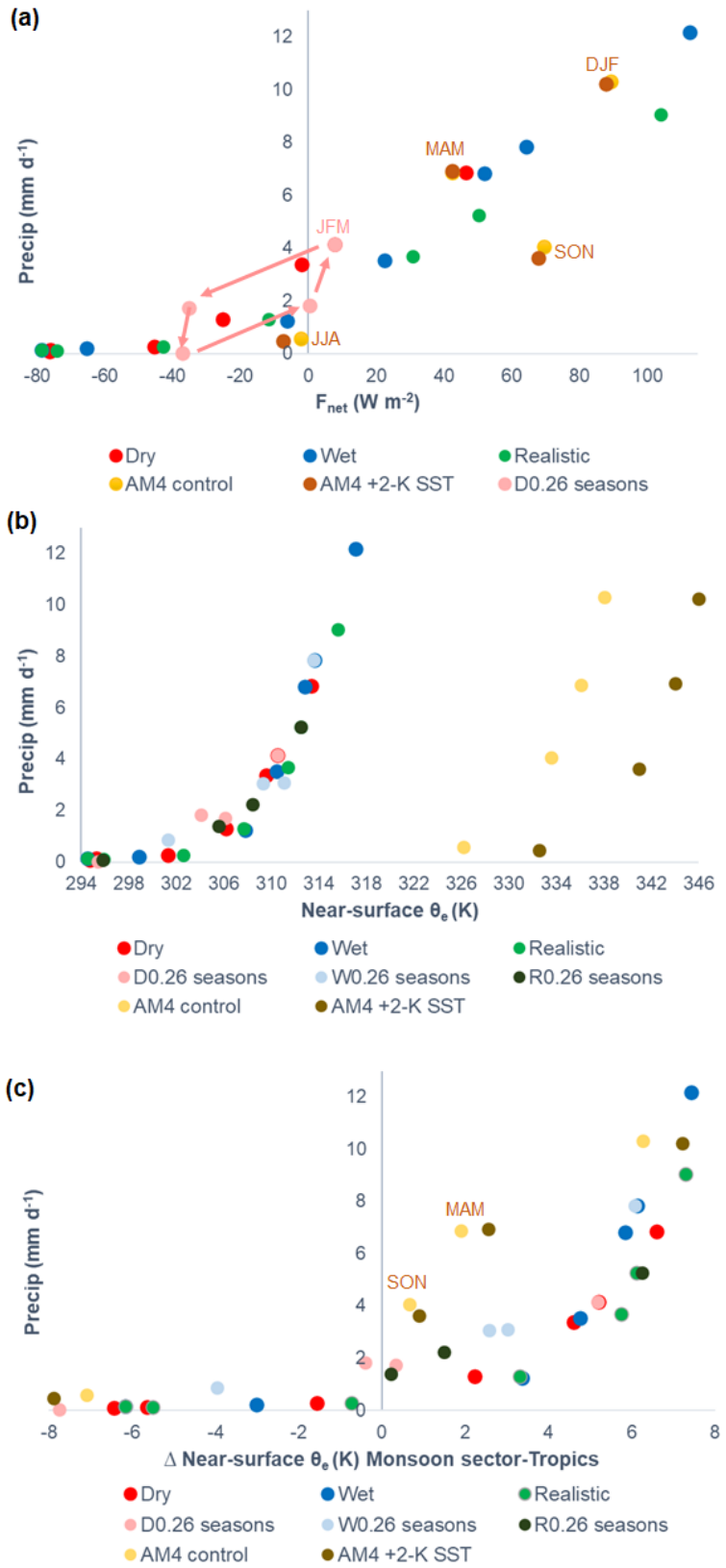



Figure 3.9: JFM mean precipitation in the monsoon sector as a function of (a) net column energy and (b) 973 hPa $\theta_e$ in all land surface albedo and moisture perturbation experiments. Panel (a) also includes the data for all four seasons of the GFDL AM4 control and +2-K SST warming experiments (labeled on the plot), as well as the four seasons of the D0.26 experiment (JFM, AMJ, JAS, OND). Panel (b) includes the seasonal data for the three baseline experiments.

circulation strength also increases with the net column forcing, albeit more modestly. In each suite of experiments, there is a concomitant enhancement of precipitation. This relationship between precipitation and net column forcing aligns with the findings of Boos and Storelvmo (2016), who demonstrate that monsoon strength has a nearly linear dependence on radiative forcing in both a comprehensive GCM and an analytical model.

Examining the TOA components of the net forcing term, the relationship between precipitation and net shortwave radiation is more consistent among experiments than the relationship between precipitation and OLR (not shown). As described earlier, the OLR is consistently higher in the dry land experiments due to the restrictions imposed on the land surface energy budget. By the same reasoning, the region-mean OLR at a given precipitation rate is consistently lower in the wet land experiments than the R experiments.

To better compare thermodynamic conditions given these moisture-modulated differences in the surface energy budget, we examine the relationship between near-surface $\theta_e$ and precipitation. In all three configurations, as albedo decreases, precipitation increases accompany increases in both the continental near-surface $\theta_e$ and its horizontal gradient (Fig. 3.9b, c). This underscores that a positive relationship between the amplitude of precipitation and near-surface $\theta_e$ can persist even when parameterized convection is largely inactive (Fig. 3.9b). Figure 3.9b illustrates a threshold behavior: all experiments with region-mean $\theta_e$ below 302 K have negligible precipitation. In the remaining experiments, in which region-mean $\theta_e$ values range from 306 K to 313 K, precipitation steadily increases with $\theta_e$ regardless of the land moisture condition. Fig (3.9c) is relevant for understanding this threshold behavior: the onset of appreciable monsoonal precipitation occurs when the monsoon sector region-mean near-surface MSE approaches or exceeds the tropical mean value. It is striking that this relationship holds in the dry land experiments, given the impedance

of parameterized convection, the shallow ascent profile (Fig. 3.4a), and the disruption of CQE conditions in the atmosphere (Fig. 3.11), as in Zhou and Xie (2018).

## 3.5 Discussion

The suite of idealized model experiments demonstrates the profound impact of land surface conditions on monsoon dynamics. These experiments, and the precipitation mechanisms they reveal, may inform our understanding of the stages of monsoon development on Earth. As an example, we consider the seasonal cycle over the South American monsoon sector as simulated in the GFDL AM4 model with prescribed climatological SSTs. In previous work, the authors examined the seasonally varying responses of precipitation in the South American monsoon sector to uniform 2-K SST warming in the GFDL AM4 model (Chapter 2, Smyth and Ming, 2020). Though the spring and fall are both characterized by moderate precipitation rates and similar region-mean MSE budget regimes in AM4, they exhibit different responses to warming. Spring rainfall decreases by 11% and $P - E$ decreases by 40%, while fall rainfall remains unchanged. This difference is linked to the difference in the climatological low-level relative humidity, which is 60% in spring and 80% in fall. The seasonal contrast in RH impacts the surface temperature and boundary layer MSE distributions and leads to different anomalous patterns in the SST warming experiment. Ultimately, the more pronounced land-sea contrast in spring renders the season vulnerable to drying by anomalous horizontal MSE advection in the +2-K experiment. The study concludes that differing boundary layer humidity plays a crucial role in setting the monsoon properties and thus the sensitivity to perturbations. This echoes Byrne and O'Gorman (2015), who find that changes in the horizontal gradients of temperature and fractional changes in relative humidity explain why the $P - E$ re-

sponse over land deviates from the canonical wet-get-wetter scaling. To what extent can the idealized model results shed light on these findings?

To assess whether the linear relationship between net column heating and precipitation holds beyond the idealized modeling framework, Figure 3.9a includes the data points for the four seasons in AM4 control and +2-K experiments. The seasonal cycle in AM4 exhibits hysteresis in this parameter space (Fig. 3.9a). In SON, preceding the rainy season, the AM4 control net column heating is 69.5 W $m^{-2}$ and the precipitation rate is 4.1 mm $d^{-1}$. Following the rainy season, in MAM, the net column heating is lower (42.5 W $m^{-2}$) while the precipitation rate is higher (6.9 mm $d^{-1}$). As noted above, the shoulder seasons have similar MSE budget regulation regimes, as characterized by the relative strength of vertical to horizontal MSE advection (Smyth and Ming, 2020). Mapping the seasonal cycle in Figure 3.9a points to the impact of the differing surface moisture availability on the efficiency of precipitation production. SON exhibits a clear deviation from the largely linear relationship across the idealized experiments and the other AM4 seasons (Fig. 3.9a). Based on net column heating, AM4 SON is most similar to W0.26 ($F_{net}$ = 64.3 W $m^{-2}$), but the W0.26 rainfall is nearly twice as strong (7.84 mm $d^{-1}$). When land surface moisture is limited, substantial moisture convergence from the ocean is needed to produce rainfall. In SON, the land heating is less pronounced than in the D suite and the circulation is substantially weaker, while the dry soil remains a limiting factor in generating precipitation.

The idealized experiments also exhibit seasonal hysteresis in the relationship between $F_{net}$ and precipitation, despite the fact that land surface moisture is externally controlled in D0.26 and W0.26. The seasonal cycle for D0.26 resembles that in AM4, though with reduced seasonal variability along both axes (Fig. 3.9a). This implies that the asymmetry between monsoon onset and withdrawal is due to the nature of the circulation, and is not entirely a consequence of seasonally varying land sur-

face moisture availability or cloud radiative effects. Though $F_{net}$ decreases strongly from summer to fall, even dropping below zero in D0.26, the circulation persists and continues to support relatively high precipitation rates. Monsoon withdrawal follows an equatorward and off-continental shift of near-surface MSE and temperature maxima (not shown). Figure 3.9b includes data for all four seasons of the D0.26, R0.26, and W0.26 experiments, and demonstrates a consistent relationship between near-surface $\theta_e$ and precipitation throughout the seasonal cycle. The near-surface MSE is consistently higher in the comprehensive GCM AM4, but the direct relationship between near-surface MSE and precipitation intensity holds throughout the seasonal cycle (Fig. 3.9b). While the net column heating varies directly with the strength of the summer monsoonal circulation, the near-surface $\theta_e$ is a better guide for capturing the monsoon-sector precipitation variability across seasons in both the idealized and comprehensive models. The near-surface $\theta_e$ contrast between the monsoon sector and the tropical mean also regulates the intensity of monsoon-sector precipitation throughout the seasonal cycle in the idealized experiments (Fig. 3.9c). As for the JFM data, substantial precipitation only occurs as the monsoon sector thermodynamic state approaches the tropical mean value. The strong relationships between precipitation and $\theta_e$ or contrasts thereof hold even in the dry land suite, when CQE conditions are not strictly satisfied. In AM4, the spring and fall deviate from the idealized model results, while the summer and winter values are remarkably consistent with the idealized model results (Fig. 3.9c).

The discrepancy between the monsoon onset season in AM4 (SON) and the idealized experiments is likely linked to the absence of one or more key processes from the idealized configuration. Connections between the idealized model simulations and AM4, or reality, must be drawn cautiously given the drastic simplification of the climate in the idealized experiments. The absence of global continental geometry impacts the general circulation in the idealized experiments, and much of the physics

is greatly simplified. In particular, the effects of clouds on surface temperature, radiative fluxes (and thus $F_{net}$), and precipitation generation are noteworthy. Clouds might, for example, reduce surface temperatures over land and impede circulation strength in AM4 SON as compared to the idealized simulations with limited land moisture (eg. Sharma et al., 1998).

The conclusions are largely robust to variations in the convective relaxation timescale, except that the ratio of large-scale to convective rainfall depends strongly on this parameter. In the R0.26 $\tau_{BM}$ experiments, the percentage of precipitation deriving from the SBM scheme is 88% in the control ($\tau_{BM}$ = 2 h), 81% with $\tau_{BM}$ = 4 h, 71% with $\tau_{BM}$ = 8 h, and only 36% when $\tau_{BM}$ = 16 h. As expected, the near-surface relative humidity increases with the relaxation time, since the moisture profiles are less frequently relaxed via the convection scheme. The climate is otherwise robust to $\tau_{BM}$, which has no notable impact on the total precipitation, nor on the region-mean surface temperature, OLR, net column energy flux, or moisture convergence ($P - E$).

Figure 3.10 provides a schematic overview of the monsoonal properties and relevant mechanisms as land surface conditions are varied. At the highest land albedo values, a monsoon cannot develop regardless of the land moisture condition, resulting in mean descent. Over dry land at mid-range land albedo values, a very shallow thermally driven monsoon develops. As land albedo decreases further, increasing the net column forcing and the cross-equatorial near-surface pressure gradient, inertial instability develops and leads to a deeper overturning cell. Deep convection can only develop when the land moisture constraint is relaxed, allowing latent heat fluxes to trigger convective instability. It is worthwhile to note that the shallow, thermally driven circulations resemble the regime described by Lindzen and Nigam (1987) in which boundary layer momentum dynamics play a crucial role. This view is supported by a set of perturbation experiments in which the land surface momentum

roughness length is varied from $5 \times 10^{-5}$ to 0.5 meters (its default value is $5 \times 10^{-3}$). When land surface roughness is increased by four orders of magnitude, precipitation increases strongly in D0.26 (+38%), slightly less so in R0.26 (+32%), and negligibly in W0.26 (+3.7%).

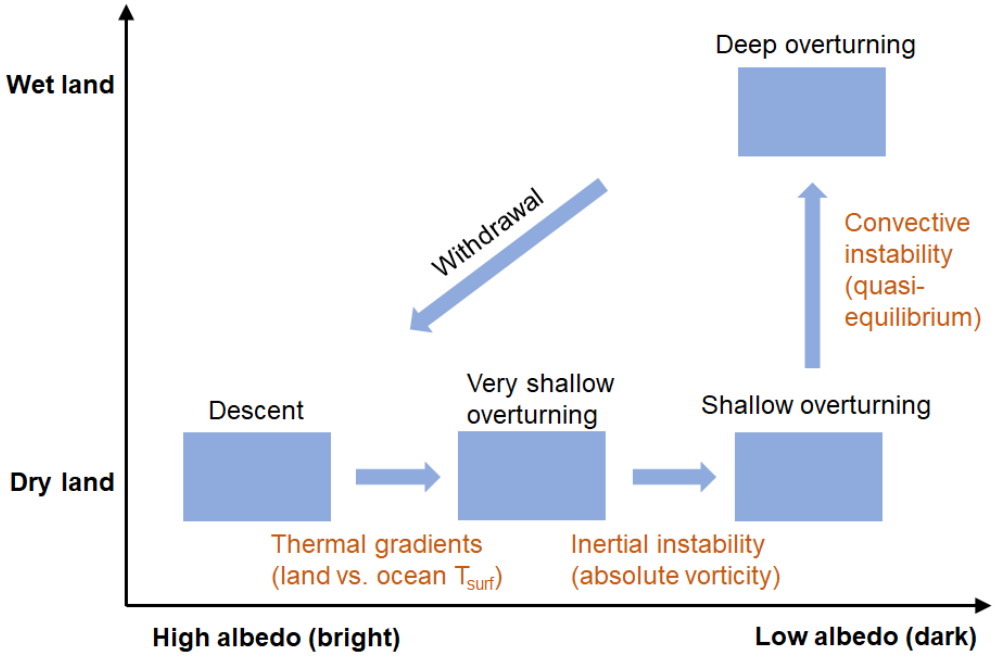



Figure 3.10: A schematic overview of the monsoon circulation properties and relevant physical mechanisms across the land surface parameter space.

The mechanisms at play in the idealized model simulations as land properties are modified may be relevant for the seasonal development of monsoons on Earth. Inertial instability alone is sufficient for producing a shallow but vigorous circulation and converging a large amount of moisture from the ocean. This mechanism may be key to monsoon onset following the dry season when soil moisture is low. Once the land is sufficiently moist, convective instability takes hold; the shallow circulation turns into a deep one. This mechanistic sequence is consistent with previous arguments (e.g. Fu et al., 1999) that wet season South American precipitation develops only after sufficient low-level moisture convergence reduces the convective inhibition.

In addition to elucidating the seasonal evolution of monsoon circulations, the idealized experiments indicate bounds on the range of land surface conditions that might support a monsoonal climate. When the net forcing is negative or the near-surface MSE is below the tropical mean value, a monsoon does not develop. It will be interesting to evaluate such threshold behavior in more realistic modeling settings. This can illuminate historical changes in tropical hydroclimate and provides a basis for understanding the how rising carbon dioxide levels may impact monsoons via their effect on land surface conditions.

## 3.6 Supplemental Material

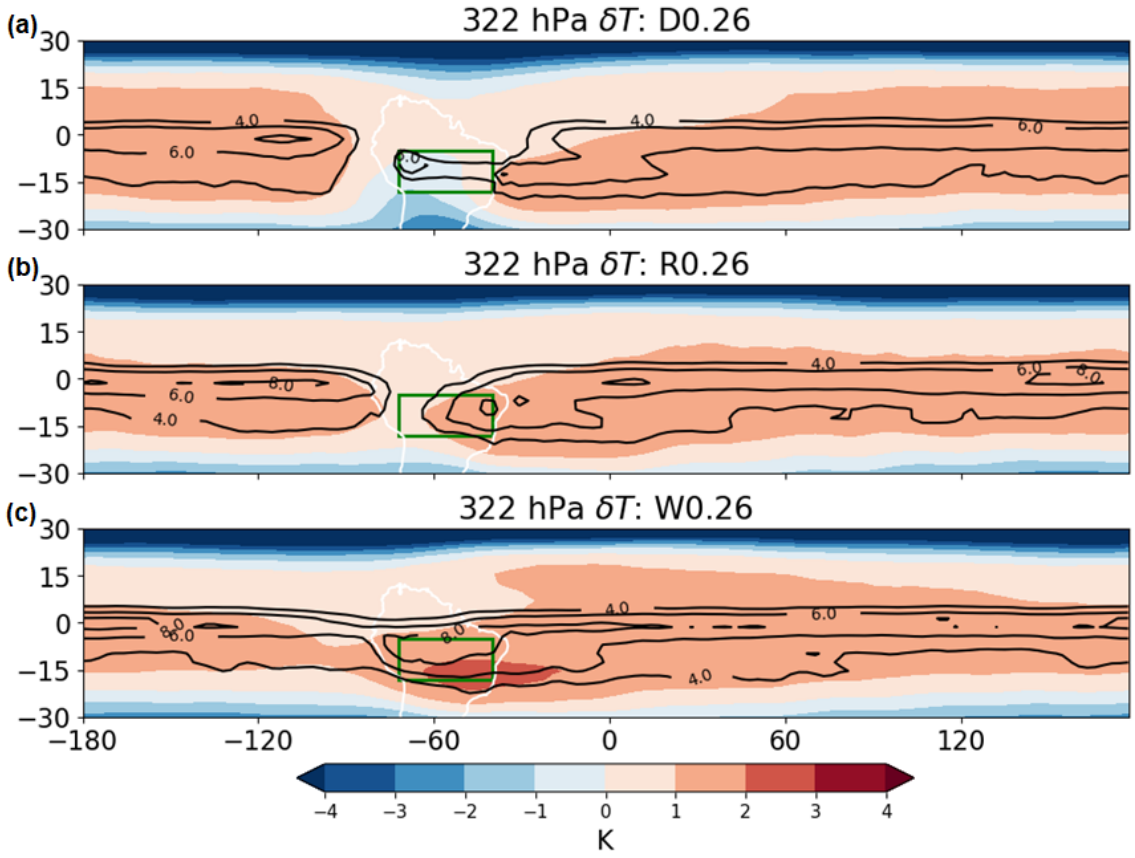



Figure 3.11: JFM distributions of free-tropospheric (322 hPa) temperature minus the tropical mean (30° S to N) value (shading) and precipitation in mm $d^{-1}$ (contours) in each of the three baseline experiments. The green box outlines the monsoon sector.

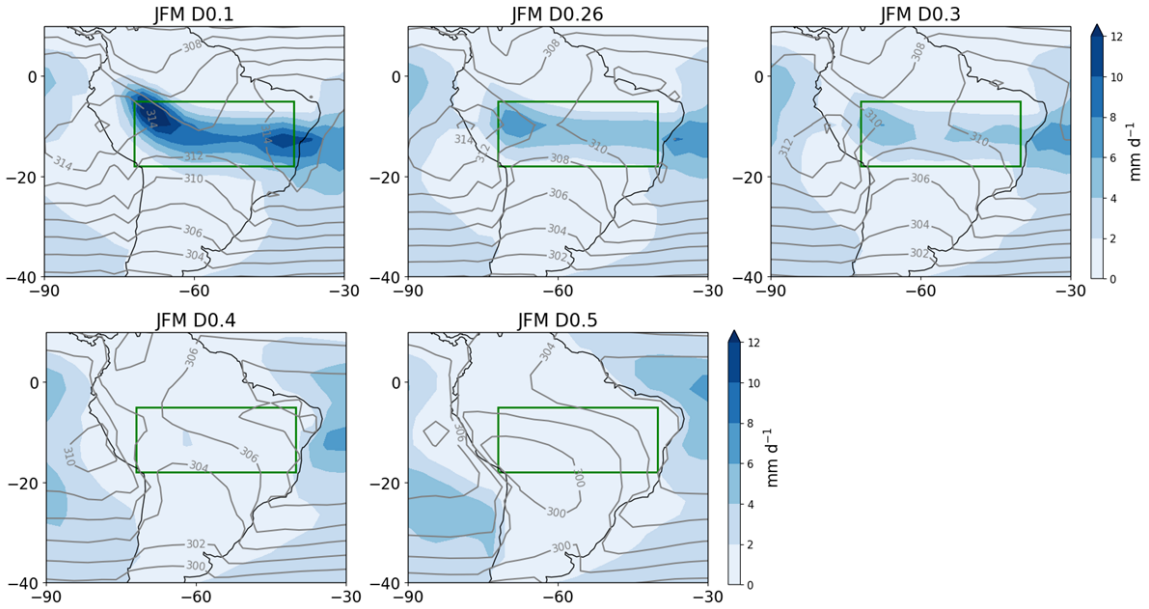



Figure 3.12: The JFM spatial distribution of precipitation (shading) and MSE (contours) in the D0.1- D0.5 albedo perturbation experiments. The green box outlines the monsoon sector.

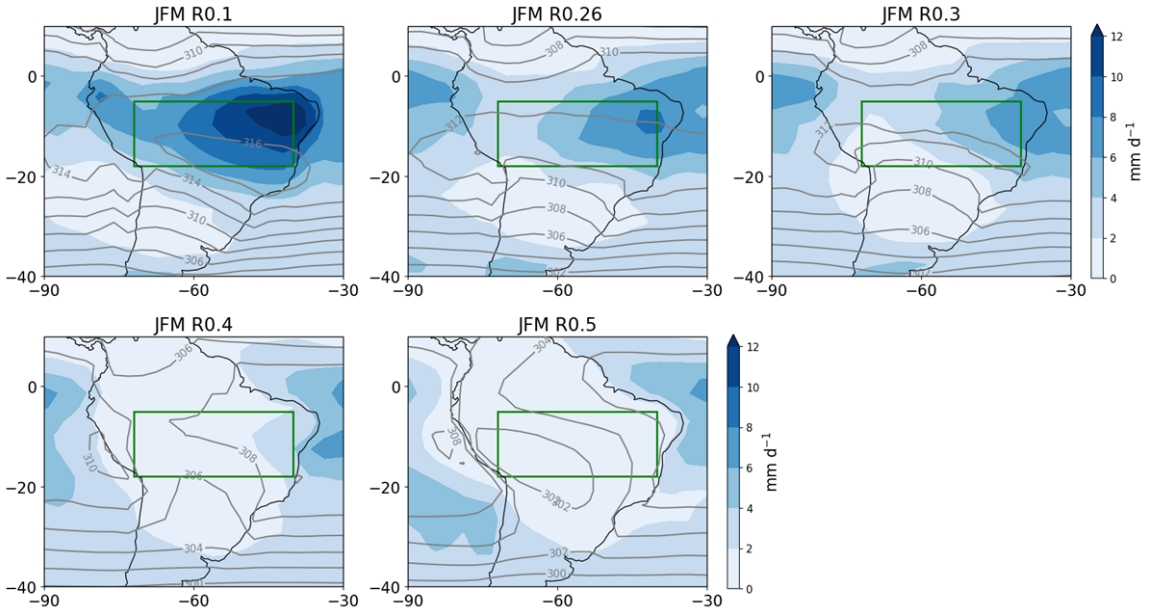



Figure 3.13: Same as Fig. 3.12, but for R0.1- R0.5.

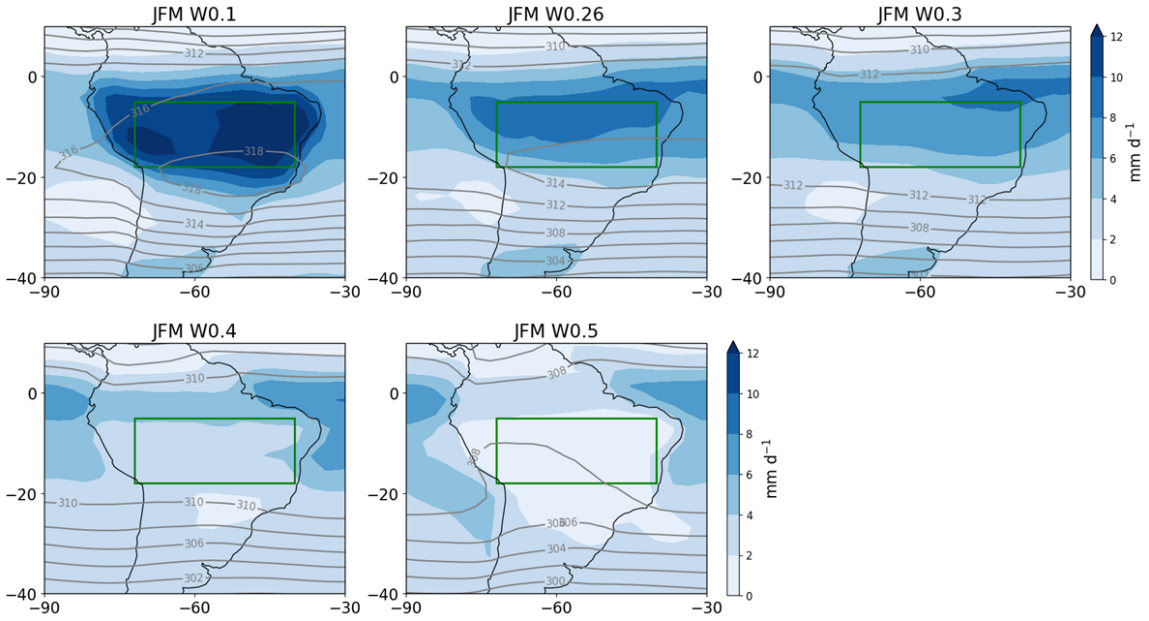



Figure 3.14: Same as Fig. 3.12, but for W0.1- W0.5.

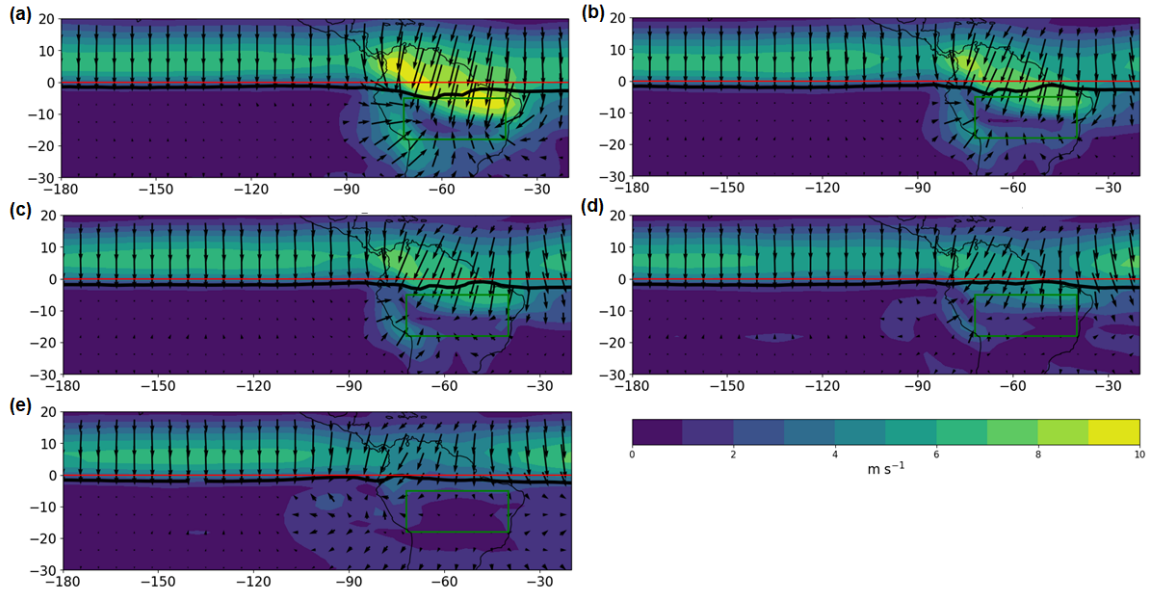



Figure 3.15: February near-surface (921 hPa) divergent winds (vectors) and divergent wind speed (shading) in (a) D0.1, (b) D0.26, (c) D0.3, (d) D0.4, and (e) D0.5.

# Chapter 4

# Synoptic analysis of monsoonal precipitation mechanisms over an idealized dry continent

## 4.1 Introduction

Thus far, this dissertation has focused on understanding the mean state of monsoonal circulations in idealized and comprehensive climate model experiments, as well as the climatological mean response to various perturbations. This chapter aims to build understanding of the mechanisms underlying precipitation generation by examining the synoptic rainfall variability during the monsoon season. The synoptic behavior of monsoon systems is poorly characterized, and has received little attention compared to the rich body of literature theorizing the controls of mean monsoon timing, position, and magnitude (e.g. Emanuel, 1995; Chou and Neelin, 2001; Privé and Plumb, 2007a,b; Bordoni and Schneider, 2008; Boos and Storelvmo, 2016; Shekar and Boos, 2016; Geen et al., 2018). This project is therefore exploratory, and conceived with an eye towards future research on monsoon low pressure systems. In this chapter, we

pursue the hypothesis put forth in Chapter 3 that inertial instability is instrumental in generating monsoonal precipitation over a dry continent.

Inertial instability is a horizontal instability that relates to the angular momentum distribution. A fluid between rotating cylinders is unstable if the angular momentum decreases radially outward (Rayleigh, 1917); for Earth, this translates to angular momentum decreasing towards the equator along an isentropic surface. For a purely zonal flow, the meridional derivative of the angular momentum can be related to the vertical component of the absolute vorticity $\eta$ like so:

$$\eta = \zeta + f = \frac{-1}{acos\phi}\frac{\partial M}{\partial \phi} \tag{4.1}$$

where $\zeta$ is the relative vorticity, $f$ is the Coriolis parameter, $a$ is Earth's radius, $\phi$ is latitude, and $M$ is the angular momentum per unit mass in the direction of the Earth's axis of rotation (Randall, 2012). According to Equation 4.1, in the Southern Hemisphere $M$ decreases towards the equator ($\frac{\partial M}{\partial \phi} < 0$) when the local absolute vorticity is positive. In other words, inertial instability can occur when the relative vorticity is anticyclonic and the absolute vorticity has the opposite sign of the planetary vorticity ($\eta f < 0$).

It is easier to reverse the sign of the absolute vorticity near the equator where the meridional shear can easily exceed the small Coriolis parameter. In addition, "wrong-signed" absolute vorticity can be advected across the equator. It seems plausible that inertial instability could therefore be an important driver of monsoonal precipitation over equatorial continents like South America and Africa. Assuming zonal flow in a geostrophically balanced basic state, the relevant equation governing a parcel's acceleration is

$$\frac{dv}{dt} = \frac{d^2(\delta y)}{dt^2} = -f(f - \frac{\partial u_g}{\partial y})\delta y \tag{4.2}$$

(Holton, 1992), where $v$ is the meridional wind, $\delta y$ is a meridional displacement, and $u_g$ is the geostrophic zonal wind. If a parcel is displaced poleward where $f - \frac{\partial u_g}{\partial y}$ has the opposite sign of $f$ (e.g. $f\eta < 0$, locally anticyclonic flow) , the parcel will accelerate in the direction of $\delta y$, producing divergent meridional flow. In the Southern Hemisphere ($f < 0$), a poleward perturbation $\delta y < 0$ will accelerate southward $\frac{dv}{dt} < 0$ when $f > \frac{\partial u_g}{\partial y}$. This is an inertially unstable zone, and it occurs when positive $\eta$ air crosses the equator into the Southern Hemisphere. Poleward of the $\eta = 0$ contour, the Coriolis force is stronger and the parcel experiences a net force that opposes the direction of the displacement. In this sector, the meridional divergent wind weakens, producing a convergence zone. Where the atmosphere is conditionally unstable, this convergence can produce convection and precipitation. The inertial instability mechanism can shed light on the initiation of convection, but not on the dynamics governing the propagation of precipitating disturbances. We elaborate on this subject in Section 4.2.2.

Inertial instability is related to symmetric instability, which is an instability to slantwise motions driven by locally anticyclonic potential vorticity (PV) anomalies in a conditionally stable atmosphere (Krishnakumar and Lau, 1998). Since inertial instability involves only the horizontal forces, it can be diagnosed at a single pressure level (Tomas and Webster, 1997). Symmetric instability is equivalent to inertial instability on an isentropic surface, where there is zero buoyancy force (Schultz and Schumacher, 1999). Near the equator, the potential temperature varies little on pressure surfaces, so symmetric instability reduces to inertial instability (Tomas and Webster, 1997).

A near equatorial continent, especially one with limited moisture, provides conditions for strong heating and thus a strong cross-equatorial meridional pressure gradient that could advect absolute vorticity across the equator and produce an inertially unstable environment. Tomas and Webster (1997) argue that the off-equatorial con-

vection in monsoon regions cannot be understand through thermodynamics alone. In these sectors, convection is not co-located with the SST maximum, and is strongest equatorward of the surface pressure minimum, indicating that the surface low is associated with the land-ocean heating contrast rather than the precipitation (Tomas and Webster, 1997). In addition, the convection in these zones tends to be stronger than near-equatorial convection. In an observational analysis they find that various signatures of inertial instability are present in these locations, and conclude that this dynamical mechanism plays a prominent role in driving off-equatorial convection in regions with strong cross-equatorial pressure gradients.

Thompson et al. (2017) develop a global climatology of inertial instability with ERA-Interim reanalysis data, and like Tomas and Webster (1997) conclude that lower-tropospheric inertial instability occurs frequently in the tropics. This holds whether one diagnoses instability with the "traditional" criterion described above ($f\eta < 0$), or the "gradient criterion" which assumes gradient-wind balance of the mean flow (see Thompson et al. (2017) equation 9). We therefore utilize the traditional criterion, which is simpler to assess.

Cook (2015) argues that inertial instability plays a key role in the abrupt transition of rainfall in the West African monsoon onset. In early summer, the West African precipitation maximum shifts from the Gulf of Guinea near 4°N to the Sahel at ∼12° N. The cessation of rainfall over the Gulf of Guinea coincides with the development of inertial instability in the region, based on 6-hourly ERA-Interim and OPERA-WAFR reanalysis. In the inertially unstable regime, northward perturbations induced by the large-scale pressure gradient accelerate poleward, producing low-level divergence and terminating precipitation over the Gulf of Guinea. The present investigation similarly evaluates the precipitation and atmospheric conditions on synoptic timescales to discern the role of inertial instability in establishing the continental precipitation distribution. Inertial instability over the Arabian Sea has also been implicated in

Indian monsoon onset (Wu and Liu, 2014), and Thompson et al. (2017) show further evidence that strong cross-equatorial flow by the Somali jet leads to frequent lower-tropospheric inertial instability in this sector. These studies demonstrate the importance of inertial instability in monsoon development on Earth, even for an off-equatorial continent.

Chapter 3 of this dissertation presents some evidence that inertial instability could be a key mechanism for generating precipitation over a completely dry equatorial continent (see Figs 3.8, 3.15 and discussion thereof). This was based on the 20-year climatological mean behavior in February of the D0.26 experiment with the idealized moist model (see Section 3.3 for simulation details). Here, we further explore that idea by analyzing daily precipitation events in a single month, January in year 18 of the simulation. We begin by comparing the synoptic behavior in D0.26 to the experiments with bucket hydrology (R0.26) or unlimited moisture over land (W0.26). Then we evaluate in detail a multi-day precipitation event in the D0.26 experiment. Next we discuss the possible relevance of theory on monsoon low pressure systems for understanding the simulated disturbances, before concluding with a summary and plans for ongoing research.

## 4.2 Results

The hypothesis that inertial instability initiates precipitation over a dry continent is based on the presence of a large-scale cross-equatorial pressure gradient at continental longitudes in local summer. The JFM D0.26 15-year mean near-surface temperature distribution illustrates the pronounced land-sea thermal contrast that develops when surface latent heat fluxes are disabled over land (Fig. 4.1a). Near-surface temperatures are over 9 K higher over the inner continent than the tropical mean value. This

supports the argument that the large-scale pressure gradient is a result of land-sea differential heating, and is a possible driver of continental precipitation.

The JFM climatological mean lower-tropospheric winds are northeasterly over the monsoon sector, advecting relatively moist oceanic air over the dry continent (Fig. 4.1b). The cross-equatorial flow is most pronounced over continental longitudes, in accordance with the large-scale thermal and pressure gradients. The upper-tropospheric winds are weaker and more easterly across the monsoon sector. The southerly cross-equatorial return flow is also evident across the tropics (Fig. 4.1c).

Next we consider the atmospheric behavior in one month of the D0.26 experiment: January of year 18. January is the first month of the peak monsoon season, during which the majority of annual precipitation falls in this sector. Strong storms, with precipitation exceeding 20 mm $d^{-1}$, sweep across continental longitudes from east to west, in the same direction as the climatological easterly flow (Fig. 4.2a). We focus on diagnosing inertial instability in the lower troposphere, where the resulting divergence-convergence dipole straddling the $\eta = 0$ contour could converge substantial moisture and produce precipitation. Therefore, Figures 4.2b and c show results at 921 hPa for the perturbation meridional velocity at 10° S, and the southernmost latitudinal position of the $\eta = 0$ contour. Similar patterns are apparent at 781 hPa (not shown), and we will consider the vertical structure of the absolute vorticity distribution in Section 4.2.1. Figure 4.2b shows the meridional velocity minus its monthly mean value. Anomalous northerly (pink) flow often coincides with heavy precipitation periods, such as on Day 6, when the precipitation centers on both coasts ($\sim$ 285 and 320°) coincide with anomalous northerly winds. This is consistent with enhanced cross-equatorial winds during periods of heightened inertial instability.

A key signature of inertial instability is the poleward displacement of the zero-line of absolute vorticity ($\eta = 0$), producing a near-equatorial zone in which $\eta f < 0$. Figure 4.2c shows the latitude where the $\eta = 0$ contour resides at each longitude; the

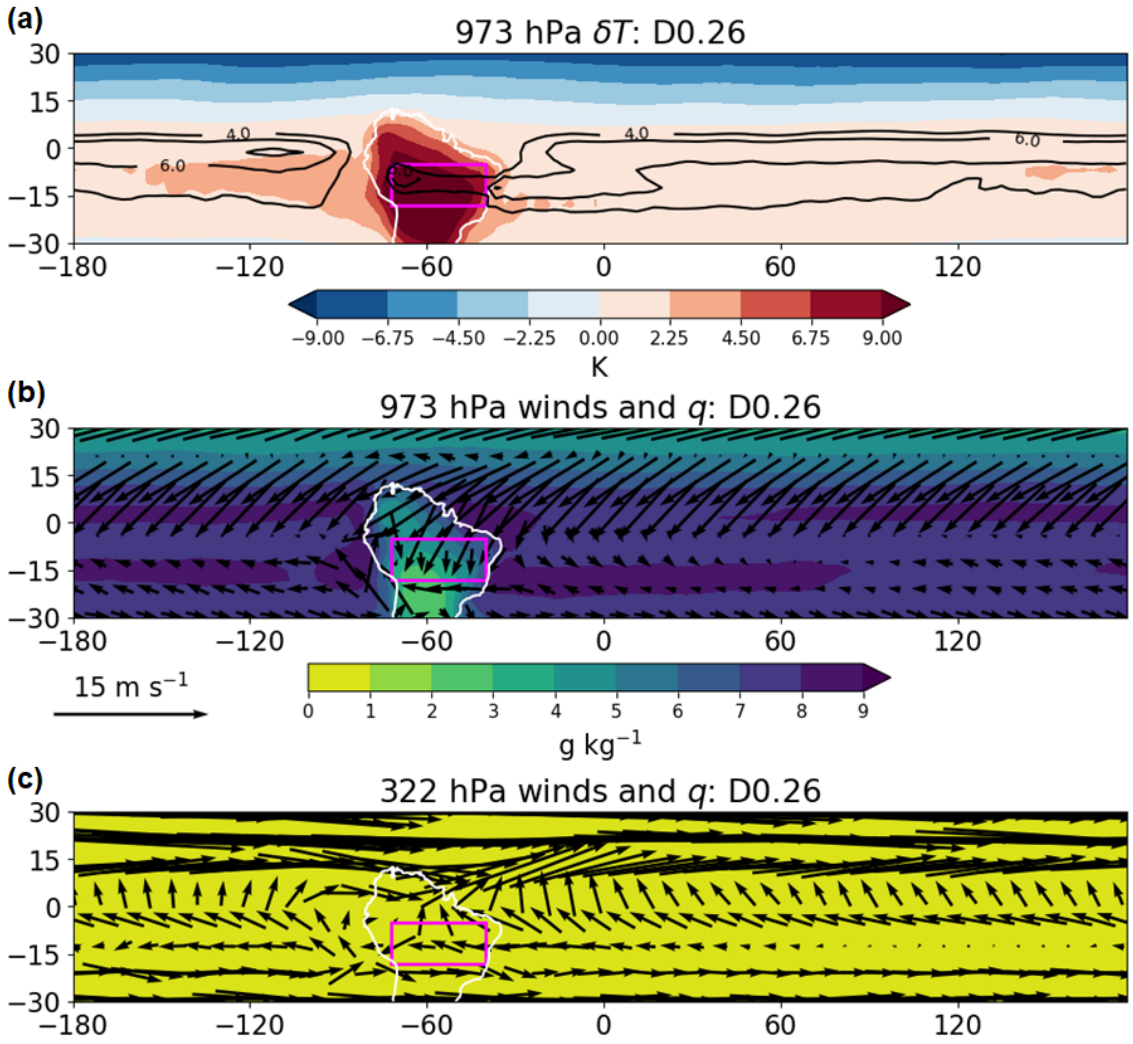



Figure 4.1: JFM 15-year mean distribution of the near-surface (973 hPa) temperature minus the tropical mean (30°S to N) value (shading) and precipitation in mm $d^{-1}$ (contours) in the D0.26 experiment (a). The JFM winds (vectors) and specific humidity (shading) at 973 hPa (b) and 322 hPa (c). The magenta box denotes the monsoon sector.

data is linearly interpolated to a 1° resolution in the meridional direction to more accurately estimate the zero-crossing latitude. Note that the longitudinal domain is broader than the other two Hovmoller plots, in order to show the clear difference in the $\eta = 0$ position over continental and oceanic longitudes. This complies with the hypothesis that the continental heating sets up the large-scale conditions conducive to this instability. The $\eta = 0$ contour is consistently located in the southern

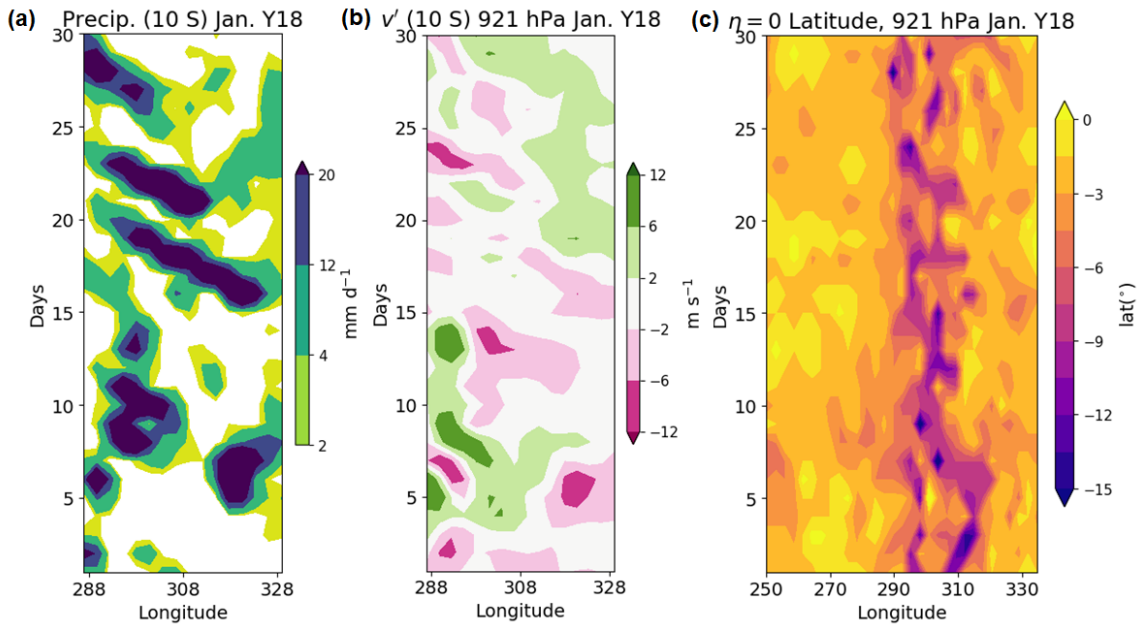



Figure 4.2: January Hovmoller diagrams of precipitation at 10° S (a), perturbation meridional velocity, computed as the anomaly from monthly mean values, at 10° S (b), and the southernmost latitudinal position of the $\eta = 0$ contour (c). Note that the longitudinal extent is broader in (c). Each plot uses daily mean model output.

hemisphere in January, sometimes poleward of 10° S over the continent. While the intrinsic timescale for inertial instability is $f^{-1}$, the cross-equatorial thermal gradient is continuous throughout the season, so the signatures of inertial instability are present on climatological timescales (shown in Chapter 3), as with other forced instabilities (Tomas and Webster, 1997). The southward excursions of the $\eta = 0$ contour sometimes appear to sweep westward across the continent, as in days 5-10; the zonal flow at 921 hPa is not always easterly, a point to which we return later.

One can compare the atmospheric behavior in D0.26 to R0.26 and W0.26, when the land moisture constraint is relaxed. Figures 4.3 and 4.4 show Hovmoller plots of precipitation, perturbation meridional velocity, and the latitude of the $\eta = 0$ contour in the R0.26 and W0.26 experiments. For these experiments, mean precipitation peaks in February (see Fig. 3.1a), so data for the month of February in Year 18 of the simulation is presented. In the R0.26 experiment, the continental hydrology is

represented with a bucket model, and in W0.26, the continental moisture is unlimited, such that the land-sea contrast is due only to the differing heat capacity (i.e. mixed layer depth). Both of these experiments exhibit westward propagating precipitation and meridional perturbation velocity, as in D0.26. The propagation speed of precipitation centers appears similar in R0.26 to D0.26, at approximately 10 m $s^{-1}$, while propagation is somewhat faster over wet land, at approximately 14 m $s^{-1}$. While the precipitating disturbances appear similar across the experiments, it is clear that the extent of the inertially unstable zone differs markedly between D0.26 and the other experiments. The 921 hPa $\eta = 0$ contour is much more confined to the equator when the continental moisture constraint is relaxed (Fig. 4.3c, 4.4c). The inertially unstable zone rarely extends beyond 6° S in R0.26 or W0.26, while it often expands to 10.5°S or more over a dry continent (Fig. 4.2c). This leads us to hypothesize that inertial instability plays a role in establishing the large-scale circulation and initializing convection in the D0.26 experiment, but that another mechanism drives the westward propagation of precipitating disturbances in all three experiments. We further discuss these disturbances, which resemble monsoon low pressure systems, in Section 4.2.2.

The D0.26 monsoon sector ($5 - 18$°S, $40 - 72$°W i.e. $288 - 320$° E) region-mean vertical pressure velocity profiles are displayed in Figure 4.5. The 30 daily-mean plots indicate that even when surface latent heat fluxes are disabled, convection is consistent over the dry continent, with ascending motion throughout January. This ascending motion varies in strength and vertical extent. To better discern the role of inertial instability in driving precipitation, we select a multi-day synoptic event to study in more detail. We investigate the Day 21-23 period, during which the atmosphere transitions from relatively shallow and weak ascent on Day 20 to more vigorous and penetrative convection on Days 22 and 23. Over the three-day event, strong rainfall at 10° S is evident in Figure 4.2a.

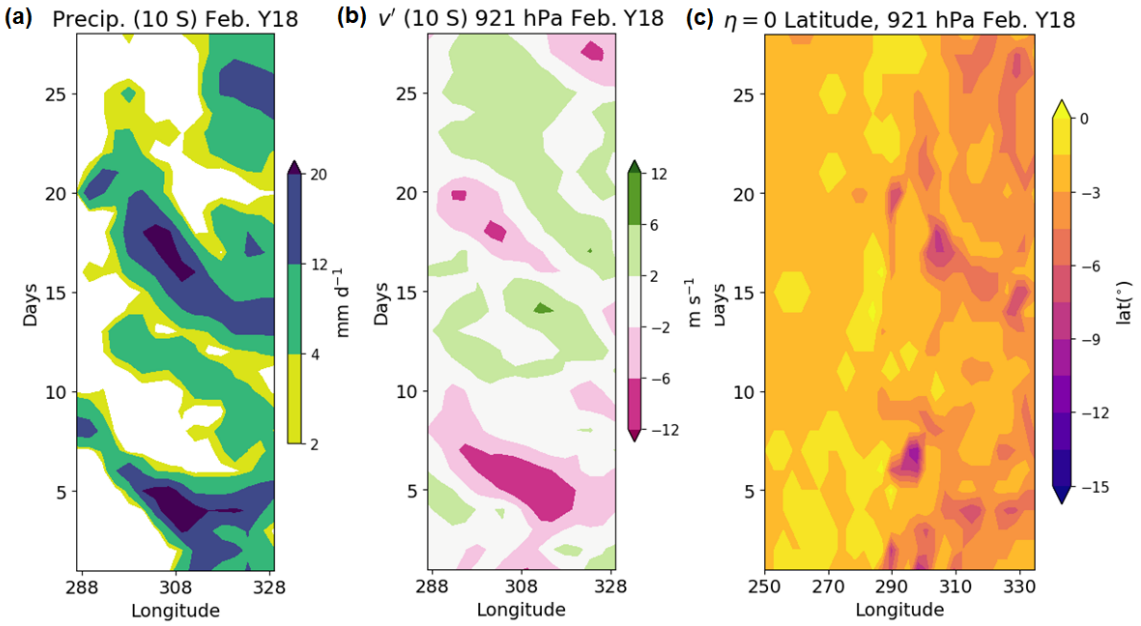



Figure 4.3: Hovmoller diagrams as in Fig. 4.2, but for R0.26 in February.

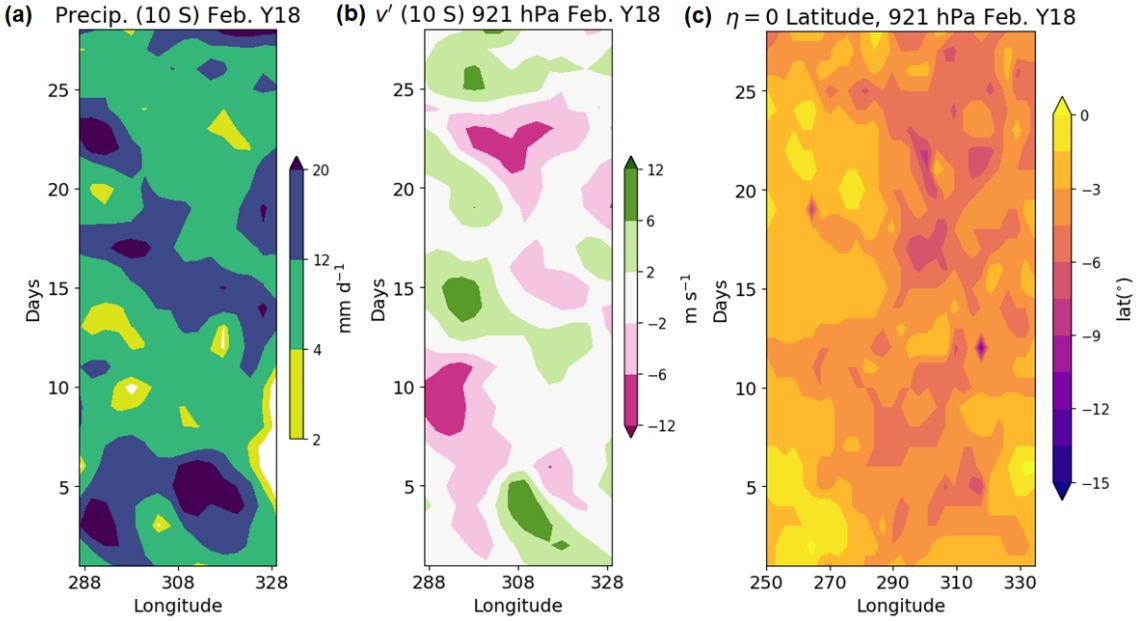



Figure 4.4: Hovmoller diagrams as in Fig. 4.2, but for W0.26 in February.

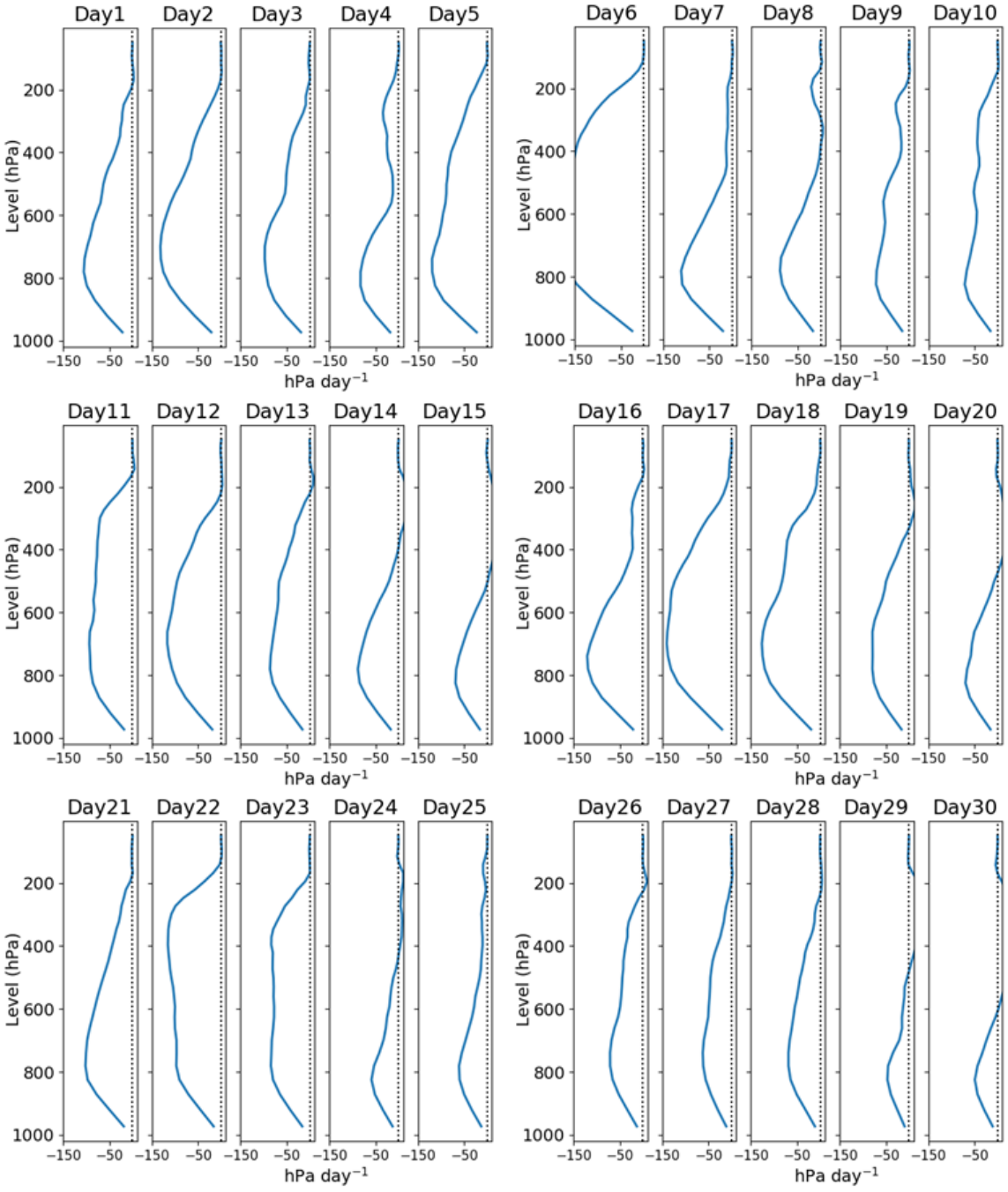



Figure 4.5: Daily mean profiles of the vertical pressure velocity $\omega$ averaged over the monsoon sector, in January year 18 of the D0.26 simulation.

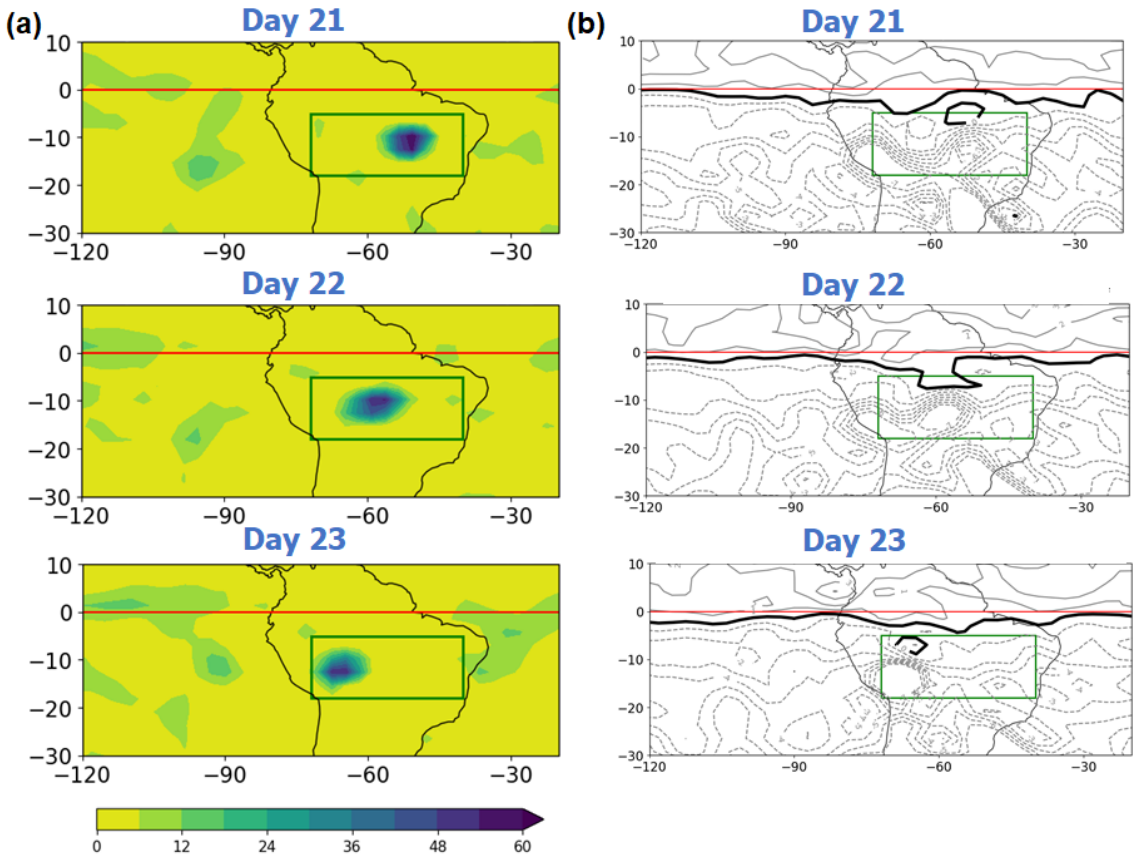



Figure 4.6: Daily mean precipitation in mm $d^{-1}$ on Days 21-23 of January (a). Absolute vorticity ($\eta$) in $10^{-5}$ $s^{-1}$ at 921 hPa, with dashed lines indicating negative values (b). The heavy bold contour shows $\eta = 0$, and the equator is marked by a red line.

### 4.2.1 Event Analysis: Days 21-23

On Days 21-23, a storm sweeps westward across the monsoon sector (Figure 4.6a). The heavy black line in Figure 4.6b shows the 921 hPa $\eta = 0$ contour, which exhibits clear displacement into the southern hemisphere by $> 5°$. As described in the Introduction 4.1, this leads to divergent meridional flow between the equator and the heavy black line, and anomalous convergence poleward thereof, consistent with the storm location on all three days. Day 22 exhibits the deepest mean convection over this period, and also has the most pronounced poleward excursion of the inertially unstable zone. A local minimum of absolute vorticity, indicating cyclonic flow, coincides with the precipitation center.

The near-surface wind distribution over the three day period is pictured in Figure 4.7. The cross-equatorial flow over the continent is stronger than the summer climatological mean (Fig. 3.3a, 4.1b). The poleward surface temperature gradient also leads to tropical westerly flow due to eastward diversion by the Coriolis force. The near-surface westerly flow is most apparent in the monsoon sector at $\sim 10°$ S on Days 21 and 22; the precipitation propagates westward at about 10 m $s^{-1}$ against the low-level flow. Next, we consider whether the anomalous meridional shear of the zonal wind over continental longitudes could be barotropically unstable. In other words, is the near-surface $\partial u/\partial y$ strong enough to reduce the meridional PV gradient, thus satisfying Rayleigh's criterion for barotropic instability? This would indicate that the modified flow induced by inertial instability may in turn be susceptible to barotropic instability, resulting in a secondary mechanism for precipitation generation over the continent. This interplay between inertial and barotropic modes has been highlighted in other theoretical studies of near-equatorial instability (e.g. Natarov and Richards, 2015). For example, Lieberman et al. (2021) explain a mechanism whereby inertial instability induces barotropically-unstable wind curvature in the stratospohere.

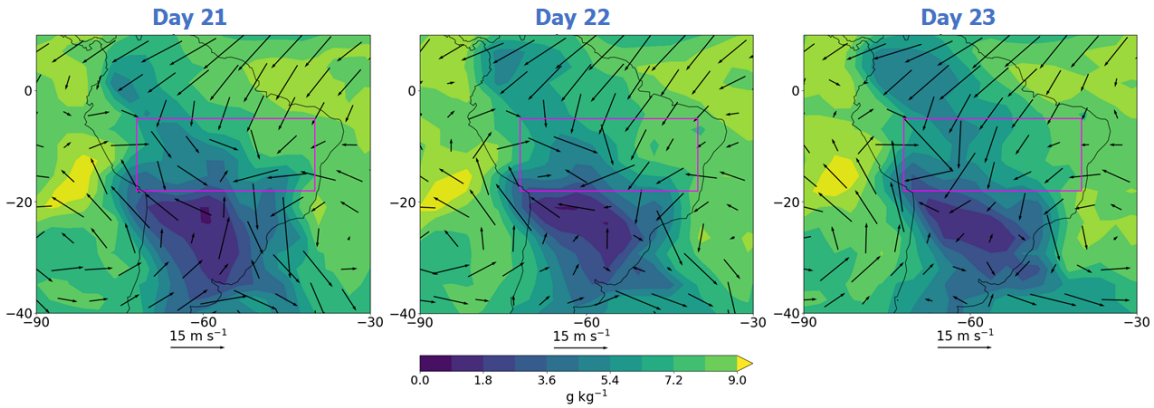



Figure 4.7: 921 hPa winds and specific humidity (g kg$^{-1}$) on Days 21-23. The monsoon sector is outlined in magenta.

To explore this possibility, we examine the the limited zonal-mean zonal wind $\overline{u}$ over continental longitudes $288 - 320°$ E, averaged over a pentad (Days 21-25) encompassing the precipitation event of interest (Fig. 4.8a). Easterly flow, in red, prevails through most of the tropical lower troposphere in this sector. However, there is westerly flow from the surface to a depth of $\sim$ 700 hPa over the continent between $\sim$ 7 and 13° S, as seen in Figure 4.7 at a single pressure level. Again, we note that the precipitation moves westward across these latitudes during this pentad, against the lower-tropospheric flow. Rayleigh's criterion for barotropic instability is a reversal of the meridional PV gradient due to horizontal shear; mathematically, this is marked by a change in the sign of $\beta - \overline{u}_{yy}$, where $\beta$ is the meridional gradient of the planetary vorticity and $\overline{u}_{yy}$ is the second derivative of the pentad-mean zonal wind. Rayleigh's criterion is indeed satisfied in the lower to mid-troposphere between 15 and 20° S over the continent (Fig. 4.8b). This indicates that the meridional shear associated with the monsoonal circulation is potentially unstable. This potential secondary instability is just poleward of the limited zonal-mean meridional overturning circulation (Fig. 4.8c). Further, the strongest ascent occurs poleward of the $\eta = 0$ contour, consistent with expectations for the location of the convergence zone induced by inertial instability (Tomas and Webster, 1997).

Based on this event and examination of other pentads in January, in the period of strong inertial instability, the resulting circulation flattens meridional shear and relaxes barotropic instability in the upper troposphere, but heightens meridional shear and reverses the potential vorticity gradient in the lower troposphere (not shown), near the poleward boundary of the meridional overturning circulation (Fig. 4.8b). It will be interesting to investigate whether barotropic eddies develop in this simulation to better understand the potential interplay between inertial and barotropic instability in generating precipitation over a dry equatorial continent.

Figure 4.8a also illustrates that there is strong vertical easterly shear around 10°S, consistent with a poleward increasing temperature gradient under thermal wind balance. Previous work has explored the idea that baroclinic instability in an easterly shear can produce monsoonal disturbances (e.g. Xie and Saiki, 1999). Clark et al. (2020) use the same idealized model as the present study, but with global continental geometry and a bucket hydrology model governing land evaporation, to study monsoonal lows in the South Asian monsoon sector. They find that Ertel potential vorticity anomalies associated with the low pressure systems tilt with the easterly shear, rather than against it, when viewed in the longitude-height plane. This would prevent amplification of counter-propagating Rossby waves, which indicates that baroclinic instability is not producing the disturbances; this is also the case in reanalysis data over the South Asian monsoon sector according to Cohen and Boos (2016). A similar investigation of whether baroclinic instability may contribute to the storm development in the present model configuration is left to future work.

As mentioned in the Introduction 4.1, the concept of inertial instability is closely related to that of symmetric instability. Symmetric instability, however, takes a three-dimensional view, and occurs when the potential vorticity, rather than the absolute vorticity, is locally anticyclonic. Krishnakumar and Lau (1998) investigate reanalysis datasets and conclude that symmetric instability of the zonal flow could underlie the

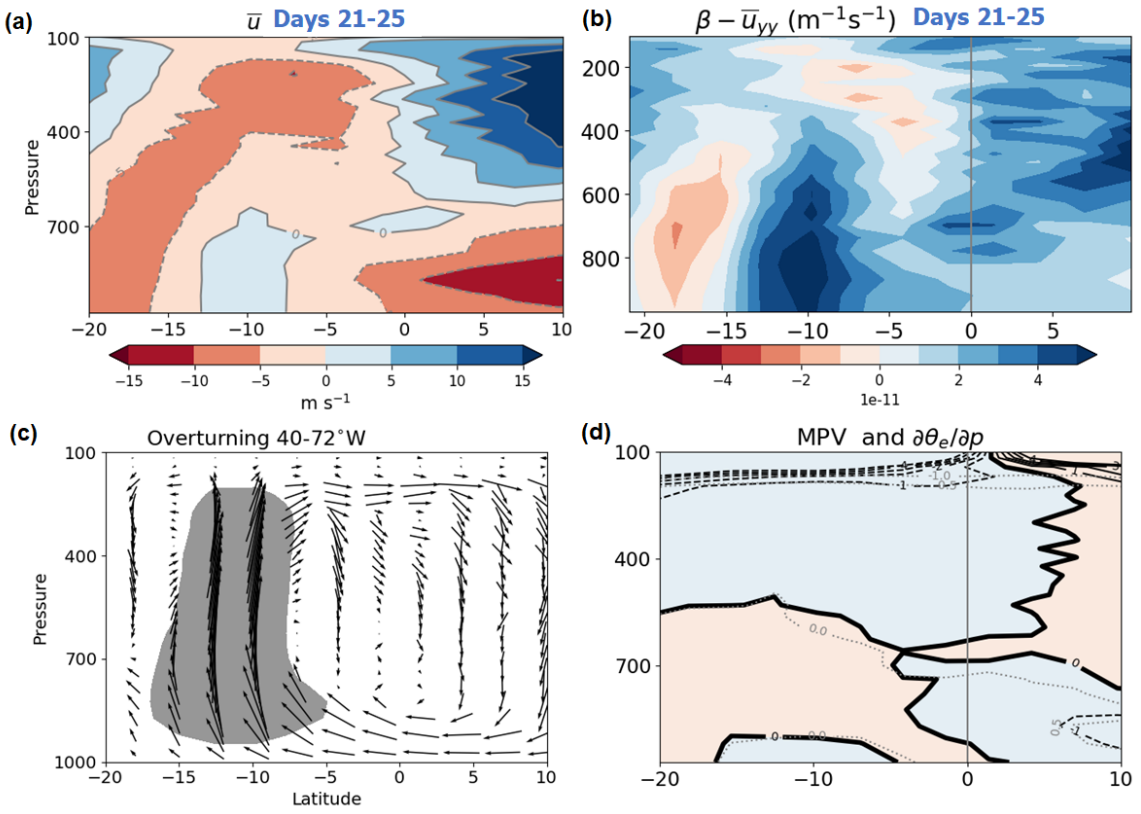



Figure 4.8: Pentad-mean zonal wind as a function of latitude and pressure, with red shading denoting easterly flow (a). Rayleigh's criterion, computed with pentad-mean winds; negative values (red) indicate a negative meridional PV gradient (b). Meridional circulation using pentad-mean meridional wind $v$ and $\omega$; gray shading indicates ascent stronger than $-0.05$ Pa s$^{-1}$ (c). Moist potential vorticity (black contours and shading) in $10^{-7}$ K m$^{-2}$ s$^{-1}$ kg$^{-1}$ and $\partial\theta_e/\partial p$ (dotted gray contours) in $10^{-3}$ K Pa$^{-1}$, using pentad-mean inputs. All four plots are limited zonal means over monsoonal longitudes (288-320°) for days 21-25 of January.

abrupt Asian monsoon transition. Moist symmetric instability accounts for the role of moisture, and is diagnosed based on the sign of the moist potential vorticity (MPV):

$$MPV = -g\left\{\frac{\partial\overline{u}}{\partial p}\left(\frac{\partial\overline{\theta_e}}{\partial y}\right)_p + \left[-\left(\frac{\partial\overline{u}}{\partial y}\right) + f\right]\frac{\partial\overline{\theta_e}}{\partial p}\right\} \tag{4.3}$$

(Krishnakumar and Lau, 1998), where $g$ is the gravitational acceleration, $\theta_e$ is the equivalent potential temperature, the $p$ subscript indicates derivatives taken on constant pressure surfaces, in accordance with the assumption that potential temperature

varies little on isobars in the tropics (Tomas and Webster, 1997; Krishnakumar and Lau, 1998). Overlines denote pentad-mean values, and other variables are as previously defined.

Figure 4.8d shows the latitude-height MPV distribution over continental longitudes during the pentad of interest. Regions where positive MPV intrudes into the Southern Hemisphere, and where the atmosphere is conditionally stable ($\partial\theta_e/\partial p < 0$), satisfy the criteria for moist symmetric instability (in particular, "potential symmetric instability" since saturation is required to release the instability; see Schultz and Schumacher (1999)) and are susceptible to slantwise overturning given a lifting mechanism (Krishnakumar and Lau, 1998). The gray dotted lines indicate that there is a deep, conditionally unstable ($\partial\theta_e/\partial p > 0$) boundary layer over the domain, as is typical throughout the tropics. However, in the mid-troposphere, the atmosphere is conditionally stable, and there are pockets of positive MPV, marked by pink shading and outlined by the heavy black MPV=0 contour. This indicates that the conditions for moist symmetric instability are also satisfied during this period of apparent inertial instability; this consistency is expected, and was also seen by Tomas and Webster (1997). However, the moist symmetric instability diagnosis is more subtle than the inertial instability perspective, and it seems cleaner to consider the dynamics alone via the inertial instability framework in this case.

As inertial instability involves only horizontal forces, it is diagnosed at a particular pressure level. It is interesting to consider the vertical extent of the inertially unstable conditions since we are interested in the role of the instability in promoting off-equatorial convergence, ascent, and precipitation. We consider the vertical structure of the absolute vorticity distribution on Day 6 of January, when the strongest monsoon-sector mean convection occurs (Fig. 4.5), accompanied by vigorous precipitation as seen on the Hovmoller diagram (Fig. 4.2a). Over continental longitudes, the zonal mean absolute vorticity profile indicates unstable conditions between the

equator and $\sim 5°$S that extend from the surface to $\sim 700$ hPa (Fig. 4.9a). This would promote convergence throughout the lower troposphere poleward of the unstable zone, which indeed occurs (Fig. 4.5). One can contrast the extent of the inertially unstable zone over continental longitudes with a remote oceanic sector of the same size. Figure 4.9b shows the limited-zonal mean $\eta$ distribution over the 174-208° oceanic longitudinal sector on Day 6. Positive absolute vorticity (shaded blue) is largely confined to the Northern Hemisphere, intruding minimally ($\sim 1°$) at various vertical levels between the surface and 400 hPa. This further supports the hypothesis that inertial instability develops over the continent due to the pronounced thermal and pressure gradients in austral summer that advect positive absolute vorticity across the equator throughout the lower troposphere. This promotes off-equatorial convection in the monsoonal sector, but not at remote longitudes.

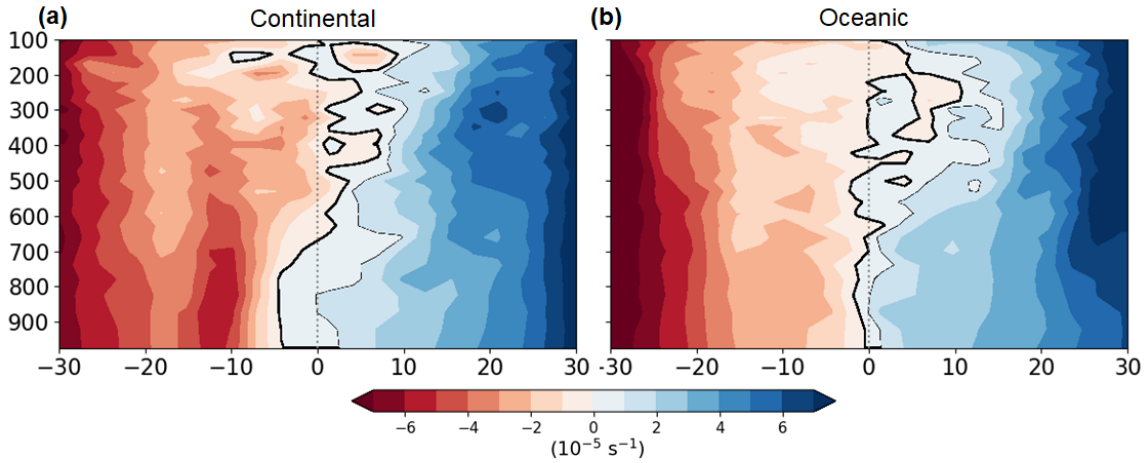



Figure 4.9: The absolute vorticity distribution ($10^{-5}$ $s^{-1}$) in the latitude-pressure plane over monsoonal longitudes (288-320°) (a) and an oceanic sector (174-208°) (b) on Day 6. The heavy black contour shows $\eta = 0$, and blue shading indicates positive absolute vorticity.

### 4.2.2 Monsoon low pressure systems

As mentioned earlier, with all three land surface moisture conditions, precipitating disturbances propagate westward across the South American continent in summer. These disturbances resemble the monsoon low pressure systems (MLPSs) that originate over the Bay of Bengal and sweep westward over the Indian monsoon sector. MLPSs are synoptic storms (horizontal scale of  2,000 kilometers (Adames and Ming, 2018)) that generate the majority of monsoon rainfall over South Asia, including the heaviest rainfall (Turner and Annamalai, 2012; Rossow et al., 2013; Sørland and Sorteberg, 2016). Despite this major role in climate, MLPSs are among the least understand modes of synoptic tropical variability (Sørland et al., 2016). Ongoing work with the present experiments will aim at characterizing these disturbances with budget analysis (Ertel potential vorticity, relative vorticity, column moisture) in order to diagnose the relevant mechanisms governing their propagation in the idealized moist model. While the results presented thus far emphasize the role of dry dynamics in D0.26 through inertial and possibly barotropic instability, there may be an important role for moist dynamics in the propagation of monsoonal disturbances. Here, we provide a brief overview of the main theories for MLPSs.

Various theories for MLPS propagation have been proposed in recent years, but they have not been broadly evaluated in models or applied to climate change studies. Boos et al. (2015) present a view of monsoonal lows as potential vorticity maxima steered westward by adiabatic advection. A series of papers by Diaz and Boos argue that the disturbances are driven by a form of moist barotropic instability in which depressions in a meridional shear interact with the latent heat release from precipitating ascent (Diaz and Boos, 2019a,b, 2021). Diaz and Boos (2021) argue based on a suite of idealized convection-permitting model experiments that MLPSs are stronger in the presence of strong low-level meridional gradients of MSE and wind shear. The former enhances the equatorward moist advection west of the disturbance, while the

latter leads to a more barotropically unstable environment. Given the development of barotropically unstable shear in response to inertial instability in D0.26 (Fig. 4.8b), it is plausible that a moist barotropic mode is at play.

Alternatively, Adames and Ming (2018) propose a framework that emphasizes interactions between moisture and potential vorticity. In their theory, dry and moist waves in the lower troposphere can trigger moisture vortex instability to initiate westward-propagating MLPSs. Meridional moisture and temperature advection leads to vortex stretching and enhanced ascent west of the low pressure center. In D0.26, the climatological JFM mean meridional moisture gradient is increasing between 0 and 15° S over the ocean (Fig. 4.1b), consistent with the prevailing moisture gradient in the Bay of Bengal.

Further evaluation of the synoptic precipitation in these simulations will draw on recent theoretical developments on MLPSs (e.g. Adames and Ming, 2018; Diaz and Boos, 2021) in order to elucidate the processes underlying simulated MLPS propagation. In another study using the same idealized moist GCM studied here, MLPS propagation appears to be largely consistent with the moisture-vortex instability theory; the anomalous Ertel potential vorticity budget indicates that latent heat release from precipitation drives propagation in the South Asian monsoon sector (Clark et al., 2020). We will evaluate whether this is also the case over a low-latitude continent, or if MLPS propagation is better characterized as a form of moist barotropic instability (Diaz and Boos, 2019b). The aforementioned theories for MLPSs underscore the importance of moist dynamics. Even if inertial instability is important for establishing convection over a dry continent, the propagation of monsoonal disturbances is likely influenced by moisture advection and latent heat release.

## 4.3 Discussion

The event-based analysis supports inertial instability as a key mechanism for precipitation development over a dry continent. Other forms of atmospheric instability may also contribute, namely barotropic instability. Further, the westward propagating precipitating disturbances in three experiments with varying land moisture conditions (D0.26, R0.26, W0.26) resemble MLPSs, thus suggesting a role for moist dynamics. It is difficult to assign causality given the complexity and variability of atmospheric conditions, or to rule out the possibility that other mechanisms contribute to monsoon development over the dry continent. However, the striking correspondence of inertial instability signatures with off-equatorial precipitation in both space and time, from a climatological perspective (Chapter 3) or on synoptic timescales, lends support to our hypothesis. The relative strength of the convection in the D0.26 experiment compared to R0.26 and W0.26 (continents with bucket hydrology or unlimited moisture; see Chapter 3), is also consistent with the expectation that inertial instability drives efficient and strong convection (Tomas and Webster, 1997).

Further exploration of these phenomena could shed light on the dynamics underlying near-equatorial (e.g. South American, West African) and off-equatorial (e.g. Indian) monsoon formation. Cross-equatorial absolute vorticity advection is frequent near the equator in solstitial seasons (Tomas and Webster, 1997; Thompson et al., 2017). Cook (2015) find that inertial instability can explain the rapid northward migration of summer rainfall over West Africa, and the existence of inertially unstable conditions in the vicinity of India suggests that this mechanism could have broad significance for understanding monsoon development (Wu and Liu, 2014; Thompson et al., 2017). Future work with the idealized moist model could target basic questions about the dynamics underlying monsoon development in the deep and outer tropics. For example, one can examine a series of experiments with a zonally symmetric continent in which the equator-side land coast is varied from a position at the equator

to 5, 10, 15, and 20°N. As the distance from the equator increases, do the instability mechanisms controlling precipitation onset change, and how does that transition play out? One might expect that in the absence of zonal asymmetry and a Somali Jet, the inertial instability mechanism is most prevalent for the equatorial continent, while barotropic or baroclinic shear instabilities are more important in the outer tropics where rotational effects are stronger and cross-equatorial $\eta$ advection does not reach the land. Further, continued research on the behavior of synoptic precipitating disturbances may reveal an important role for moist dynamics, as well as the relevance of recent theories for MLPSs.

The spatial and temporal coherence of inertial instability signatures and precipitation on climatological (Chapter 3, Figs 3.8, 3.15) and synoptic timescales provides compelling evidence that inertial instability plays a key role in monsoon development in the dry land experiment. Strong continental heating promotes inertial instability in the monsoon sector compared to a remote oceanic sector, and drives convergence strong enough to produce heavy precipitation even in the absence of local surface latent heat fluxes. This study suggests that inertial instability could be particularly relevant for monsoon onset, when the land surface is relatively dry.

# Chapter 5

# The impact of climate change on hydrological seasonality in Brazil: implications for energy system planning

## 5.1 Introduction

As climate change alters the distributions of temperature, precipitation, and other variables, infrastructure is more regularly exposed to previously infrequently occurring hazards. Systems designed for historical conditions may underperform or fail when climate regimes change. A salient example is the power sector. In Brazil, hydropower has contributed between 60 and 80% of monthly power generation since 2013, and upwards of 90% before that, when thermal (i.e. fossil fuel) and wind energy contributed smaller shares (ONS). The national electricity system is therefore highly reliant on regular and stationary streamflow patterns, and the precipitation patterns that feed them. Temporal and spatial changes in precipitation could dis-

rupt hydropower production, produce energy supply shortfalls, and interrupt social and economic functioning at large. Ensuring energy system security in the face of climate change is essential given electricity's foundational role in modern life. While this problem has gained attention recently (e.g. Arias et al., 2020), the risks have not been adequately assessed and are not formally considered in the Brazilian electricity systems' operation or capacity expansion planning (Ruffato-Ferreira et al., 2017).

Brazil's 179.2 GW of installed capacity takes the form of 7,440 generation plants from a mix of sources. In 2020, the electricity production came from hydroelectric (64.6%), fossil fuel (11.6%), wind (9.4%), other renewables (9.0%), nuclear (2.2%), and solar (1.25%) sources (Ritchie and Roser, 2020). The Brazilian Interconnected Power System Operator (ONS) oversees the entire system, comprised of these diverse power plants as well as transmission lines (Falcetta et al., 2014). The National Interconnected System (SIN for Sistema Interligado Nacional) handles over 98% of the national energy transmission, linking all states and excluding only small areas in the Amazon (Sánchez et al., 2015). This national scope reduces the strain of rainfall variability in any particular region and treats the array of hydropower plants as a joint resource (Barroso et al., 2004). However, most drainage basins exhibit similar seasonal variability, with maximum rainfall in summer and a dry period in winter (Silva et al., 2016). This limits inter-basin complementarity, and leads to reliance on thermal power during dry periods (Silva et al., 2016, see their Fig. 12a).

In the past, droughts have caused large-scale disruptions to the Brazilian electricity system, such as in the 2012-2015 drought (Zambon et al., 2016). Blackouts, transit delays, and business closures strained Brazil in 2015, and the country resorted to energy rationing in 2001. Drought risk is therefore a major concern for Brazil, which is the largest economy in South America and the 8th largest in the world (Suzuki et al., 2015). Increasing demand due to demographic and economic changes will likely

compound this risk; the Energy Research Company projects energy consumption will increase by 2.9% per year on average until 2024 (Ruffato-Ferreira et al., 2017).

The Ten-Year Expansion Plan from Brazil's Energy Research Office (EPE) published in 2017 (PDE 2027) plans for the addition of five hydropower plants in the Amazon basin, amounting to 61% of the total generation capacity expansion. The planned increase in hydropower is $\sim 10,000$ MW, amounting to a $\sim 10\%$ increase over the 2017 hydropower capacity. In Amazonia, flat topography and environmental concerns require run-of-river plant designs. Without large storage reservoirs, run-of-river hydropower production is more directly linked to instantaneous streamflow, so these plants are particularly prone to underperformance in drought conditions (de Souza Dias et al., 2018). These multi-billion-dollar infrastructure investments are based on historical expectations for rainfall and streamflow. Providing an accurate assessment of the hydropower potential that accounts for climate change is paramount, particularly in light of the additional impacts of hydropower plants on ecology and indigenous populations (de Souza Dias et al., 2018). The Brazilian Ministry of Mines and Energy commissioned a study in 2017 of the potential impacts of hydrological changes on the energy system, but the results have yet to be published or formally addressed.

Generally, drying over land with climate change is an expected consequence of land-amplified warming combined with land moisture limitations (Joshi et al., 2008; Sherwood and Fu, 2014). Further, a growing line of evidence based on climate models, observations, and theory suggests that warming will cause a systematic change in the South American monsoon seasonality, with a delayed monsoon onset and a drier spring (Biasutti and Sobel, 2009; Seth et al., 2010, 2011, 2013; Fu et al., 2013; Boisier et al., 2015; Smyth and Ming, 2020). This poses a risk to the Amazon rainforest, which is limited by dry season length (Boisier et al., 2015) and could initiate a rainforest-savanna ecosystem transition, in addition to its less-explored effects on

the Brazilian energy system. The Coupled Model Intercomparison Project Phase 5 (CMIP5) ensemble projects decreases in annual mean runoff across Amazonia, including the South American monsoon sector (Milly and Dunne, 2016a, see their Fig. 4), and CMIP6 models project mean state drying as well as more frequent and severe droughts over the Amazon with future warming (Cook et al., 2020; Ukkola et al., 2020). Different hydroclimate regimes across Brazil provide some complementarity for the interconnected hydropower system, but the monsoon regime encompasses much of the country, including the basins that drain to some of its largest hydropower plants (e.g. Belo Monte and Santo Antonio) (Fig. 5.1) (Silva et al., 2016). This emerging research suggests that the South American monsoon sector may be a hotspot for climate-energy impacts and vulnerability.

Based on various climate change simulations using two rainfall-runoff hydrologic models (Soil Moisture Accounting Procedure (SMAP) and Stochastic Linear Model (SLM)), annual streamflow is expected to decrease broadly across Brazil, including in the Amazon basin (Tiezzi et al., 2019). Ruffato-Ferreira et al. (2017) identify a risk of increased water scarcity across central Brazil based on changes in a simple water balance index, precipitation minus evaporation, in the RCP4.5 and RCP8.5 climate changes scenarios in the regional Eta-HadGEM2-ES model. A more detailed and seasonally resolved assessment that accounts for other runoff processes will better equip policymakers to respond to water scarcity risks in Brazil. Arias et al. (2020) conclude that climate change-induced streamflow changes may have a substantial impact on hydropower production in the Tapajos river basin, reducing dry season hydropower potential by over 7%. They use the terrestrial biosphere model Ecosystem Demography Model v.2 (ED2) and the HEC-ResSim to represent 37 dams and reservoirs in the Tapajos basin. By focusing on the link between large-scale climate patterns and basin-scale runoff, the present study provides a more holistic view of potential impacts. Brazil has an interconnected national energy system, so generation and pricing

may be broadly affected by changes within the monsoon sector. Our focus on robust projected changes in the hydrological cycle is key, so that physical understanding and modeling consensus underpins any adaptation measures.

Much of the available research on the vulnerability of Brazilian hydropower to climate change is based on annual mean analyses, which can obscure larger signals in the seasonal cycle and limit policy responses. For example, capacity expansion plans require seasonal projections in order to harness complementarity of regional hydrological regimes or renewable alternatives (Silva et al., 2016). The aim of this study is to leverage our best understanding of large-scale climate dynamics to improve the clarity of seasonal hydrologic projections, helping to ensure a secure and sustainable Brazilian electricity system.

## 5.2 Methods

To evaluate the impact of climate change on Brazilian hydroclimate, we utilize a state-of-the-art Earth System model: the CMIP6 generation ESM4.1 from NOAA GFDL (Dunne et al., 2020). The model represents the coupled atmosphere-ocean-land system, including climate dynamics, carbon, and chemistry. The atmospheric component, AM4.1, is run at 1 degree horizontal resolution with 49 vertical levels, and includes interactive aerosol chemistry. The land model, LM4, is also run at a 1 degree resolution, and represents land hydrology via rivers, lakes, soil, and surface and subsurface runoff, as well as ecology. Its new vegetation dynamics component is based on the Perfect Plasticity Approximation (PPA) which predicts the biomass, size, and species distributions of forests (Purves et al., 2008). The transpiration and stomatal conductance mechanism is updated from the Leuning (1995) parameterization to the Wolf et al. (2016). It includes a daily fire model instead of annual as in LM4.0, as well as annual wood harvesting, prescribed crop planting and harvesting, and grazing

on pastures and rangelands. The representation of carbon pools and cycling is also more sophisticated than previous models (see Dunne et al. (2020) for additional model details). ESM4.1's ocean model, the Modular Ocean Model Version 6 (MOM6) has a 0.5 degree horizontal resolution and includes biogeochemical dynamics.

The study evaluates three simulations: a historical scenario based on observed natural and anthropogenic forcings and emissions, and two Shared Socioeconomic Pathway (SSP) experiments. SSP245 is a "middle of the road" scenario with 4.5 W $m^{-2}$ end-of-century radiative forcing, while SSP585 is a scenario of "fossil fueled development" in which economic growth and energy use are largely unconstrained and end-of-century radiative forcing reaches 8.5 W $m^{-2}$ (O'Neill et al., 2017). These two alternative futures allow us to consider a plausible range of future hydrological changes. Integrated Assessment Model simulations based on these alternative climate change narratives provide quantitative trajectories of emissions and land use changes (O'Neill et al., 2017). Both SSPs assume continued tropical deforestation, with moderate regulations gradually slowing the rate of forest loss (O'Neill et al., 2017; Estoque et al., 2020). The SSP narratives also assume that crop yields rapidly increase in SSP585, while crop yield increases slow over time in SSP245 (Estoque et al., 2020). It is worth underscoring that the SSP narratives are fixed, so that changes in the ESM do not feed back on the prescribed SSP scenarios (e.g. regardless of the ESM simulated changes in the Amazon rainforest, the SSP245 scenario will result in 4.5 W $m^{-1}$ radiative forcing). Further, this study does not make assumptions about Brazil's climate change policies, and the impacts those might have on emissions or power system management.

The analysis focuses on the climate response within the South American monsoon sector (5-18° S, 40-72° W), which encompasses six significant basins for the Brazilian hydropower system (Fig. 5.1; Table 5.1). The Santo Antonio Dam is of particular interest, as it is one of the world's largest run-of-river dams and has minimal storage

capacity. It is located in the western monsoon sector on the Madeira River, the Amazon's largest tributary. Also noteworthy is the Belo Monte Dam on the Xingu River. Belo Monte is Brazil's second largest dam in terms of installed capacity, following the binational Itaipu Dam. Both the Madeira and Xingu rivers exhibit enormous seasonal variability in streamflow, with summer inflows 7 and 20 times higher than dry season inflows, respectively (Kelman and Harrison, 2019). Rather than assessing the model-simulated streamflow at the grid cells corresponding to dam locations, we integrate the total runoff, which includes surface and sub-surface flow, over the drainage basins outlined in Figure 5.1. This variable represents the net water yield and corresponds well with streamflow within the basin, and avoids limitations to the simulated river network due to the resolution and grid configuration.

All results are based on 20-year mean climatologies in each experiment: years 1985-2004 in the historical run, and 2081-2100 in the SSP experiments. Some mid-century results (2051-2070) for runoff changes are included in the interest of informing nearer-term energy system planning. The analysis uses only one model, GFDL ESM4.1, so its biases limit our conclusions, though we focus on pronounced signals that appear to be robust aspects of the climate response across the existing literature (Biasutti and Sobel, 2009; Seth et al., 2010, 2011, 2013; Joetzjer et al., 2013).

Table 5.1: Descriptions of Brazilian hydropower plants of interest.

| **Dam** | **Capacity (MW)** | **Details** |
|---|---|---|
| Santo Antonio | 3,568 | Run-of-river dam + 271 $km^2$ reservoir |
| Teles Pires | 1,820 | Run-of-river dam + 150 $km^2$ reservoir |
| Belo Monte | 11,233 | Dam + 440 $km^2$ reservoir. $2^{nd}$ largest dam in Brazil, $4^{th}$ in world |
| Tucurui | 8,370 | Dam + 2,850 $km^2$ reservoir |
| Lajeado | 902.5 | Dam + 630 $km^2$ reservoir |
| Serra de Mesa | 1,275 | Dam + 1,784 $km^2$ reservoir |

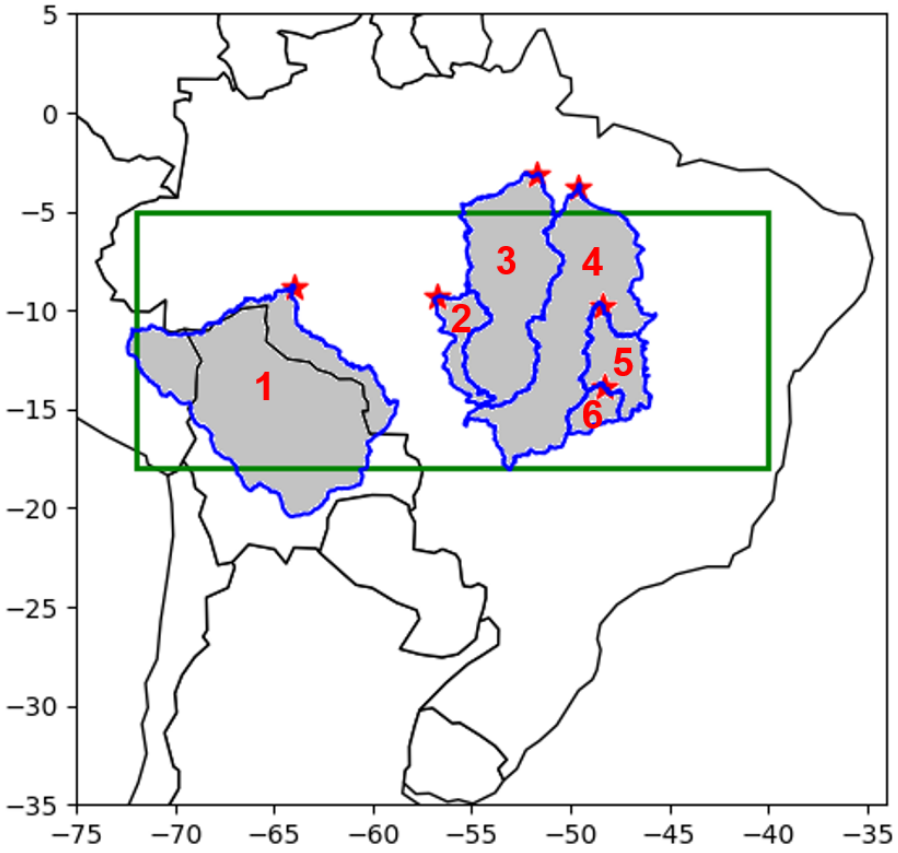



Figure 5.1: A map of the drainage basins of interest in Brazil. The Santo Antonio Dam is located in basin 1, Teles Pires in basin 2, Belo Monte in basin 3, Tucurui in 4, Lajeado in 5, and Serra de Mesa in 6. The green box denotes the monsoon sector.

## 5.3 Results

### 5.3.1 The monsoon-sector climate response

To establish whether the GFDL ESM4.1 model is an appropriate tool for the questions of interest, we evaluate the realism of its simulation of South American precipitation. Figure 5.2a shows the seasonal cycle of precipitation averaged over the monsoon sector for 20 years of the historical simulation along with the GPCPv1.2 observations over the period 1996-2015. The model captures the monsoon seasonality with improved fidelity compared to previous generation Earth System Models which were plagued by

dry biases (Sakaguchi et al., 2018; Joetzjer et al., 2013; Yin et al., 2013). Some biases persist: the model produces $\sim 2$ mm $d^{-1}$ excessive precipitation in summer (December through February or DJF), and produces a longer and slightly drier dry season than observed. The dry bias in the monsoon onset season (September through November, or SON) could bias the drying response to warming exhibited in this season, which we will evaluate at length. The simulated annual mean boundary layer flow over South America compares favorably with ERA-Interim reanalysis (Fig. 5.2b), while the specific humidity distribution illustrates a slight dry bias from the West Atlantic to the interior Amazon basin. However, the humidity gradients are well captured, and the general South American hydroclimate is adequately represented to warrant further analysis, especially compared to previous models.

Figure 5.3a-b shows the monsoon sector region-mean seasonal cycles of temperature, precipitation, and evaporation in the historical, moderate emissions, and high emissions pathways. Surface warming is strongest in spring, with 7.7 K warming in SSP585 compared to 4.4 K in the fall (March through May, or MAM). This differential warming is related to differences in the surface energy budget due to varying surface water availability throughout the seasonal cycle. We will elaborate on this important point later. The precipitation curves demonstrate that in GFDL ESM4.1, consistent with many other models and with previous work for this dissertation, warming produces a drying of the monsoon onset season (spring, September-November or SON), amounting in a longer, drier dry season (Fig. 5.3b). Precipitation decreases severely through the spring and early summer; September precipitation decreases by over 60% even in the moderate emissions scenario (Fig. 5.3c). In terms of absolute change, mean precipitation decreases by 1.5 and 3.5 mm $d^{-1}$ in November in SSP245 and 585 respectively. Later in the summer and fall (January through May) precipitation decreases by 10% ($\sim$1 mm $d^{-1}$) in the high emissions scenario, and responds minimally in SSP245. While the percent change is large in the dry season (June through

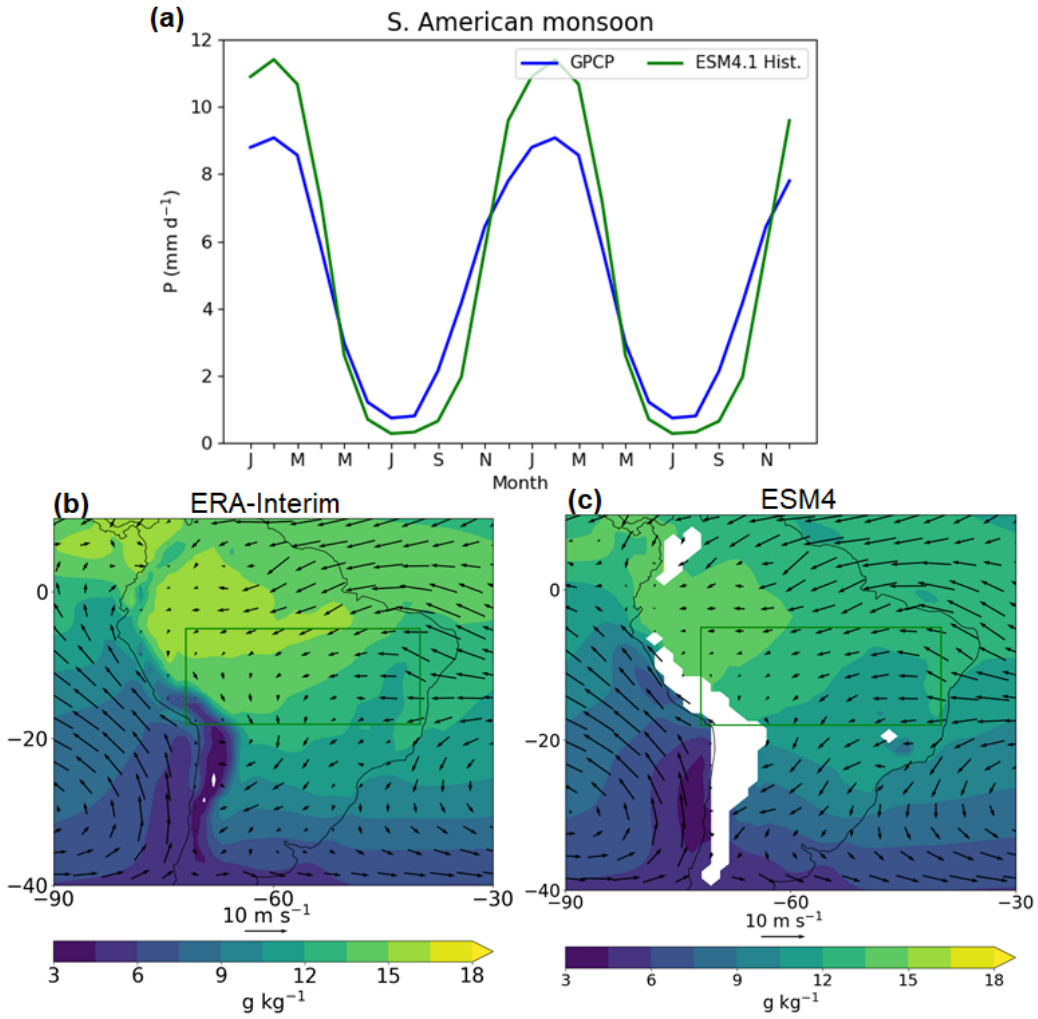



Figure 5.2: The annual cycle of precipitation over the monsoon sector (a), the near-surface (925 hPa) annual mean winds and specific humidity in reanalysis (b) and in ESM4.1 (c).

August, JJA), climatological rainfall is very low, and the absolute change is less than 1 mm d$^{-1}$ in both scenarios. Figure 5.4 illustrates the spatial pattern of the precipitation response, with clear appreciable decreases in all three climatologically raining seasons (spring, summer, fall). The pronounced drying signal in the west stands out, particularly in spring (SON), and remains prominent throughout the analysis.

The evaporation response (Fig. 5.3b, solid lines) shows little change between scenarios in the wet months, a reduction of evaporation in the dry season and an even

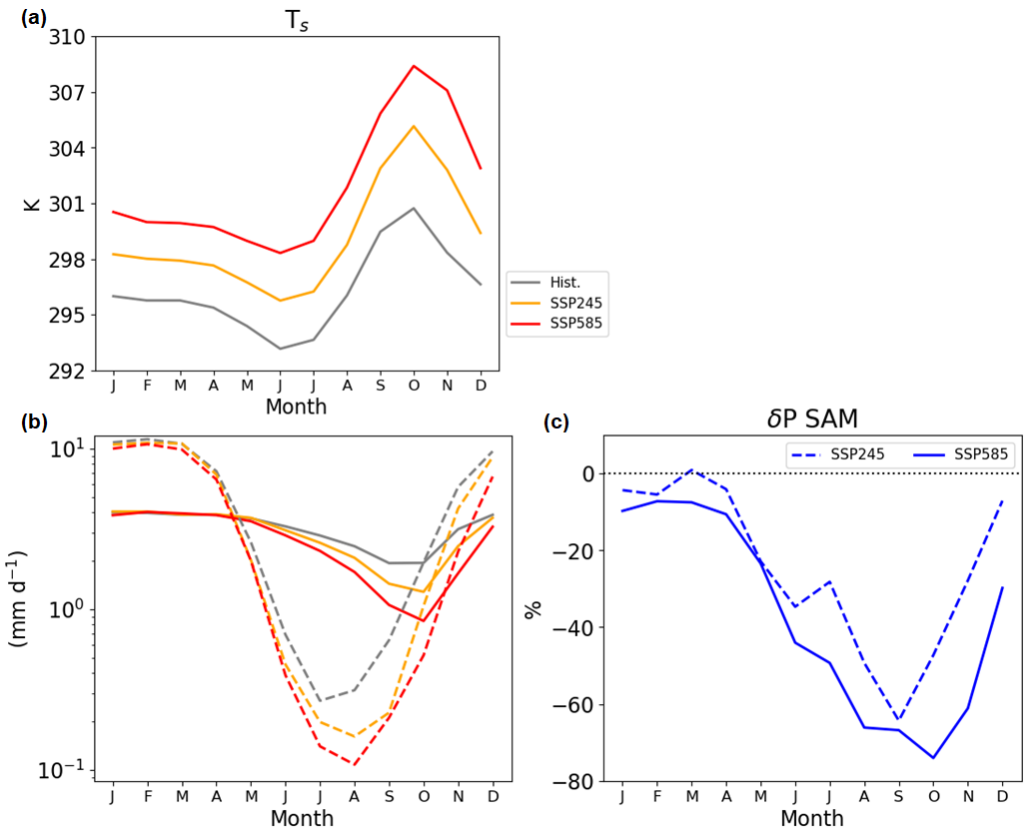



Figure 5.3: The annual cycle of monsoon-sector mean surface temperature in the historical, SSP245, and SSP585 simulations (a), the annual cycle of precipitation (dashed) and evaporation (solid) on a logarithmic axis (b), and the percent change in precipitation in each month.

stronger reduction in spring. In the high emissions scenario, evaporation decreases by 1.2 mm $d^{-1}$ in SON, a 50% decrease from the historical value. Evaporation declines by 0.6 mm $d^{-1}$ (21%) in JJA, and by less than 0.3 mm $d^{-1}$ in DJF or MAM. In SSP245, spring evaporation decreases by 0.7 mm $d^{-1}$ (28%) in SON and 0.3 mm $d^{-1}$ (11%) in JJA. Warming increases the atmospheric moisture demand which would tend to increase evaporation where moisture is available, assuming little change to the surface winds. The opposing responses of surface temperatures and evaporation over the monsoon sector in winter and spring suggest an increasingly water-limited climate.

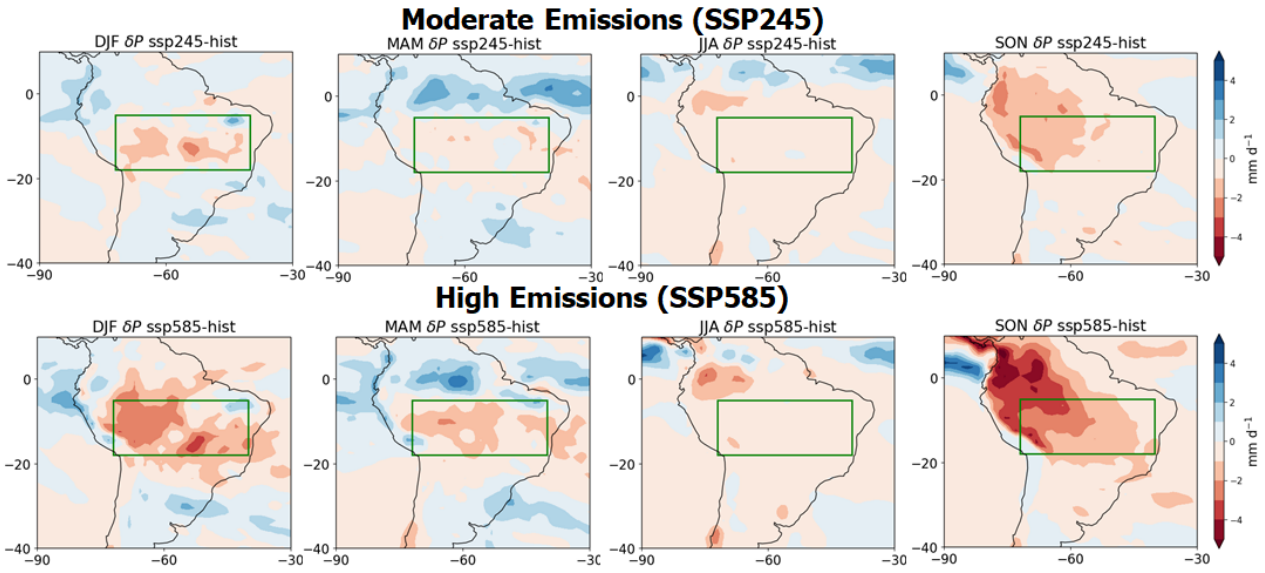



Figure 5.4: Seasonal mean distributions of end-of-century (2081-2100) precipitation anomalies (SSP-hist.) in the moderate (upper) and high (lower) emissions scenarios.

The time at which mean precipitation exceeds evaporation in the spring denotes the seasonal onset of positive net precipitation (P-E). Precipitation minus evaporation and storage constitutes the runoff which ultimately drives streamflow. We consider daily model output to quantify changes in the timing of this seasonal transition. In the historical experiment, the daily mean P-E is positive from October 20 through the rainy season. In SSP245, positive P-E is delayed only three days relative to the historical experiment. In SSP585, the daily mean P-E oscillates around zero in early spring, and sustained positive P-E commences on November 13, 23 days later than in the historical experiment. This delayed onset of positive P-E is consistent with previous work that concludes warming will likely delay monsoon onset globally (Biasutti and Sobel, 2009; Seth et al., 2011). A longer average dry season could make the region more prone to drought, and push hydropower storage past its limits, leading to supply shortages and blackouts as in historical drought episodes. It is worth noting that the decrease in evaporation in spring described previously reduces the delay of positive net precipitation compared to a case in which evaporation is unchanged from

the historical scenario (see intersection of precipitation and evaporation lines). This emphasizes the importance of including a land model that accurately represents soil moisture and transpiration in order to accurately project changes in the seasonality of water availability and runoff.

The differing precipitation and evaporation responses throughout the seasonal cycle hint at the seasonal evolution of climatic regimes in the monsoon sector. A Budyko Curve illustrates this point: Figure 5.5 show the relationship between the aridity index, the ratio of potential evapotranspiration (PET) to precipitation, versus the moisture recycling ratio, evaporation over precipitation. We compute the season-mean value for each year and average over 20 years, with error bars indicating the interannual standard deviation. PET can be estimated in numerous ways; we opt for the "energy-only" approach which is both the simplest and best performing metric (Milly and Dunne, 2016b). PET is computed as 80% the net surface downward radiative flux, an empirically based estimate of the partitioning of latent and sensible heat fluxes in a regime unlimited by water availability (Koster and Mahanama, 2012). The one-to-one line on Fig. 5.5 represents the energy limit for surface evaporation, in which the actual evaporation attains its maximum theoretical value. The climatological mean values for both the peak monsoon season and the fall (DJF, MAM) cleanly fall in this regime. When rainfall is most vigorous, surface water is plentiful and Amazonia's "Green Ocean" nickname is apt (Williams et al., 2002). Summer and fall remain in this regime in the SSP experiments, with no significant change along either axis. Spring is a different story. The historical SON regime is moisture-limited, with evaporation falling well below its potential value (PET/P $>$ 1 and E/P $<$ 1). In the SSP simulations, the aridity index increases markedly, due to both increasing atmospheric moisture demand and decreasing precipitation. The E/P ratio also increases, as precipitation decreases more than evaporation in the monsoon sector. The winter (JJA) data are not pictured, since the monsoon-sector precipitation is so small that

the ratios are extremely high; to summarize, JJA is arid and becomes more so in the SSP experiments. Figure 5.5 succinctly encapsulates the differing initial hydrological regimes throughout the seasonal cycle, as well as the differing propensities to change with warming.

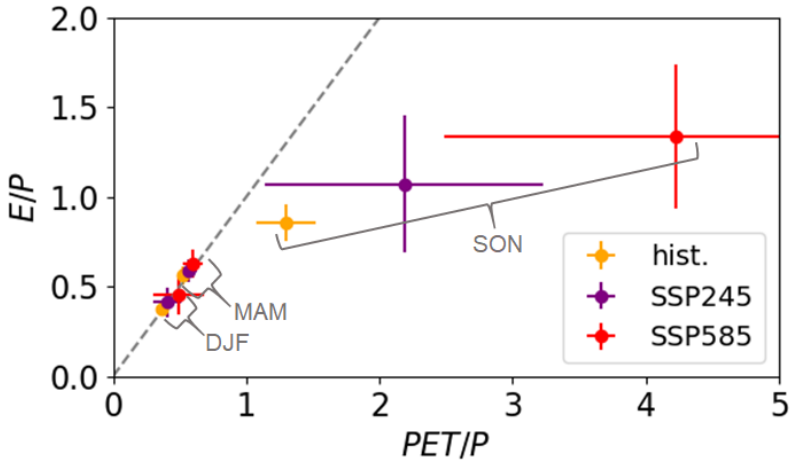



Figure 5.5: A Budyko plot using season-mean data from the three simulations. The vertical and horizontal error bars indicate the population standard deviation based on 20 years of season-mean data for each point.

A surface energy budget analysis reinforces this picture of seasonally varying hydrological regimes. In summer and fall, the Bowen ratio (ratio of sensible to latent heat fluxes) is 0.18 and 0.17 respectively in the historical simulation, and it remains below 0.3 in the SSP experiments. Note that these values hover around the 80% theoretical ratio of latent to total turbulent heat fluxes used to calculate PET. In both summer and fall there is less than 5 W $m^{-2}$ anomalous upwelling surface longwave radiation in SSP585 compared to the historical experiment due to surface warming, and the net downward shortwave flux increases by 6.5 and 5.6 W $m^{-2}$ in summer and fall respectively. Overall, the surface energy budget response is muted in the two rainiest seasons. The surface energy budget in spring differs starkly. The Bowen ratio in the historical simulation is 0.8. The ratio of latent to total turbulent fluxes is 0.55, well below the 0.8 empirical maximum estimate. In SSP245 and 585, the Bowen ratio

exceeds 1, with values of 1.3 and 2.2 respectively. SON sensible heat fluxes increase (by 10.6 and 18.3 W $m^{-2}$ in SSP245 and 585), while latent heat fluxes decrease by nearly twice the magnitude (by  19 and 35 W $m^{-2}$). The large reduction in upward latent heat fluxes is also compensated by anomalous upwelling longwave radiation ( 12 and 20 W $m^{-2}$ in SSP245 and 585). The increase in downward shortwave radiation is of a similar magnitude as in summer and fall. The surface energy budget is similar to spring in the dry season, JJA, though it is interesting to note that the Bowen ratio is lower in JJA than SON (0.5 vs. 0.8) in the historical simulation.

We consider meteorological, agricultural, and hydrological drought indicators, and all demonstrate aridification, especially in spring, with future warming (Fig. 5.6). The patterns described are similar but of a lesser magnitude in the SSP245 experiment. As previously described, evaporation decreases in the monsoon onset season, with the strongest signal to the west and along the southern margin of the monsoon sector (Fig. 5.6a). By contrast, evaporation changes by less than 1 mm $d^{-1}$ in summer and fall. Transpiration changes dominate the decreases in dry season evaporation, demonstrating the importance of vegetation in the surface climate response (Fig. 5.6b). Consistent with this, the stomatal conductance decreases across the continent, but particularly in the western monsoon sector (by more than 60% its control values) (Fig. 5.6c). Stomatal conductance decreases throughout the year, as expected due to the CO2 physiological effect (Cao et al., 2010), but the magnitude and spatial pattern are pronounced in spring and winter, suggesting a heightened response due to plant water stress. Drying soils also suggest water stress as a culprit for reduced evaporation, particularly in western monsoon sector (Fig. 5.6e). The upper-column soil moisture decreases throughout the year, with the most pronounced changes in the west, especially during the dry season and spring.

Finally, the vegetation fraction decreases across the sector, particularly in the west and along the southern margin, where reductions are as high as 40% (Fig. 5.6f). This

highlights the ecosystem risks of climate change in South America, which can feed back on water availability (e.g. Pielke et al., 1998). In the annual mean, the vegetation fraction decreases by more than 10% along the southern monsoon sector, with local changes exceeding 30% in places (not shown). Southern Amazonia is known to be vulnerable to a rainforest-savannah ecosystem transition (Fu et al., 2013), and the GFDL ESM4.1 experiments underscore this risk.

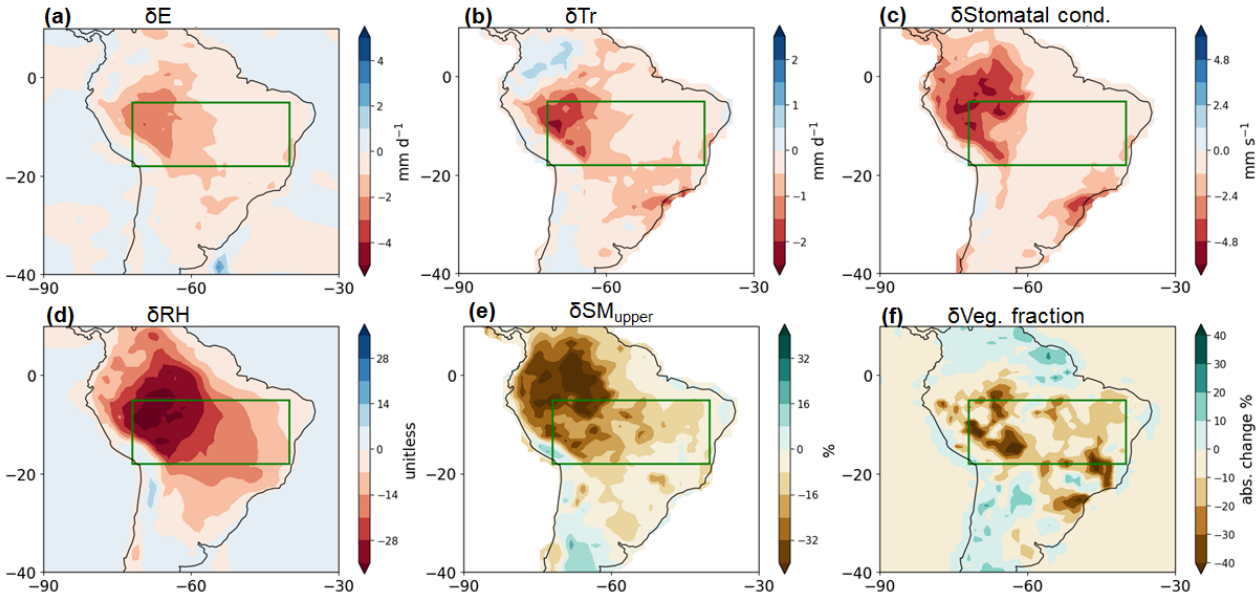



Figure 5.6: SON anomalies (SSP585-hist) of evaporation (a), transpiration (b), stomatal conductance (c), 2-meter relative humidity (d), upper-column soil moisture (e), and vegetation fraction (f).

To better understand the physical drivers of the drying response, we consider an idealized forcing simulation from the C4MIP (carbon cycle Model Intercomparison Project) protocol. To discern whether the plant response (Fig. 5.6b,c) is driven by the $CO_2$ physiological effect or water scarcity, we examine the 1% year$^{-1}$ radiatively-coupled experiment ("1pctCO2-rad"), in which the radiation code is affected by the increasing $CO_2$ concentrations but the carbon cycle model sees repeating 1850 $CO_2$ concentrations. Unlike the SSP experiments, there are no prescribed changes in land use or emissions aside from the idealized increase in $CO_2$. The mean state averaged

over years 131-150 of the experiment exhibits drying patterns relative to the historical experiment that resemble the SSP585 results in space and time (not shown). The drying response over the monsoon sector is most pronounced in spring and is amplified in the west. Precipitation decreases by up to 3 mm $d^{-1}$ in the west and relative humidity decreases by over 20%. Evaporation decreases by up to 2 mm $d^{-1}$ in the western monsoon sector, with transpiration dominating the change. This demonstrates that the patterns of drying and of reduced evapotranspiration are produced by the radiative impact of $CO_2$ alone, without the direct effect of increased carbon concentrations on plant stomatal conductance. This is important because the radiative impact of $CO_2$ is more robust than its direct effect on plants, and because it demonstrates that water scarcity alone, absent the $CO_2$ physiological response, can induce changes in stomatal conductance and transpiration similar to those seen in the SSP experiments.

The heightened aridification patterns in spring and winter alter the annual mean climate, again highlighting the growing water supply risk with climate change in this region. Maps of the inverse aridity index, P/PET, illustrate the shift to a water-limited climate regime (Fig. 5.7). In the historical simulation, P/PET $> 1$ across most of the monsoon sector and the rainforest ecosystem to the north. In SSP585, reductions in P/PET are clear in the west and along the southern monsoon sector; where P/PET falls between 0.5-0.65, the land is classified as dry sub-humid (Middleton and Thomas, 1997).

The spring surface climate response elicits a dynamic response, as illustrated in Figure 5.8. The near-surface heating, as high at 10 K in the inner basin, drives anomalous boundary layer thermal convergence (Lindzen and Nigam 1987) (Fig. 5.8b). The near-surface specific humidity response demonstrates the breakdown of the thermodynamic scaling for water vapor. According to the Clausius-Clapeyron relation, saturation vapor pressure increases by $\sim 7\%$ $K^{-1}$, so assuming little change in relative humidity, specific humidity should also increase at this rate. In the inner basin, tem-

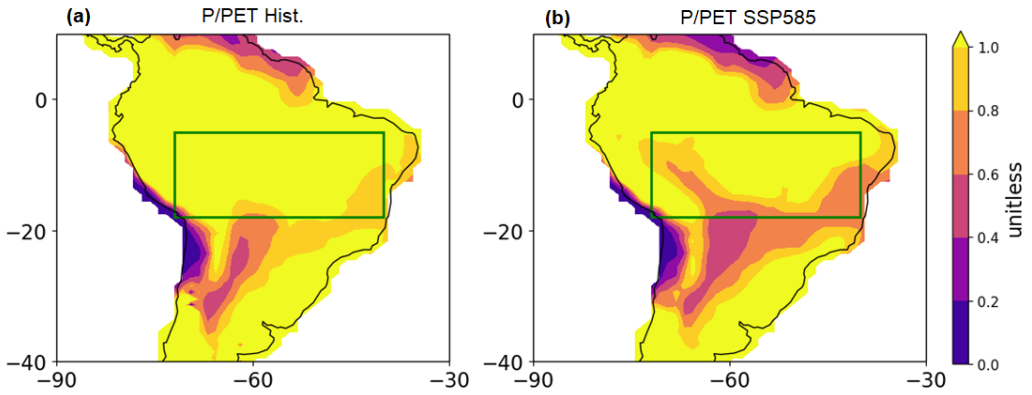



Figure 5.7: Annual P/PET in the historical (a) and SSP585 (b) simulations. The PET is computed following (Milly and Dunne, 2016a).

perature increases by ∼10 K, while specific humidity actually decreases rather than increasing by 70%. Accordingly, near-surface relative humidity decreases drastically (Fig. 5.6d).

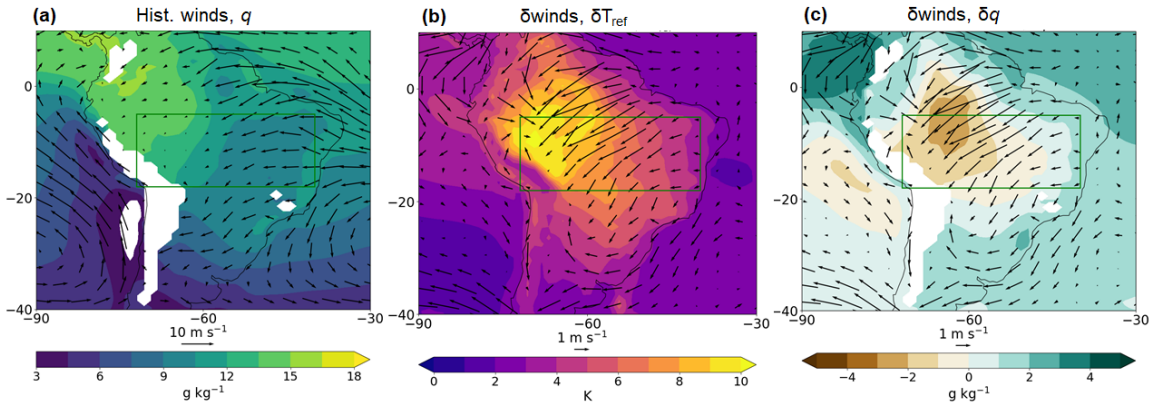



Figure 5.8: The historical (a) and anomalous (SSP585 - historical) SON mean near-surface winds and temperature (b) and moisture (c).

Relative humidity decreases over land are expected with warming (e.g. Joshi et al., 2008; Sherwood and Fu, 2014); the key mechanistic arguments are presented in Byrne and O'Gorman (2016) and summarized here. Assuming oceanic control of land boundary layer specific humidity and small changes in oceanic relative humidity, warming should produce equal fractional changes in specific humidity over land and ocean. One

expects amplified warming over land due to approximately uniform free tropospheric warming in the tropics combined with different dry and moist adiabatic lapse rates operating over land and ocean (Byrne and O'Gorman, 2013). Taken together, these statements imply that equal fractional changes in specific humidity over land and ocean will cause relative humidity to decrease over land. This explains the general pattern of relative humidity reductions over land in climate change simulations. Such changes can be amplified due to moisture forcing; the pronounced land relative humidity decrease in the western monsoon sector complies with the conceptual picture presented by Byrne and O'Gorman (2016). Dynamic constraints, namely the atmospheric processes that smooth free tropospheric temperatures throughout the tropics, link the moist static energy over land and ocean ($h_l$ and $h_o$, respectively) such that changes in $h_l$ approximately equal changes in $h_o$: $c_p\delta T_l + L_v\delta q_l = c_p\delta T_o + L_v\delta q_o$ (Byrne and O'Gorman, 2016, Eq. 11). If greenhouse gas forcing drives an increase in $T_o$ and $q_o$, increasing $h_o$, and moisture forcing over land (e.g. stomatal closure or soil moisture reduction as in Fig. 5.6c,e) simultaneously reduces $q_L$, the $T_L$ increase must be correspondingly stronger to satisfy the above equation. The changes in both $q_l$ and $T_l$ contribute to reductions in $RH_l$. In this way, temperature changes strongly amplify the land relative humidity response to moisture forcing (Byrne and O'Gorman, 2016). Berg et al. (2016) also conclude that land-atmosphere feedbacks triggered by reduced soil moisture amplify aridity increases over land with warming.

It is interesting to consider what leads to the zonal pattern of the drying, with clearly amplified drying in the western monsoon sector. The western basin is remote from the oceanic moisture inflow from Atlantic easterlies, and westerly inflow is blocked by the Andes Mountains. Therefore, the western basin is more dependent on continental evaporation as a moisture source (Zemp et al., 2017; Findell et al., 2019). The relative humidity over the continent decreases with warming (Byrne and O'Gorman, 2016), so the winds over the western continent converge relatively dry

air in the warmer climate, exacerbating the relative humidity decrease in the inner continent.

### 5.3.2 Runoff changes in key hydropower basins

In all six drainage basins of interest (Fig. 5.1), the basin mean precipitation reductions are greatest in spring, and they are accompanied by smaller evaporation reductions, a large proportion of which come from transpiration changes (Fig. 5.9). The hydrological response is consistent with the large-scale changes described in the previous section, indicating that these precipitation shifts are a manifestation of the monsoon shift. These precipitation changes do not directly correspond to runoff changes; the rainfall-runoff transformation process causes runoff to lag precipitation. The process is complicated and depends on basin characteristics like geology (slope steepness), surface processes like evaporation and percolation, vegetation properties, soil properties that affect seasonal storage, and more (Dunne, 1978). The Amazon basin is very flat, so there are significant lags between precipitation and runoff. The slow response time is evident in the seasonal cycle of the basin-integrated runoff, as well as the timing of runoff changes in the SSP experiments (Fig. 5.10). In the historical simulation, while precipitation steadily increases from September through the summer, runoff does not increase from its dry season baseline level until December in all basins except Santo Antonio. In the SSP585 experiment, while precipitation reductions are most pronounced in terms of absolute and percent change in spring, the runoff changes across the monsoonal basins are most pronounced in summer and early fall due to the inherent lag in the rainfall-runoff process (Fig. 5.10).

In four of the basins, these changes are statistically significant for at least one season by a two-sample Kolmogorov-Smirnov (K-S) test (Table 2). The basin that drains to the Belo Monte dam, the second largest hydropower plant in Brazil which supplies electricity to 60 million people, exhibits significant total runoff reductions

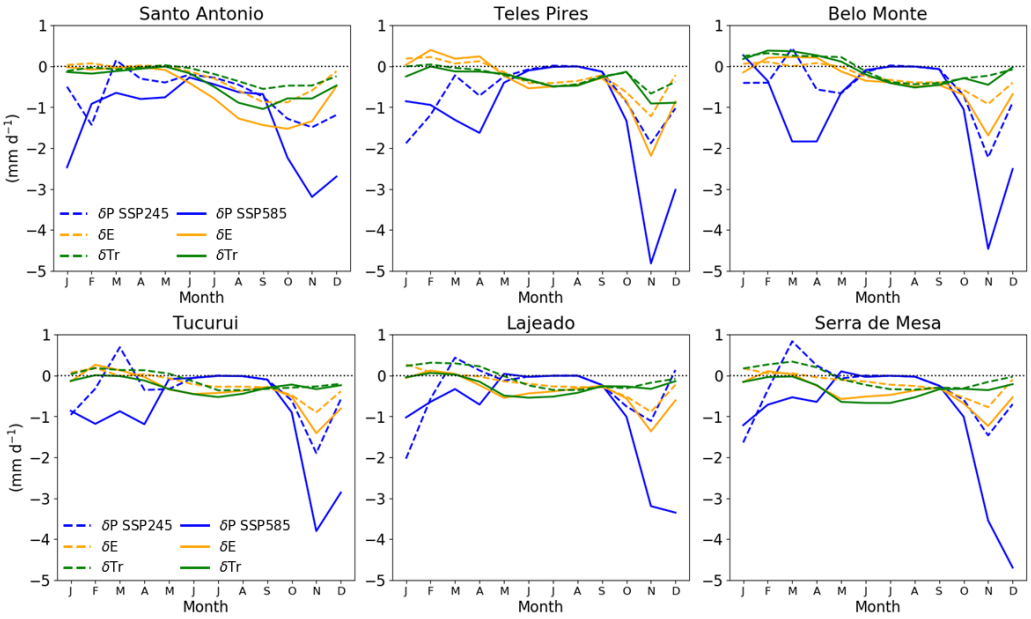



Figure 5.9: The anomalous annual cycles of precipitation, evaporation, and transpiration averaged over the six drainage basins for SSP245 (dashed) and SSP585 (solid).

in spring, summer, and fall by end-of-century in SSP585. The spring reduction is significant by mid-century (2051-2070) in SSP585. Even in the moderate emissions experiment, the spring runoff reduction is significant by mid-century in the Belo Monte dam drainage basin. This indicates that there is a risk that even with climate change mitigation and moderate warming, this recently completed major hydropower plant will experience lower average streamflow at the end of the dry season when reservoir storage is already low.

Based on the ESM4.1 analysis, the Santo Antonio Dam may also be exposed to significantly lower streamflow in the coming decades due to climate change. The Santo Antonio Dam is one of the five largest in Brazil and supplies power to 44 million people. It is a relatively new development (2016 completion) representing an $8 billion investment. It is a run-of-river dam with minimal storage capacity, and therefore little means to buffer the impact of seasonal streamflow reductions on power generation. In the SSP585 experiment, the basin-integrated runoff decreases

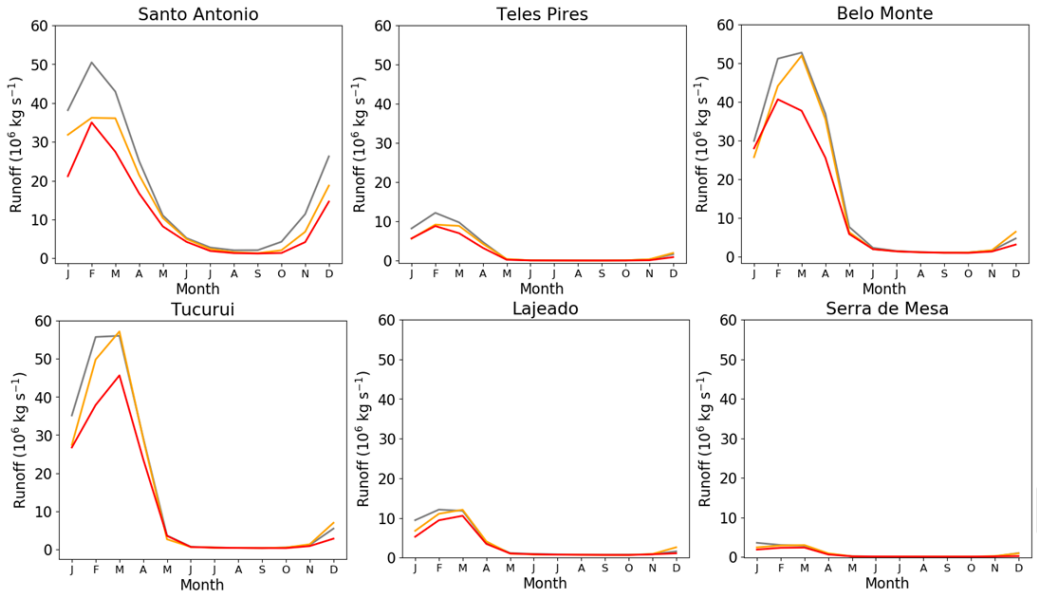



Figure 5.10: Annual cycles of total runoff integrated over the basin area for each of the six dams of interest in the historical, SSP245, and SSP585 simulations.

significantly in all four seasons by end-of-century, and in spring, summer, and winter by mid-century. With moderate emissions, the runoff reductions are also significant by mid-century in spring, summer, and winter. Santo Antonio is in the westernmost drainage basin, and while the summer runoff in strongest, climatological runoff is also substantial in spring, and there are marked spring runoff reductions (over 50% in Oct and Nov).

Given the magnitude and statistical significance of the runoff changes, as well as the location of the dam in the western basin where the aridification changes are most pronounced (Fig. 5.6), we consider the Santo Antonio basin in greater detail. Figure 5.11 shows the probability density functions (PDFs) for 20 years of monthly total runoff data in each season (N=60 for each simulation on each subplot). The PDFs show a clear shift of the runoff distributions towards more frequent low-runoff months in SSP585 in all seasons. While an average reduction of streamflow and hydropower production throughout the year is a concern in itself, the increased frequency of low-runoff months during and following the dry season increases the likelihood of very

Table 5.2: P-values from two-sample K-S test comparing basin-integrated runoff to historical simulation output.

| | SON | | | | DJF | | | |
|---|---|---|---|---|---|---|---|---|
| | ssp585 | | ssp245 | | ssp585 | | ssp245 | |
| | mid | end | mid | end | mid | end | mid | end |
| Santo Antonio | <.0001 | <.0001 | <.01 | <.001 | <.001 | <.0001 | <.05 | <.01 |
| Teles Pires | 0.10 | <.001 | 0.10 | 0.06 | <.05 | <.05 | 0.34 | 0.06 |
| Belo Monte | <.03 | <.001 | <.03 | <.01 | 0.48 | <.05 | 0.48 | 0.24 |
| Tucurui | 0.24 | 0.16 | 0.24 | 0.91 | 0.34 | 0.16 | 0.78 | 0.24 |
| Lajeado | 0.10 | <.001 | 0.10 | 0.06 | <.05 | <.05 | 0.34 | 0.06 |
| Serra de Mesa | 0.34 | 0.63 | 0.48 | 0.48 | 0.16 | 0.06 | 0.91 | 0.78 |

| | MAM | | | | JJA | | | |
|---|---|---|---|---|---|---|---|---|
| | ssp585 | | ssp245 | | ssp585 | | ssp245 | |
| | mid | end | mid | end | mid | end | mid | end |
| Santo Antonio | 0.16 | <.01 | 0.78 | 0.48 | <.001 | <.0001 | <.05 | <.01 |
| Teles Pires | 0.35 | 0.10 | 0.78 | 0.48 | 0.24 | 0.10 | 0.48 | 0.24 |
| Belo Monte | 0.16 | <.01 | 0.16 | 0.62 | 0.48 | 0.34 | 0.78 | 0.34 |
| Tucurui | 0.98 | 0.48 | 0.99 | 0.78 | 0.78 | 0.48 | 0.78 | 0.78 |
| Lajeado | 0.35 | 0.10 | 0.78 | 0.48 | 0.24 | 0.10 | 0.48 | 0.24 |
| Serra de Mesa | 0.78 | 0.24 | 0.91 | 0.91 | 0.34 | 0.91 | 0.91 | 0.78 |

low production periods that could lead to power supply shortages and electricity price spikes. Current Brazilian capacity expansion plans call for further development of run-of-river plants in the Amazon basin, but these results for Santo Antonio highlight the risk of investing in run-of-river hydropower capacity based on historical streamflow patterns.

The Teles Pires and Lajeado drainage basins are impacted by significant spring and fall runoff reduction in the SSP585 end-of-century simulation compared to the historical baseline. Teles Pires is a run-of-river hydro plant, like Santo Antonio, so there would not be an operational solution to reduced instantaneous streamflow, like optimizing reservoir levels, when making system management decisions. The runoff changes are not significant by the K-S test in Serra de Mesa or Tucurui hydropower plants due to high runoff variability.

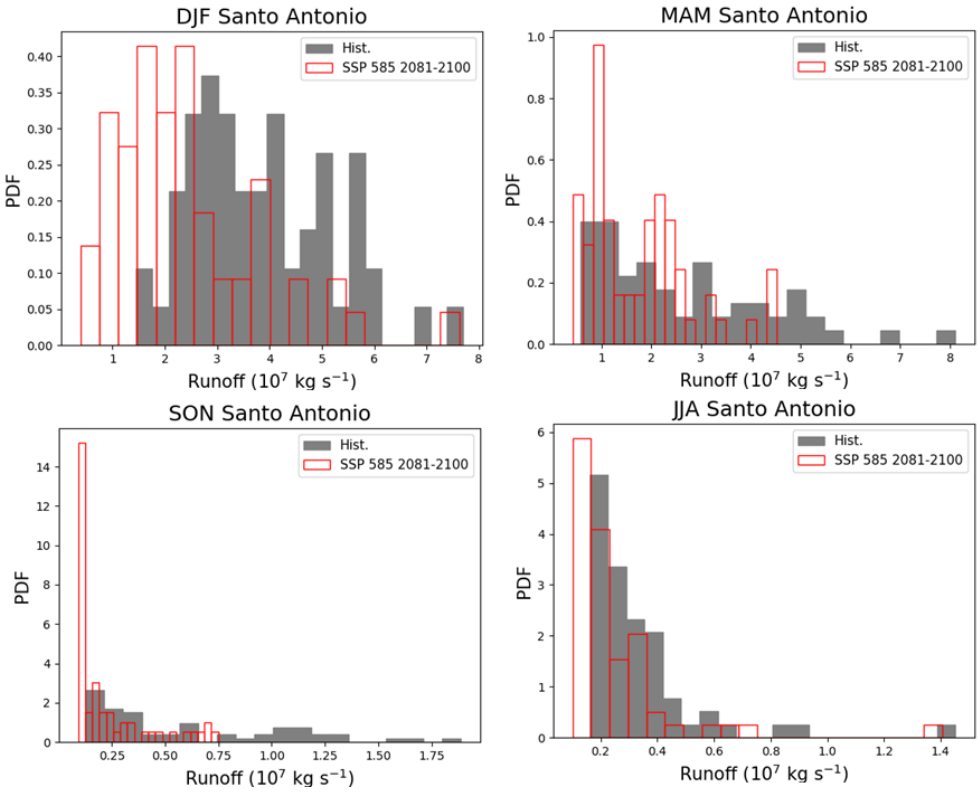



Figure 5.11: PDFs of monthly runoff for each of the four seasons in the drainage basin feeding the Santo Antonio Dam. The historical data is shaded gray, and the SSP585 data is in red. Each season includes 20 years of data for 3 months, so there are 60 values for each experiment.

## 5.4 Policy implications

In ESM4.1, continued emissions lead to a shift in South American monsoon seasonality with reductions in precipitation in spring, summer, and fall. The precipitation changes are particularly severe in spring, during monsoon onset, and lead to increasingly arid conditions across a broad area of South America (Fig. 5.4), including significant changes in seasonal runoff (Fig. 5.10, Table 5.2). The mean drying is most pronounced in the inner continent, to the west. The severity of these hydrological changes is substantially lower with mitigation (SSP245), though significant seasonal runoff reductions still emerge in basins across the monsoon sector. These results have implications for long-term infrastructure planning in the electricity sector.

The key finding of this work is that in ESM4.1, large-scale hydrological changes driven by warming reduce seasonal runoff significantly across a number of key basins for hydropower production in Brazil. In general, climate adaptation is difficult because of uncertainties in projections, but the monsoon delay is emerging as a robust climate change projection that warrants risk assessment and policy responses. The main policy goal in light of these projections is to ensure energy system security in Brazil amid competing demands such as climate change mitigation, reliability of supply, cost effectiveness, ecosystem conservation, and indigenous claims to land.

The first recommendation would be for the Brazilian government's Energy Research Office (EPE) to implement formal climate risk assessments. The EPE is charged with developing medium to long term plans for the energy sector to ensure its stability and security. In the current framework, EPE is not responsible for conducting climate risk assessment (Ruffato-Ferreira et al., 2017). Capacity expansion planning should account for potential rainfall scenarios based on climate science literature to avoid wasteful multi-billion-dollar investments in underperforming hydroelectric projects, especially in light of the additional risks to ecosystem health and indigenous communities. Climate change risk assessments might lead Brazil to reconsider Amazonian hydroelectric capacity expansion altogether, where flat conditions and environmental considerations would necessitate the development of drought-prone run-of-river plants. With their small reservoirs, run-of-river plants will be especially unreliable if exposed to seasonal shifts in precipitation and streamflow.

Another way to mitigate the climate risk to the energy system would be to appropriately price non-served energy. The non-served energy is the electricity demand that is not met by the system at a given time. It is priced in order to represent the social cost of electricity interruptions, and this price affects economic decisions about investing in new developments (Oren, 2000). Increasing the price of non-served en-

ergy in Brazil would better reflect the severe impacts of rolling blackouts, and would incentivize projects that complement existing resources and bolster system reliability.

While analysis of demand changes is beyond the scope of this paper, it is worth noting that demand changes may compound the electricity system vulnerability in Brazil. In particular, droughts can exacerbate temperature extremes, leading to spikes in electricity demand for air conditioning while simultaneously reducing streamflow and hydropower potential. The potential for compounding threats of heat waves and power shortages calls for further research. The results for the mean seasonality changes presented here show that in the river basins feeding the Santo Antonio, Belo Monte, Lajeado, and Teles Pires hydropower plants, runoff decreases significantly in austral summer, when demand is also highest. Expected increases in temperature and heat stress (e.g. Zhang et al., 2021), as well as general development trends, will likely cause demand to increase strongly, and potentially worsen gaps between supply and demand if Brazil remains reliant on hydropower.

From an operational standpoint, hydropower deployment could be improved by altering ONS' dispatch system. Currently, ONS deploys generators in order to minimize instantaneous costs. This fails to account for the impacts on water levels at dams and exacerbates waste in wet years and scarcity in dry seasons (Hunt et al., 2018). ONS could reduce some of the seasonal variability of hydropower production by considering optimal water levels at existing dams in its dispatch decisions. Of course, this strategy will be limited if run-of-river capacity expansion continues. Further, developing seasonal pumped storage facilities across a broader geographic range could reduce the volatility associated with hydropower. Seasonal pumped storage acts like a long-term battery, moving water uphill when water is ample and energy is cheap, and releasing it to generate electricity during the dry season. Broadening hydroelectric storage capacity across a broader geographic range can buffer drought risk and provide dispatchable, low-carbon power as variable renewable energy capac-

ity grows. The reservoirs of existing dams could serve as lower-reservoirs for pumped storage hydropower developments, to benefit from existing electrical and transmission capacity (Kelman and Harrison, 2019). The development of pumped storage would be limited to areas with favorable terrain (Kelman and Harrison, 2019). From the market perspective, a revision of the remuneration scheme to place value on ancillary services would make pumped hydropower storage projects more economically feasible (Kelman and Harrison, 2019).

Given the risk of shifting rainfall seasonality and increased aridity over the South American monsoon sector, Brazil's electricity system planning should focus on supporting diversification and complementarity. For example, solar farms can be designed to optimize output for a particular season, such as when hydropower production is expected to dip. Brazil's high insolation makes it a promising market for solar energy, and there is rush of solar expansion underway as developers seek to benefit from a renewable energy subsidy set to expire in March 2022 (Costa, 2021). Further policy incentives to encourage solar growth can mitigate the hydropower risk and reduce reliance on thermal generation.

One particular challenge will be to accommodate distributed solar generation within the centralized Brazilian electricity system. With Brazil's ample solar resources and growing demand, decentralized solar generation could flourish in coming years, presenting a major disruption to the centralized power system currently in place (Le Corre and coauthors, 2017). ANEEL issued resolution No. 687 in 2015 to instate a net metering program to lay the groundwork for broader use of distributed generation resources. However, solar PV systems remain expensive compared to other countries due to hefty tariffs and the variable-cost based pricing of the centralized grid electricity (Le Corre and coauthors, 2017). On the other hand, unlike in most countries, in Brazil the electricity bill is solely based on variable costs, which means zero charges when a unit's PV installation is meeting its demand.

How could Brazil foster its fledgling distributed solar generation program? By removing import taxes on solar PV materials, offering tax credits for installations, and revising its net metering rules to increase the credit limit for energy injected to the grid or even offering remuneration, Brazil could accelerate adoption of small-scale solar PV and relieve peak demand on its electricity system (Le Corre and coauthors, 2017). This would present challenges to existing utilities, who would lose payments. If EPE accounts for the rise of distributed generation along with these reforms in its research, they might determine that the proliferation of solar could eliminate the need for some hydropower development in sensitive ecosystems like the Amazon. In addition, depending on ANEEL's reforms and the extent of distributed solar uptake it might be necessary to invest in grid improvements to accommodate new congestion hotspots where excess solar energy is injected. Recovering these investment costs may require regulatory reform, since users with distributed solar power meet some of their own energy needs and therefore are not always paying for energy from the centralized system. By taking a role in net-metering installation or including a fixed-cost minimal payment on electricity bills, ANEEL can maximize system benefits. Taking a proactive approach to distributed solar generation will enable Brazil to maintain a sustainable business model.

Wind energy capacity expansion can also improve system resilience, and Brazil has enormous wind energy potential: continental wind resources are estimated at 143.5 GW and offshore resources in waters up to 50 meters deep exceed 1.2 TW (Pimenta and Assireu, 2015; Silva et al., 2016). Offshore winds in the north and northeast of Brazil exhibit strong seasonal complementarity with streamflow across the monsoon sector (Chade et al., 2015; Silva et al., 2016). Increased wind energy generation can reduce the reliance on hydroelectric generation and stabilize reservoir levels, improving system stability (Pimenta and Assireu, 2015). Solar and wind developments are promising not only for their complementarity but also as less capital

and labor-intensive projects with fewer environmental impacts than hydropower dams (Kelman and Harrison, 2019). Future work is needed to assess and mitigate the risk of shifting rainfall seasonality to electricity system reliability in Brazil. Investing in a diversified and seasonally complementary expansion of Brazil's renewable energy capacity will ensure a resilient and sustainable electricity sector.

# Chapter 6

# Conclusion

## 6.1 Summary

This dissertation focuses on building our physical understanding of monsoon seasonality. We do so by studying seasonal variations in the climate response to warming (Chapters 2, 5) as well as the impact of land surface properties (moisture, albedo), which on Earth vary seasonally and geographically, on the properties and mechanisms of monsoonal precipitation (Chapters 3, 4).

First, we examine the mechanisms of future drying over South America using a simple, uniform SST warming experiment in the GFDL atmospheric model AM4.1. While uniform SST warming is a robust aspect of the climate response to increased $CO_2$, the precipitation response to uniform warming is not well understood (Chadwick, 2016). Precipitation decreases substantially in the monsoon onset season, lending support to the projection that the dry season will become more severe over southern Amazonia with warming. Informed by a moist static energy budget analysis, we propose an explanation for the seasonally varying rainfall response to warming. The climatological MSE budget regulation, in particular the ratio of vertical to horizontal MSE advection terms ($V_{MSE}/H_{MSE}$), provides information about the character

of tropical atmospheric circulations. In summer over the monsoon sector, when the net column forcing is positive and the total circulation must export MSE from the column, the sign of $\mathrm{V}_{MSE}/\mathrm{H}_{MSE}$ reflects the sign of the gross moist stability, which is related to the shape of the ascent profile. For circulations in which the $\mathrm{V}_{MSE}/\mathrm{H}_{MSE}$ is positive but less than one, horizontal MSE advection plays a leading role in exporting column MSE. Such circulations are more prone to drying by the "upped-ante" mechanism first described by Chou and Neelin (2004), whereby the increase of horizontal MSE gradients with warming leads to enhanced damping of column MSE by the horizontal flow. Therefore, a place is vulnerable to drying if its climatological circulation satisfies $0 < V_{MSE}/\mathrm{H}_{MSE} < 1$ and the horizontal MSE gradients parallel to the horizontal inflow increase with warming. Due to different near-surface relative humidity in spring in fall, while both seasons satisfy the first criterion, only spring satisfies the second criterion and exhibits pronounced drying.

Next, motivated by the apparent importance of seasonally varying surface moisture in the monsoon response to warming, we employ a moist idealized modeling framework to discern the impact of land surface albedo and moisture conditions on monsoon dynamics. We find that a monsoon can emerge over a near-equatorial continent even when latent heat fluxes are disabled over land, though the strength and depth of convection, the precipitation generation mechanism, and the column energy budget are strongly influenced by the surface moisture availability. Considering the entire suite of experiments, we identify some key parameters governing the precipitation magnitude with all land moisture conditions. The simulated monsoon strength increases as the surface albedo decreases, the net column energy flux $\mathrm{F}_{net}$ increases, the near-surface MSE increases, and the near-surface MSE contrast between the monsoon sector and the tropical mean increases. These relationships hold across experiments and in some cases across seasons.

Then, we examine the processes underlying monsoonal precipitation on synoptic timescales in one of the idealized model experiments. We focus on understanding the atmospheric instability underlying storm development when the land surface is completely dry. The results lend support to the idea that inertial instability is a key driver of off-equatorial convergence and precipitation over the continent. The lower-tropospheric absolute vorticity contour $\eta = 0$ expands off the equator due to the large scale cross-equatorial pressure gradient induced by the low heat capacity of the land combined with the constraint on latent heat fluxes. On daily timescales, the position and strength of convection and precipitation coincides with the extent of the inertially unstable zone in the lower-troposphere. These findings have potential relevance for understanding monsoon onset following the dry season, when land surface moisture is limited and thermal gradients increase with insolation forcing.

The final project analyzes the potential implications of projected spring drying over the South American monsoon sector for the Brazilian electricity system. Hydropower is the basis of the Brazilian electricity system, contributing about 60 to 80% of national power generation in the last seven years. The ongoing development of additional run-of-river hydropower plants will increasingly link the Brazilian electricity system to instantaneous streamflow. We examine the hydrological response to warming in the moderate and high-emissions Shared Socioeconomic Pathway (SSP) scenarios in the latest coupled Earth System Model from the NOAA Geophysical Fluid Dynamics Laboratory (GFDL ESM4.1). The results indicate that even with mitigation efforts (SSP245), warming will drive reductions in precipitation in spring, with aridity increasing across the continent, especially in the west. Increasing water scarcity leads to decreases in soil moisture, transpiration, vegetation fraction, and near-surface relative humidity. The changes in monsoon seasonality also lead to significant runoff reductions in several basins where key hydroelectric plants are located. In the basin draining to the Santo Antonio Dam, a run-of-river hydropower

plant located in western Brazil, total runoff decreases by $\sim$ 30% in February, and the decreases in mean runoff are statistically significant in all four seasons by the end-of-century in the high emissions scenario. The changes in the monsoon represent a large-scale and systematic shift that could expose vulnerabilities in the Brazilian energy system. The work emphasizes the value of seasonal projections, which enable energy system planners to take advantage of seasonally complementary renewable energy alternatives. Offshore wind energy in the northeast of Brazil has the highest generation potential from late winter through early summer, making it an excellent candidate to complement hydrological seasonality and bolster Brazil's energy profile (Chade et al., 2015; Silva et al., 2016).

## 6.2 A model hierarchy approach

This dissertation utilizes a range of climate models to explore the causes and consequences of monsoon variability, from an idealized moist atmospheric model with a slab ocean, to a comprehensive atmospheric model with prescribed SSTs, to a fully coupled Earth System Model with interactive ocean dynamics and vegetation. These three models, all global in scale, vary in the sophistication of the atmospheric physics and the number of processes included, ranging from a model without clouds, topography or global continental geometry, to a model with all of these features as well as chemistry and carbon cycling (Maher et al., 2019). All three models capture key features of the South American monsoon, though they achieve varying degrees of realism (Figs. 2.1, 3.2, 5.2). The models are selected based on the questions of interest in each respective chapter. The work with the idealized model aims to explore physical relationships in order to build understanding of fundamental aspects of monsoon formation. Given modern orbital parameters and an isolated equatorial continent, under what conditions can a monsoon form? How do the continental conditions dictate the

spatial distribution and magnitude of rainfall, the circulation properties, the atmospheric energy budget, and the atmospheric instabilities underlying monsoonal storm formation? An idealized model allows one to systematically pursue these questions without facing the full complexity of the coupled land-atmospheric-ocean system. Setting aside cloud, ocean, or vegetation feedbacks, what are the basic processes at play? Can the results shed light on the monsoon behavior in a more complex model, or in observations?

An elegant model hierarchy distills the key components needed to capture a phenomenon of interest, and even enables one to discern cause and effect in well-designed experiments (Held, 2005; Hoskins, 1983; Maher et al., 2019). With the simpler models in the hierarchy one can perform mechanism denial experiments and test theories. Such research can build confidence, or raise crucial questions, about the realism and robustness of comprehensive coupled climate model projections. Most of the literature on monsoon dynamics is based on either highly idealized zonally symmetric configurations or the most realistic CMIP models. As reviewed in Chapter 1, great progress has been made in developing the basic theory for monsoons using zonally symmetric models configured as aquaplanets with dry or simplified moist atmospheres (e.g. Privé and Plumb, 2007a; Bordoni and Schneider, 2008). In terms of boundary conditions, some studies have implemented zonally symmetric or zonally confined continents; some impose perpetual solstice conditions rather than a seasonal cycle. This thesis utilizes an idealized moist model with realistic radiative transfer, a seasonal cycle, and an isolated continent with realistic geometry, because it occupies a rung on the hierarchy between the highly idealized and realistic touchstones that dominate the literature (Clark et al., 2018). The model is apt because it captures some of the essential features of monsoons: seasonality, zonal asymmetry, and moist physics. The basis of the model is that developed by Frierson et al. (2006), which has become a benchmark model in the field (e.g. O'Gorman and Schneider, 2008;

Levine and Schneider, 2011; Vallis et al., 2018). Following Clark et al. (2018), we elaborate the model by including a realistic radiative transfer scheme so that water vapor feedbacks are included, but retain elegance by excluding clouds and using simple convective and boundary layer parameterizations.

Throughout this dissertation we draw connections between the models of varying complexity. In Chapter 3, we find that some simple relationships governing the monsoon precipitation magnitude in the idealized model also hold in AM4, a significantly more elaborate and realistic model. Notably, precipitation increases with the contrast between monsoon-sector and tropical mean near-surface MSE across the idealized experiments, AM4 control and +2-K experiments, and throughout the seasonal cycle in both models. The precipitation seems to increase more sharply above this threshold in AM4 than in the idealized model. Interestingly, even when CQE conditions are broken in the dry land experiments, substantial precipitation does not occur until the monsoon-sector near-surface MSE exceeds the tropical mean value. The apparent generality of this relationship, even as the mechanisms initiating precipitation and the properties of convection differ, is striking and warrants further research.

For Chapter 5, our interest in future runoff changes calls for a higher spatial resolution (here, $\sim 1^\circ$ horizontal) and a faithful representation of the land processes involved in the rainfall-runoff transformation processes. Therefore, Chapter 5 utilizes the fully coupled Earth System Model ESM4.1, while drawing on the insights developed with the models lower in the hierarchy. A focus on the seasonal cycle allows us to draw on a robust aspect of the future climate projection (a drier monsoon onset season), and to propose solutions that account for the seasonality of both renewable energy sources and electricity demand. While interactive vegetation amplifies the spring drying response to increased $CO_2$ over the South American monsoon sector, the basic response can be understood in an atmospheric model in which SSTs are increased uniformly by 2-K (Chapter 2).

## 6.3 Future research directions

A theme of this thesis is the importance of land-atmosphere coupling for determining monsoon seasonality. In Chapter 2 we show that while fall and spring are in similar regimes in terms of their monsoon-sector mean MSE budget regulation, the precipitation response to warming differs in the two seasons, with drying in spring and negligible change in fall. We attribute this to the differing availability of surface moisture preceding and following the rainy season, which leads to different surface MSE gradient changes with warming. In Chapters 3 and 4, the land surface properties impact the monsoonal intensity, spatial distribution, energy budget regulation, and precipitation generation processes. In Chapter 5, water scarcity and its effect on plants reduces evapotranspiration over the monsoon sector. Further, the evapotranspiration, basin geometry, and vegetation and soil properties result in a phase-lag of total runoff relative to precipitation in Amazonia, so that changes in precipitation affect streamflow and hydropower production in other seasons. The work illustrates the importance of studying the combined responses of precipitation and evaporation to understand how regional water supply will be affected by climate change (Konapala et al., 2020).

A rich avenue for future study will be the role of atmosphere-*ocean* coupling in monsoon dynamics. The strong influence of SSTs on the precipitation distribution is well appreciated (e.g. Lindzen and Nigam, 1987; Giannini et al., 2003; Lu and Delworth, 2005). Ocean heat transport can impact surface thermodynamic gradients and thus the atmospheric circulation, in addition to its impact on the atmospheric energy budget. In this thesis, the AM4 model uses prescribed SSTs, and the idealized model is configured with a thermodynamic slab ocean. While ESM4.1 is coupled to a dynamic ocean, we do not consider the impact of ocean heat transport on the monsoon response to forcing. Chou et al. (2001) demonstrate that the inclusion of ocean transport intensifies monsoon precipitation by cooling the tropical ocean,

making land more thermodynamically favorable to convection. By similar means, in an idealized model the cross-equatorial ocean heat transport (OHT) induced by monsoonal winds intensfies the monsoon circulation (Lutsko et al., 2019). At the same time, the inclusion of interactive ocean dynamics weakens the cross-equatorial atmospheric circulation since the requisite atmospheric heat transport decreases with the enhanced OHT (Lutsko et al., 2019). Such work raises interesting questions about the relationship of the monsoon to the zonal mean circulation, as well as the importance of feedbacks between near-surface winds and Ekman transport in monsoon regions. It will be fruitful to pursue further research along these lines, as the the role of ocean dynamics in monsoon formation has generally been under-explored.

In Chapter 3, the bottom-heavy monsoonal ascent profiles in the dry land suite resemble the observed convection in regions with strong SST gradients, like the East Pacific ITCZ. These regions of negative gross moist stability deviate from the canonical picture of tropical precipitation in which deep moist convection contributes to column MSE export (Neelin and Held, 1987). Further, these dry-land monsoons deviate from convective quasi-equilibrium conditions. I am interested in analyzing the climate response to increased atmospheric $CO_2$ in these idealized moist model configurations. This will elucidate how the climatological properties of convection impact the precipitation response to warming, and allow us to test how well the conditions for drying proposed in Chapter 2 guide predictions.

Chapter 4 presents a preliminary study of the synoptic variability during a single month of the monsoon season over a dry continent. While there are hundreds of papers analyzing the seasonal or climatological behavior of monsoon circulations, relatively few studies look at monsoon precipitation generation mechanisms on shorter timescales. Understanding the synoptic dynamics will shed light on intraseasonal variability (e.g. the active-break sequence), precipitation extremes, and will ultimately contribute to improved forecasts.

Finally, it will be valuable to make more contact with observations in the future, to determine the relevance of the insights developed in a modeling context for real monsoons, and to constrain the comprehensive models used to simulate past and future monsoon systems. In this way, step by step, we can build understanding and appreciation of our bewildering, intricate, and life-giving climate system.

# Bibliography


Adam, O., T. Bischoff, and T. Schneider, 2016: Seasonal and interannual variations of the energy flux equator and itcz. part ii: Zonally varying shifts of the itcz. *Journal of Climate*, **29 (20)**, 7281–7293, doi:10.1175/JCLI-D-15-0710.1.

Adames, Á. F., and Y. Ming, 2018: Interactions between water vapor and potential vorticity in synoptic-scale monsoonal disturbances: Moisture vortex instability. *Journal of the Atmospheric Sciences*, **75 (6)**, 2083–2106.

Adler, R., and Coauthors, 2016: The new version 2.3 of the global precipitation climatology project (gpcp) monthly analysis product. *University of Maryland, April*, 1072–1084.

Allen, M. R., and W. J. Ingram, 2002: Constraints on future changes in climate and the hydrologic cycle. *Nature*, **419 (6903)**, 224–232.

An, Z., and Coauthors, 2015: Global monsoon dynamics and climate change. *Annual Review of Earth and Planetary Sciences*, **43**, 29–77.

Arias, M. E., F. Farinosi, E. Lee, A. Livino, J. Briscoe, and P. R. Moorcroft, 2020: Impacts of climate change and deforestation on hydropower planning in the brazilian amazon. *Nature Sustainability*, **3 (6)**, 430–436.

Back, L., and C. Bretherton, 2006: Geographic variability in the export of moist static energy and vertical motion profiles in the tropical pacific. *Geophysical research letters*, **33 (17)**.

Back, L. E., and C. S. Bretherton, 2009: A simple model of climatological rainfall and vertical motion patterns over the tropical oceans. *Journal of Climate*, **22 (23)**, 6477–6497.

Barroso, L. A., J. M. Bressane, L. M. Thomé, M. Junqueira, I. Camargo, G. Oliveira, S. Binato, and M. V. Pereira, 2004: Transmission structure in Brazil: organization, evaluation and trends. *IEEE Power Engineering Society General Meeting, 2004.*, IEEE, 1301–1306.

Berg, A., B. Lintner, K. Findell, and A. Giannini, 2017: Soil moisture influence on seasonality and large-scale circulation in simulations of the west african monsoon. *Journal of Climate*, **30 (7)**, 2295–2317.

Berg, A., B. Lintner, K. Findell, S. Seneviratne, and B. van den Hurk et al., 2015: Interannual coupling between summertime surface temperature and precipitation over land: Processes and implications for climate change. *J. Climate*, **28**, 1308–1328.

Berg, A., and Coauthors, 2016: Land–atmosphere feedbacks amplify aridity increase over land under global warming. *Nature Climate Change*, **6 (9)**, 869–874, doi:10.1038/nclimate3029, URL https://www.nature.com/articles/nclimate3029, number: 9 Publisher: Nature Publishing Group.

Biasutti, M., A. Sobel, and S. Camargo, 2009: The role of the sahara low in summertime sahel rainfall variability and change in the cmip3 models. *J. Climate*, **22**, 5755–5771.

Biasutti, M., and A. H. Sobel, 2009: Delayed sahel rainfall and global seasonal cycle in a warmer climate. *Geophysical Research Letters*, **36 (23)**.

Biasutti, M., and Coauthors, 2018: Global energetics and local physics as drivers of past, present and future monsoons. *Nature Geoscience*, **11 (6)**, 392.

Bischoff, T., and T. Schneider, 2014: Energetic constraints on the position of the intertropical convergence zone. *Journal of Climate*, **27 (13)**, 4937–4951.

Boers, N., N. Marwan, H. M. Barbosa, and J. Kurths, 2017: A deforestation-induced tipping point for the south american monsoon system. *Scientific reports*, **7 (1)**, 1–9.

Boisier, J., P. Ciais, A. Ducharne, and M. Guimberteau, 2015: Projected strengthening of amazonian dry season by constrained climate model simulations. *Nature Climate Change*, **5**, 656–660, doi:10.1038/NCLIMATE2658.

Bollasina, M. A., and Y. Ming, 2013: The role of land-surface processes in modulating the indian monsoon annual cycle. *Climate dynamics*, **41 (9-10)**, 2497–2509.

Boos, W., and R. Korty, 2016: Regional energy budget control of the intertropical convergence zone and application to mid-holocene rainfall. *Nature Geoscience*, **9**, 892–897.

Boos, W. R., and J. V. Hurley, 2013: Thermodynamic bias in the multimodel mean boreal summer monsoon. *Journal of Climate*, **26 (7)**, 2279–2287.

Boos, W. R., J. V. Hurley, and V. S. Murthy, 2015: Adiabatic westward drift of Indian monsoon depressions. *Quarterly Journal of the Royal Meteorological Society*, **141 (689)**, 1035–1048, doi:https://doi.org/10.1002/qj.2454.

Boos, W. R., and T. Storelvmo, 2016: Near-linear response of mean monsoon strength to a broad range of radiative forcings. *Proceedings of the National Academy of Sciences*, **113 (6)**, 1510–1515.

Bordoni, S., and T. Schneider, 2008: Monsoons as eddy-mediated regime transitions of the tropical overturning circulation. *Nature Geoscience*, **1 (8)**, 515–519.

Bretherton, C. S., P. N. Blossey, and M. E. Peters, 2006: Interpretation of simple and cloud-resolving simulations of moist convection–radiation interaction with a mock-walker circulation. *Theoretical and Computational Fluid Dynamics*, **20 (5-6)**, 421–442.

Byrne, M., and P. O'Gorman, 2016: Understanding decreases in land relative humidity with global warming: Conceptual model and gcm simulations. *Journal of Climate*, **29 (24)**, 9045–9061, doi:10.1175/JCLI-D-16-0351.1.

Byrne, M. P., and P. A. O'Gorman, 2013: Land–ocean warming contrast over a wide range of climates: convective quasi-equilibrium theory and idealized simulations. *Journal of Climate*, **26 (12)**, 4000–4016.

Byrne, M. P., and P. A. O'Gorman, 2015: The response of precipitation minus evapotranspiration to climate warming: Why the "wet-get-wetter, dry-get-drier" scaling does not hold over land. *Journal of Climate*, **28 (20)**, 8078–8092, doi: 10.1175/JCLI-D-15-0369.1.

Cao, L., G. Bala, K. Caldeira, R. Nemani, and G. Ban-Weiss, 2010: Importance of carbon dioxide physiological forcing to future climate change. *Proceedings of the National Academy of Sciences*, **107 (21)**, 9513–9518, doi:10.1073/pnas.0913000107.

Cess, R. D., and Coauthors, 1990: Intercomparison and interpretation of climate feedback processes in 19 atmospheric general circulation models. *J. Geophys. Res*, **95 (D10)**, 16 601– 16 615, doi:10.1029/JD095iD10p16601.

Chade, J. F., R. C. Zambon, I. L. Sauer, and W. W. Yeh, 2015: Increasing share of wind power and its complementarity with hydropower in the brazilian interconnected electricity system. *World Environmental and Water Resources Congress 2015*, 2163–2172.

Chadwick, R., 2016: Which aspects of co2 forcing and sst warming cause most uncertainty in projections of tropical rainfall change over land and ocean? *Journal of Climate*, **29 (7)**, 2493–2509.

Chao, W. C., and B. Chen, 2001: The origin of monsoons. *Journal of the Atmospheric Sciences*, **58 (22)**, 3497–3507.

Charney, J. G., 1963: A note on large-scale motions in the tropics. *Journal of the Atmospheric Sciences*, **20 (6)**, 607–609.

Charney, J. G., 1975: Dynamics of deserts and drought in the sahel. *Quarterly Journal of the Royal Meteorological Society*, **101 (428)**, 193–202.

Charney, J. G., and M. Stern, 1962: On the stability of internal baroclinic jets in a rotating atmosphere. *Journal of the Atmospheric Sciences*, **19 (2)**, 159–172.

Chou, C., and C.-W. Lan, 2012: Changes in the annual range of precipitation under global warming. *Journal of Climate*, **25 (1)**, 222–235.

Chou, C., and J. D. Neelin, 2001: Mechanisms limiting the southward extent of the south american summer monsoon. *Geophysical research letters*, **28 (12)**, 2433–2436.

Chou, C., and J. D. Neelin, 2004: Mechanisms of global warming impacts on regional tropical precipitation. *Journal of Climate*, **17 (13)**, 2688–2701.

Chou, C., J. D. Neelin, and H. Su, 2001: Ocean-atmosphere-land feedbacks in an idealized monsoon. *Quarterly Journal of the Royal Meteorological Society*, **127 (576)**, 1869–1891.

Clark, S. K., Y. Ming, and Á. F. Adames, 2020: Monsoon low pressure system–like variability in an idealized moist model. *Journal of Climate*, **33 (6)**, 2051–2074.

Clark, S. K., Y. Ming, I. M. Held, and P. J. Phillipps, 2018: The role of the water vapor feedback in the itcz response to hemispherically asymmetric forcings. *Journal of Climate*, **31 (9)**, 3659–3678.

Cohen, N. Y., and W. R. Boos, 2016: Perspectives on Moist Baroclinic Instability: Implications for the Growth of Monsoon Depressions. *Journal of the Atmospheric Sciences*, **73 (4)**, 1767–1788, doi:10.1175/JAS-D-15-0254.1.

Collini, E. A., E. H. Berbery, V. R. Barros, and M. E. Pyle, 2008: How does soil moisture influence the early stages of the south american monsoon? *Journal of Climate*, **21 (2)**, 195–213.

Cook, B. I., J. S. Mankin, K. Marvel, A. P. Williams, J. E. Smerdon, and K. J. Anchukaitis, 2020: Twenty-First Century Drought Projections in the CMIP6 Forcing Scenarios. *Earth's Future*, **8 (6)**, e2019EF001 461, doi:https://doi.org/10.1029/2019EF001461.

Cook, K. H., 2015: Role of inertial instability in the west african monsoon jump. *Journal of Geophysical Research: Atmospheres*, **120 (8)**, 3085–3102.

Cook, K. H., and A. Gnanadesikan, 1991: Effects of saturated and dry land surfaces on the tropical circulation and precipitation in a general circulation model. *Journal of climate*, **4 (9)**, 873–889.

Costa, L., 2021: Brazil sees solar boom ahead of cut in subsidies for new projects. *Reuters*, URL https://www.reuters.com/business/energy/brazil-sees-solar-boom-ahead-cut-subsidies-new-projects-2021-04-20/.

de Souza Dias, V., M. Pereira da Luz, G. M. Medero, and D. Tarley Ferreira Nascimento, 2018: An overview of hydropower reservoirs in brazil: Current situation, future perspectives and impacts of climate change. *Water*, **10 (5)**, 592.

Delworth, T. L., and S. Manabe, 1988: The influence of potential evaporation on the variabilities of simulated soil wetness and climate. *Journal of Climate*, **1 (5)**, 523–547.

Diaz, M., and W. R. Boos, 2019a: Barotropic growth of monsoon depressions. *Quarterly Journal of the Royal Meteorological Society*, **145 (719)**, 824–844, doi: https://doi.org/10.1002/qj.3467.

Diaz, M., and W. R. Boos, 2019b: Monsoon depression amplification by moist barotropic instability in a vertically sheared environment. *Quarterly Journal of the Royal Meteorological Society*, **145 (723)**, 2666–2684.

Diaz, M., and W. R. Boos, 2021: Evolution of idealized vortices in monsoon-like shears: Application to monsoon depressions. *Journal of the Atmospheric Sciences*, **78 (4)**, 1207–1225.

Dirmeyer, P. A., C. A. Schlosser, and K. L. Brubaker, 2009: Precipitation, recycling, and land memory: An integrated analysis. *Journal of Hydrometeorology*, **10 (1)**, 278–288.

Dunne, J. P., and Coauthors, 2020: The GFDL Earth System Model Version 4.1 (GFDL-ESM 4.1): Overall Coupled Model Description and Simulation Characteristics. *Journal of Advances in Modeling Earth Systems*, **12 (11)**, e2019MS002 015, doi:https://doi.org/10.1029/2019MS002015, URL https://agupubs.onlinelibrary.wiley.com/doi/abs/10.1029/2019MS002015, _eprint: https://agupubs.onlinelibrary.wiley.com/doi/pdf/10.1029/2019MS002015.

Dunne, T., 1978: Field studies of hillsope flow processes. *Hillslope hydrology*, 227–293.

Dwyer, J. G., M. Biasutti, and A. H. Sobel, 2014: The effect of greenhouse gas–induced changes in sst on the annual cycle of zonal mean tropical precipitation. *Journal of Climate*, **27 (12)**, 4544–4565.

Emanuel, K. A., 1995: On thermally direct circulations in moist atmospheres. *Journal of the atmospheric sciences*, **52 (9)**, 1529–1534.

Emanuel, K. A. J. D. N., and C. S. Bretherton, 1994: On large-scale circulations in convecting atmospheres. *Quarterly Journal of the Royal Meteorological Society*, **120 (519)**, 1111–1143.

Estoque, R. C., M. Ooba, T. Togawa, and Y. Hijioka, 2020: Projected land-use changes in the Shared Socioeconomic Pathways: Insights and implications. *Ambio*, **49 (12)**, 1972–1981, doi:10.1007/s13280-020-01338-4, URL https://doi.org/10.1007/s13280-020-01338-4.

Falcetta, F. A., R. C. Zambon, and W. W. Yeh, 2014: Evolution of storage capacity in the brazilian hydropower system. *World Environmental and Water Resources Congress 2014*, 1916–1925.

Ferranti, L., J. Slingo, T. Palmer, and B. Hoskins, 1999: The effect of land-surface feedbacks on the monsoon circulation. *Quarterly Journal of the Royal Meteorological Society*, **125 (557)**, 1527–1550.

Findell, K. L., P. W. Keys, R. J. v. d. Ent, B. R. Lintner, A. Berg, and J. P. Krasting, 2019: Rising Temperatures Increase Importance of Oceanic Evaporation as a Source for Continental Precipitation. *Journal of Climate*, **32 (22)**, 7713–7726, doi:10.1175/JCLI-D-19-0145.1.

Frierson, D., 2007: The dynamics of idealized convection schemes and their effect on the zonally averaged tropical circulation. *Journal of the Atmos. Sciences*, **64**, 1959–1975.

Frierson, D. M., I. M. Held, and P. Zurita-Gotor, 2006: A gray-radiation aquaplanet moist gcm. part i: Static stability and eddy scale. *Journal of the atmospheric sciences*, **63 (10)**, 2548–2566.

Fu, R., and W. Li, 2004: The influence of the land surface on the transition from dry to wet season in amazonia. *Theoretical and Applied Climatology*, **78 (1)**, 97–110, doi:10.1007/s00704-004-0046-7.

Fu, R., B. Zhu, and R. E. Dickinson, 1999: How do atmosphere and land surface influence seasonal changes of convection in the tropical amazon? *Journal of Climate*, **12 (5)**, 1306–1321.

Fu, R., and Coauthors, 2013: Increased dry-season length over southern amazonia in recent decades and its implication for future climate projection. *Proceedings of the National Academy of Sciences*, 201302584, doi:10.1073/pnas.1302584110.

Gadgil, S., 2018: The monsoon system: Land–sea breeze or the itcz? *Journal of Earth System Science*, **127 (1)**, 1–29.

Gadgil, S., P. S. Rao, and K. N. Rao, 2002: Use of climate information for farm-level decision making: rainfed groundnut in southern india. *Agricultural Systems*, **74 (3)**, 431–457.

Garreaud, R., and P. Aceituno, 2001: Interannual rainfall variability over the south american altiplano. *Journal of climate*, **14 (12)**, 2779–2789.

Geen, R., S. Bordoni, D. S. Battisti, and K. Hui, 2020: Monsoons, itczs and the concept of the global monsoon. *Reviews of Geophysics*, e2020RG000700.

Geen, R., F. Lambert, and G. Vallis, 2018: Regime change behavior during asian monsoon onset. *Journal of Climate*, **31 (8)**, 3327–3348.

Giannini, A., R. Saravanan, and P. Chang, 2003: Oceanic forcing of sahel rainfall on interannual to interdecadal time scales. *Science*, **302 (5647)**, 1027–1030.

Gill, A. E., 1980: Some simple solutions for heat-induced tropical circulation. *Quarterly Journal of the Royal Meteorological Society*, **106 (449)**, 447–462.

Halley, E., 1687: An historical account of the trade winds, and monsoons, observable in the seas between and near the tropicks, with an attempt to assign the physical cause of the said winds. *Philosophical Transactions of the Royal Society of London*, **16 (183)**, 153–168.

Harrop, B. E., J. Lu, and L. R. Leung, 2019: Sub-cloud moist entropy curvature as a predictor for changes in the seasonal cycle of tropical precipitation. *Climate Dynamics*, **53 (5)**, 3463–3479.

He, J., B. J. Soden, and B. Kirtman, 2014: The robustness of the atmospheric circulation and precipitation response to future anthropogenic surface warming. *Geophysical Research Letters*, **41 (7)**, 2614–2622.

Heaviside, C., and A. Czaja, 2013: Deconstructing the hadley cell heat transport. *Q.J.R. Meteorol. Soc.*, **139**, 2181–2189, doi:10.1002/qj.2085.

Held, I., T. Delworth, J. Lu, K. Findell, and T. Knutson, 2005: Simulation of sahel drought in the 20th and 21st centuries. *PNAS*, **102**, 17 891–17 896.

Held, I. M., 2005: The gap between simulation and understanding in climate modeling. *Bulletin of the American Meteorological Society*, **86 (11)**, 1609–1614.

Held, I. M., 2019: 100 years of progress in understanding the general circulation of the atmosphere. *Meteorological Monographs*, **59**, 6–1.

Held, I. M., and M. J. Suarez, 1994: A proposal for the intercomparison of the dynamical cores of atmospheric general circulation models. *Bulletin of the American Meteorological society*, **75 (10)**, 1825–1830.

Hill, S., Y. Ming, and I. Held, 2015: Mechanisms of forced tropical meridional energy flux change. *Journal of Climate*, **28**, 1725–1742.

Hill, S. A., 2019: Theories for past and future monsoon rainfall changes. *Journal of Climate*, **5 (3)**, 160–171.

Hill, S. A., Y. Ming, I. M. Held, and M. Zhao, 2017: A moist static energy budget–based analysis of the sahel rainfall response to uniform oceanic warming. *Journal of Climate*, **30 (15)**, 5637–5660.

Holton, J., 1992: *An introduction to dynamic meteorology*, Vol. 48. 1–497 pp.

Hoskins, B., 1983: Dynamical processes in the atmosphere and the use of models. *Quarterly Journal of the Royal Meteorological Society*, **109 (459)**, 1–21.

Hsieh, J., and K. H. Cook, 2005: Generation of african easterly wave disturbances: Relationship to the african easterly jet. *Mon. Wea. Rev.*, **133**, 1311–1327.

Huang, P., S.-P. Xie, K. Hu, G. Huang, and R. Huang, 2013: Patterns of the seasonal response of tropical rainfall to global warming. *Nature Geoscience*, **6 (5)**, 357.

Hunt, J. D., D. Stilpen, and M. A. V. de Freitas, 2018: A review of the causes, impacts and solutions for electricity supply crises in brazil. *Renewable and Sustainable Energy Reviews*, **88**, 208–222.

Hurley, J., and W. Boos, 2013: Interannual variability of monsoon precipitation and local subcloud equivalent potential temperature. *Journal of Climate*, **26 (23)**, 9507–9527.

Joetzjer, E., H. Douville, C. Delire, and P. Ciais, 2013: Present-day and future amazonian precipitation in global climate models: Cmip5 versus cmip3. *Climate Dynamics*, **41 (11)**, 2921–2936.

Jones, C., and L. M. Carvalho, 2013: Climate change in the south american monsoon system: present climate and cmip5 projections. *Journal of Climate*, **26 (17)**, 6660–6678.

Joshi, M. M., J. M. Gregory, M. J. Webb, D. M. H. Sexton, and T. C. Johns, 2008: Mechanisms for the land/sea warming contrast exhibited by simulations of climate change. *Climate Dynamics*, **30 (5)**, 455–465, URL https://doi.org/10.1007/s00382-007-0306-1.

Kang, S., I. Held, D. Friersona, and M. Zhao, 2008: The response of the itcz to extratropical thermal forcing: Idealized slab-ocean experiments with a gcm. *Journal of Climate*, **21**, 3521–3532.

Kelman, R., and D. L. Harrison, 2019: Integrating Renewables with Pumped Hydro Storage in Brazil: a Case Study, URL https://hal.archives-ouvertes.fr/hal-02145006.

Kent, C., R. Chadwick, and D. Rowell, 2015: Understanding uncertainties in future projections of seasonal tropical precipitation. *Journal of Climate*, **28 (11)**, 4390–4413.

Kintisch, E., 2015: Amazon rainforest ability to soak up carbon dioxide is falling. *Science Magazine*, doi:10.1126/science.aab0336.

Kodama, Y., 1992: Large-scale common features of subtropical precipitation zones (the baiu frontal zone, the spcz, and the sacz) part i: Characteristics of subtropical frontal zones. *Journal of the Meteorological Society of Japan. Ser. II*, **70 (4)**, 813–836.

Kodama, Y.-M., 1993: Large-scale common features of sub-tropical convergence zones (the baiu frontal zone, the spcz, and the sacz) part ii: conditions of the circulations for generating the stczs. *Journal of the Meteorological Society of Japan. Ser. II*, **71 (5)**, 581–610.

Konapala, G., A. K. Mishra, Y. Wada, and M. E. Mann, 2020: Climate change will affect global water availability through compounding changes in seasonal precipitation and evaporation. *Nature Communications*, **11 (1)**, 3044, doi:10.1038/s41467-020-16757-w.

Koster, R. D., and S. P. P. Mahanama, 2012: Land Surface Controls on Hydroclimatic Means and Variability. *Journal of Hydrometeorology*, **13 (5)**, 1604–1620, doi:10.1175/JHM-D-12-050.1.

Koster, R. D., and M. J. Suarez, 1995: Relative contributions of land and ocean processes to precipitation variability. *Journal of Geophysical Research: Atmospheres*, **100 (D7)**, 13 775–13 790.

Koster, R. D., and Coauthors, 2004: Regions of strong coupling between soil moisture and precipitation. *Science*, **305 (5687)**, 1138–1140.

Krishnakumar, V., and K. M. Lau, 1998: Possible Role of Symmetric Instability in the Onset and Abrupt Transition of the Asian Monsoon. *Journal of the Meteorological Society of Japan. Ser. II*, **76 (3)**, 363–383, doi:10.2151/jmsj1965.76.3_363.

Lau, W. K.-M., H.-T. Wu, and K.-M. Kim, 2013: A canonical response of precipitation characteristics to global warming from cmip5 models. *Geophysical Research Letters*, **40 (12)**, 3163–3169.

Le Corre, J., and coauthors, 2017: Disruption Coming to Your Home: Decentralized Solar Generation in Brazil. Tech. rep., The Boston Consulting Group.

Lee, J.-Y., and B. Wang, 2014: Future change of global monsoon in the cmip5. *Climate Dynamics*, **42 (1-2)**, 101–119.

Leuning, R., 1995: A critical appraisal of a combined stomatal-photosynthesis model for c3 plants. *Plant, Cell & Environment*, **18 (4)**, 339–355.

Levine, X. J., and W. R. Boos, 2017: Land surface albedo bias in climate models and its association with tropical rainfall. *Geophysical Research Letters*, **44 (12)**, 6363–6372.

Levine, X. J., and T. Schneider, 2011: Response of the hadley circulation to climate change in an aquaplanet gcm coupled to a simple representation of ocean heat transport. *Journal of the Atmospheric Sciences*, **68 (4)**, 769–783.

Li, W., R. Fu, and R. E. Dickinson, 2006: Rainfall and its seasonality over the amazon in the 21st century as assessed by the coupled models for the ipcc ar4. *Journal of Geophysical Research: Atmospheres*, **111 (D2)**.

Lieberman, R., J. France, D. Ortland, and S. Eckermann, 2021: The role of inertial instability in cross-hemispheric coupling. *Journal of the Atmospheric Sciences*.

Lindzen, R. S., and S. Nigam, 1987: On the role of sea surface temperature gradients in forcing low-level winds and convergence in the tropics. *Journal of the Atmospheric Sciences*, **44 (17)**, 2418–2436.

Lu, J., and T. L. Delworth, 2005: Oceanic forcing of the late 20th century sahel drought. *Geophysical Research Letters*, **32 (22)**.

Lutsko, N. J., J. Marshall, and B. Green, 2019: Modulation of monsoon circulations by cross-equatorial ocean heat transport. *Journal of Climate*, **32 (12)**, 3471–3485.

Maher, P., and Coauthors, 2019: Model hierarchies for understanding atmospheric circulation. *Reviews of Geophysics*, **57 (2)**, 250–280.

Manabe, S., 1969: Climate and the ocean circulation: I. the atmospheric circulation and the hydrology of the earth's surface. *Monthly Weather Review*, **97 (11)**, 739–774.

Marengo, J. A., and M. Bernasconi, 2015: Regional differences in aridity/drought conditions over northeast brazil: present state and future projections. *Climatic Change*, **129 (1-2)**, 103–115, doi:https://doi.org/10.1007/s10584-014-1310-1.

Maroon, E. A., and D. M. Frierson, 2016: The impact of a continent's longitudinal extent on tropical precipitation. *Geophysical Research Letters*, **43 (22)**, 11–921.

Middleton, N., and D. Thomas, 1997: *World atlas of desertification.. ed. 2*. Arnold, Hodder Headline, PLC.

Milly, P. C. D., and K. A. Dunne, 2016a: Potential evapotranspiration and continental drying. *Nature Climate Change*, **6 (10)**, 946–949, doi:10.1038/nclimate3046.

Milly, P. C. D., and K. A. Dunne, 2016b: Potential evapotranspiration and continental drying. *Nature Climate Change*, **6 (10)**, 946–949, doi:10.1038/nclimate3046, URL http://www.nature.com/articles/nclimate3046.

Muller, C., and P. O'Gorman, 2011: An energetic perspective on the regional response of precipitation to climate change. *Nature Climate Change*, **1**, 266–271, doi:10.1038/NCLIMATE1169.

Natarov, A., and K. J. Richards, 2015: Persistent presence of small vertical scale velocity features during three-dimensional equilibration of equatorial inertial instability. *Physics of Fluids*, **27 (8)**, 084 109.

Neelin, D., and I. Held, 1987: Modeling tropical convergence based on the moist static energy budget. *Mon. Wea. Rev.*, **115**, 3–12.

Neelin, J., C. Chou, and H. Su, 2003: Tropical drought regions in global warming and el niño teleconnections. *Geophysical Research Letters*, **30 (24)**.

Neelin, J. D., 2007: Moist dynamics of tropical convection zones in monsoons, teleconnections, and global warming. Princeton University Press, 267–301 pp.

Nie, J., W. R. Boos, and Z. Kuang, 2010: Observational evaluation of a convective quasi-equilibrium view of monsoons. *Journal of Climate*, **23 (16)**, 4416–4428.

Nieto Ferreira, R., and W. C. Chao, 2013: Aqua-planet simulations of the formation of the south atlantic convergence zone. *International journal of climatology*, **33 (3)**, 615–628.

Norris, J., G. Chen, and J. D. Neelin, 2019: Thermodynamic versus dynamic controls on extreme precipitation in a warming climate from the community earth system model large ensemble. *Journal of Climate*, **32 (4)**, 1025–1045.

Oren, S. S., 2000: Capacity Payments and Supply Adequacy in Competitive Electricity Markets. *Sepope, May*, 8.

O'Gorman, P. A., and T. Schneider, 2008: The hydrological cycle over a wide range of climates simulated with an idealized gcm. *Journal of Climate*, **21 (15)**, 3815–3832.

O'Neill, B. C., and Coauthors, 2017: The roads ahead: Narratives for shared socioeconomic pathways describing world futures in the 21st century. *Global Environmental Change*, **42**, 169–180, doi:10.1016/j.gloenvcha.2015.01.004.

Paynter, D., and V. Ramaswamy, 2014: Investigating the impact of the shortwave water vapor continuum upon climate simulations using gfdl global models. *Journal of Geophysical Research: Atmospheres*, **119 (18)**, 10–720.

Pielke, R. A., R. Avissar, M. Raupach, A. J. Dolman, X. Zeng, and A. S. Denning, 1998: Interactions between the atmosphere and terrestrial ecosystems: influence on weather and climate. *Global change biology*, **4 (5)**, 461–475.

Pietschnig, M., F. Lambert, M. Saint-Lu, and G. Vallis, 2019: The presence of africa and limited soil moisture contribute to future drying of south america. *Geophysical Research Letters*, **46 (21)**, 12 445–12 453.

Pimenta, F. M., and A. T. Assireu, 2015: Simulating reservoir storage for a wind-hydro hydrid system. *Renewable Energy*, **76**, 757–767, doi:10.1016/j.renene.2014.11.047.

Plumb, R. A., and A. Y. Hou, 1992: The response of a zonally symmetric atmosphere to subtropical thermal forcing: Threshold behavior. *Journal of the atmospheric sciences*, **49 (19)**, 1790–1799.

Privé, N. C., and R. A. Plumb, 2007a: Monsoon dynamics with interactive forcing. part i: Axisymmetric studies. *Journal of the atmospheric sciences*, **64 (5)**, 1417–1430.

Privé, N. C., and R. A. Plumb, 2007b: Monsoon dynamics with interactive forcing. part ii: Impact of eddies and asymmetric geometries. *Journal of the atmospheric sciences*, **64 (5)**, 1431–1442.

Purves, D. W., J. W. Lichstein, N. Strigul, and S. W. Pacala, 2008: Predicting and understanding forest dynamics using a simple tractable model. *Proceedings of the National Academy of Sciences*, **105 (44)**, 17 018–17 022, doi:10.1073/pnas.0807754105.

Randall, D., 2012: Inertial stability and instability.

Rayleigh, L., 1917: On the dynamics of revolving fluids. *Proceedings of the Royal Society of London. Series A, Containing Papers of a Mathematical and Physical Character*, **93 (648)**, 148–154.

Ritchie, H., and M. Roser, 2020: Energy. *Our World in Data*, https://ourworldindata.org/energy.

Rossow, W. B., A. Mekonnen, C. Pearl, and W. Goncalves, 2013: Tropical precipitation extremes. *Journal of Climate*, **26 (4)**, 1457–1466.

Ruffato-Ferreira, V., R. da Costa Barreto, A. O. Júnior, W. L. Silva, D. de Berrêdo Viana, J. A. S. do Nascimento, and M. A. V. de Freitas, 2017: A foundation for the strategic long-term planning of the renewable energy sector in brazil: Hydroelectricity and wind energy in the face of climate change scenarios. *Renewable and Sustainable Energy Reviews*, **72**, 1124–1137.

Sakaguchi, K., L. Leung, C. D. Burleyson, H. Xiao, and H. Wan, 2018: Role of troposphere-convection-land coupling in the southwestern amazon precipitation bias of the community earth system model version 1 (cesm1). *Journal of Geophysical Research: Atmospheres*, **123 (16)**, 8374–8399.

Sánchez, A., E. Torres, and R. d. A. Kalid, 2015: Renewable energy generation for the rural electrification of isolated communities in the amazon region. *Renewable and Sustainable Energy Reviews*, **49**, 278–290.

Schneider, T., T. Bischoff, and G. Huag, 2014: Migrations and dynamics of the intertropical convergence zone. *Nature Review*, **513**, 45–53.

Schultz, D. M., and P. N. Schumacher, 1999: The Use and Misuse of Conditional Symmetric Instability. *Monthly Weather Review*, **127 (12)**, 2709–2732, doi:10.1175/1520-0493(1999)127⟨2709:TUAMOC⟩2.0.CO;2.

Schwingshackl, C., M. Hirschi, and S. I. Seneviratne, 2018: A theoretical approach to assess soil moisture-climate coupling across cmip5 and glace-cmip5 experiments. *Earth System Dynamics*, **9 (4)**, 1217–1234.

Seneviratne, S. I., T. Corti, E. L. Davin, M. Hirschi, E. B. Jaeger, I. Lehner, B. Orlowsky, and A. J. Teuling, 2010: Investigating soil moisture–climate interactions in a changing climate: A review. *Earth-Science Reviews*, **99 (3-4)**, 125–161.

Seth, A., A. Giannini, S. Rauscher, S. Bordoni, D. Singh, and S. Camargo, 2018: Monsoon responses to climate changes– similarities and differences between regions. *Current Climate Change Reports*.

Seth, A., S. A. Rauscher, M. Biasutti, A. Giannini, S. J. Camargo, and M. Rojas, 2013: Cmip5 projected changes in the annual cycle of precipitation in monsoon regions. *Journal of Climate*, **26 (19)**, 7328–7351.

Seth, A., S. A. Rauscher, M. Rojas, A. Giannini, and S. J. Camargo, 2011: Enhanced spring convective barrier for monsoons in a warmer world? *Climatic Change*, **104 (2)**, 403–414.

Seth, A., M. Rojas, and S. A. Rauscher, 2010: Cmip3 projected changes in the annual cycle of the south american monsoon. *Climatic Change*, **98 (3-4)**, 331–357.

Sharma, O., H. Le Treut, G. Seze, L. Fairhead, and R. Sadourny, 1998: Interannual variations of summer monsoons: Sensitivity to cloud radiative forcing. *Journal of climate*, **11 (8)**, 1883–1905.

Shekar, and Boos, 2016: Improving energy-based estimates of monsoon location in the presence of proximal deserts. *Journal of Climate*, **29 (13)**.

Sherwood, S., and Q. Fu, 2014: A Drier Future? *Science*, **343 (6172)**, 737–739, doi:10.1126/science.1247620.

Shukla, J., and Y. Mintz, 1982: Influence of land-surface evapotranspiration on the earth's climate. *Science*, **215 (4539)**, 1498–1501.

Silva, A. R., F. M. Pimenta, A. T. Assireu, and M. H. C. Spyrides, 2016: Complementarity of brazil s hydro and offshore wind power. *Renewable and Sustainable Energy Reviews*, **56**, 413–427.

Silva, V. B., and V. E. Kousky, 2012: The south american monsoon system: climatology and variability. *Modern climatology*, **398**.

Skinner, C. B., and N. S. Diffenbaugh, 2014: Projected changes in african easterly wave intensity and track in response to greenhouse forcing. *Proceedings of the National Academy of Sciences*, **111 (19)**, 6882–6887.

Smyth, J., S. Hill, and Y. Ming, 2018: Simulated responses of the west african monsoon and zonal-mean tropical precipitation to early holocene orbital forcing. *Geophysical Research Letters*, **45**, 12,049– 12,057, doi:10.1029/2018GL080494.

Smyth, J. E., and Y. Ming, 2020: Characterizing drying in the south american monsoon onset season with the moist static energy budget. *Journal of Climate*, **33 (22)**, 9735—-9748, doi:10.1175/JCLI-D-20-0217.1.

Smyth, J. E., and Y. Ming, 2021: Investigating the impact of land surface characteristics on monsoon dynamics with idealized model simulations and theories. *Journal of Climate*, 1–49, doi:10.1175/JCLI-D-20-0954.1.

Soares, W. R., and J. A. Marengo, 2009: Assessments of moisture fluxes east of the andes in south america in a global warming scenario. *International Journal of Climatology: A Journal of the Royal Meteorological Society*, **29 (10)**, 1395–1414.

Sørland, S. L., and A. Sorteberg, 2016: Low-pressure systems and extreme precipitation in central india: sensitivity to temperature changes. *Climate Dynamics*, **47 (1)**, 465–480.

Sørland, S. L., A. Sorteberg, C. Liu, and R. Rasmussen, 2016: Precipitation response of monsoon low-pressure systems to an idealized uniform temperature increase. *Journal of Geophysical Research: Atmospheres*, **121 (11)**, 6258–6272.

Suzuki, A. H., R. C. Zambon, and W. W. Yeh, 2015: Water supply planning and operation in the metropolitan region of são paulo: Worst drought in history, conflicts, response, and resilience. *World Environmental and Water Resources Congress 2015*, 2226–2235.

Taylor, K. E., D. Williamson, and F. Zwiers, 2000: *The sea surface temperature and sea-ice concentration boundary conditions for AMIP II simulations*. Program for Climate Model Diagnosis and Intercomparison, Lawrence Livermore ....

Thompson, C., D. Schultz, and G. Vaughan, 2017: A Global Climatology of Tropospheric Inertial Instability. *Journal of the Atmospheric Sciences*, **75**, doi: 10.1175/JAS-D-17-0062.1.

Tiezzi, R. O., P. S. Barbosa, J. E. Lopes, A. L. Francato, R. C. Zambon, A. Silveira, P. H. Menezes, and J. M. Isidoro, 2019: Trends of streamflow under climate change for 26 brazilian basins. *Water policy*, **21 (1)**, 206–220.

Tomas, R. A., and P. J. Webster, 1997: The role of inertial instability in determining the location and strength of near-equatorial convection. *Quarterly Journal of the Royal Meteorological Society*, **123 (542)**, 1445–1482.

Torres, R. R., and J. A. Marengo, 2013: Uncertainty assessments of climate change projections over south america. *Theoretical and applied climatology*, **112 (1-2)**, 253–272.

Turner, A. G., and H. Annamalai, 2012: Climate change and the south asian summer monsoon. *Nature Climate Change*, **2 (8)**, 587–595.

Ukkola, A. M., M. G. De Kauwe, M. L. Roderick, G. Abramowitz, and A. J. Pitman, 2020: Robust future changes in meteorological drought in CMIP6 projections despite uncertainty in precipitation. preprint, Climatology (Global Change). doi: 10.1002/essoar.10502465.1.

Vallis, G. K., and Coauthors, 2018: Isca, v1. 0: A framework for the global modelling of the atmospheres of earth and other planets at varying levels of complexity.

Van Der Wiel, K., A. J. Matthews, D. P. Stevens, and M. M. Joshi, 2015: A dynamical framework for the origin of the diagonal south pacific and south atlantic convergence zones. *Quarterly Journal of the Royal Meteorological Society*, **141 (691)**, 1997–2010.

Vera, C., and Coauthors, 2006: The south american low-level jet experiment. *Bulletin of the American Meteorological Society*, **87 (1)**, 63–78.

Voigt, A., S. Bony, J.-L. Dufresne, and B. Stevens, 2014: The radiative impact of clouds on the shift of the intertropical convergence zone. *Geophysical Research Letters*, **41 (12)**, 4308–4315.

Vuille, M., and Coauthors, 2012: A review of the south american monsoon history as recorded in stable isotopic proxies over the past two millennia. *Climate of the Past Discussions*, **8 (1)**.

Walker, C. C., and T. Schneider, 2005: Response of idealized hadley circulations to seasonally varying heating. *Geophysical research letters*, **32 (6)**.

Walker, C. C., and T. Schneider, 2006: Eddy influences on hadley circulations: Simulations with an idealized gcm. *Journal of the atmospheric sciences*, **63 (12)**, 3333–3350.

Walker, J. M., S. Bordoni, and T. Schneider, 2015: Interannual variability in the large-scale dynamics of the south asian summer monsoon. *Journal of Climate*, **28 (9)**, 3731–3750.

Wang, B., C. Jin, and J. Liu, 2020: Understanding future change of global monsoons projected by cmip6 models. *Journal of Climate*, **33 (15)**, 6471–6489, doi:10.1175/JCLI-D-19-0993.1.

Wang, H., and R. Fu, 2004: Influence of cross-andes flow on the south american low-level jet. *Journal of climate*, **17 (6)**, 1247–1262.

Webster, P. J., 1983: Mechanisms of monsoon low-frequency variability: Surface hydrological effects. *Journal of Atmospheric Sciences*, **40 (9)**, 2110–2124.

Webster, P. J., V. O. Magana, T. Palmer, J. Shukla, R. Tomas, M. Yanai, and T. Yasunari, 1998: Monsoons: Processes, predictability, and the prospects for prediction. *Journal of Geophysical Research: Oceans*, **103 (C7)**, 14 451–14 510.

Williams, E., and Coauthors, 2002: Contrasting convective regimes over the Amazon: Implications for cloud electrification. *Journal of Geophysical Research: Atmospheres*, **107 (D20)**, LBA 50–1–LBA 50–19, doi:https://doi.org/10.1029/2001JD000380.

Wolf, A., W. R. L. Anderegg, and S. W. Pacala, 2016: Optimal stomatal behavior with competition for water and risk of hydraulic impairment. *Proceedings of the National Academy of Sciences*, **113 (46)**, E7222–E7230, doi:10.1073/pnas.1615144113.

Wu, G., and B. Liu, 2014: Roles of forced and inertially unstable convection development in the onset process of indian summer monsoon. *Science China Earth Sciences*, **57 (7)**, 1438–1451.

Xie, S.-P., C. Deser, G. Vecchi, and Coauthors, 2015: Towards predictive understanding of regional climate change. *Nature Climate Change*, **5 (10)**, 921–930.

Xie, S.-P., and N. Saiki, 1999: Abrupt onset and slow seasonal evolution of summer monsoon in an idealized gcm simulation. *Journal of the Meteorological Society of Japan. Ser. II*, **77 (4)**, 949–968.

Xue, Y., F. De Sales, W. Li, C. Mechoso, C. Nobre, and H. Juang, 2006: Role of land surface processes in south american monsoon development. *Journal of climate*, **19 (5)**, 741–762.

Yin, L., R. Fu, E. Shevliakova, and R. E. Dickinson, 2013: How well can cmip5 simulate precipitation and its controlling processes over tropical south america? *Climate Dynamics*, **41 (11-12)**, 3127–3143.

Zambon, R. C., M. T. Barros, and W. W.-G. Yeh, 2016: Impacts of the 2012–2015 drought on the brazilian hydropower system. *World Environmental and Water Resources Congress 2016*, 82–91.

Zemp, D. C., C.-F. Schleussner, H. M. J. Barbosa, and A. Rammig, 2017: Deforestation effects on Amazon forest resilience. *Geophysical Research Letters*, **44 (12)**, 6182–6190, doi:https://doi.org/10.1002/2017GL072955.

Zhai, J., and W. Boos, 2015: Regime transitions of cross-equatorial hadley circulations with zonally asymmetric thermal forcings. *Journal of the Atmospheric Sciences*, **72 (10)**, 3800–3818.

Zhang, Y., and S. Fueglistaler, 2020: How tropical convection couples high moist static energy over land and ocean. *Geophysical Research Letters*, **47 (2)**, e2019GL086 387.

Zhang, Y., I. Held, and S. Fueglistaler, 2021: Projections of tropical heat stress constrained by atmospheric dynamics. *Nature Geoscience*, **14 (3)**, 133–137.

Zhao, M., and Coauthors, 2018a: The gfdl global atmosphere and land model am4. 0/lm4. 0: 1. simulation characteristics with prescribed ssts. *Journal of Advances in Modeling Earth Systems*, **10 (3)**, 691–734.

Zhao, M., and Coauthors, 2018b: The gfdl global atmosphere and land model am4. 0/lm4. 0: 2. model description, sensitivity studies, and tuning strategies. *Journal of Advances in Modeling Earth Systems*, **10 (3)**, 735–769.

Zhou, W., and S.-P. Xie, 2018: A hierarchy of idealized monsoons in an intermediate gcm. *Journal of Climate*, **31 (22)**, 9021–9036.